SOFT MOLECULAR MATERIALS FOR SENSING AND ACTUATION

A Thesis Submitted for the Degree
of Doctor of Philosophy in the Faculty of Science

Submitted By
PRASENJIT GIRI

DEPARTMENT OF CHEMISTRY
JADAVPUR UNIVERSITY
JADAVPUR, KOLKATA-700032
INDIA
2025

যাদবপুর বিশ্ববিদ্যালয়
কলকাতা-৭০০০৩২, ভারত

*JADAVPUR UNIVERSITY
KOLKATA-700 032, INDIA

Dr. Manas Kumar Panda
Assistant Professor
Department of Chemistry ,
Faculty of Science
Email: manaspanda.chemistry@jadavpuruniversity.in

This is to certify that the thesis entitled "…….**SOFT MOLECULAR MATERIALS FOR SENSING AND ACTUATION** ……." Submitted by Sri. …… **PRASENJIT GIRI** …… ……. who got his / her name registered on……**18/03/2021**…… for the award of Ph. D. (Science) Degree of Jadavpur University, is absolutely based upon his own work under the supervision of…… ……**DR. MANAS KUMAR PANDA** …… and that neither this thesis nor any part of it has been submitted for either any degree / diploma or any other academic award anywhere before.

08/7/2025

Dr. Manas Panda
Assistant Professor
Department of Chemistry
Jadavpur University
Kolkata-700 032

……
(Signature of the Supervisor(s) date with official seal)

Dedicated to

Baba, Maa and Dada

Acknowledgements

As I approach the end of my Ph.D. journey, I take a moment to reflect on the many individuals who have been crucial to this accomplishment. I am profoundly grateful to everyone who has supported, guided, and encouraged me throughout this process. While I will make every effort to acknowledge everyone who has contributed, I apologize in advance if I inadvertently leave anyone out.

The first person who comes to mind is my supervisor, Dr. Manas Kumar Panda, from the Department of Chemistry at Jadavpur University. His steadfast encouragement has been crucial to my research. Dr. Panda's skill in clarifying even the most complex concepts significantly enhanced my understanding, especially in areas such as single crystal formation techniques, Single Crystal X-Ray Diffraction, Powder X-Ray Diffraction, Fluorescence Spectroscopy, Solid State Chemistry, FTIR, and actuation. His approachable demeanor and the supportive environment he fostered in the lab were instrumental in overcoming the challenges of research. I am profoundly grateful for both his academic mentorship and personal support throughout this journey.

I would also like to express my heartfelt thanks to my lab-mates, Dibyendu Dey, Diotima Bhattacharjee, Souvik Garani, Mainak Ghosh and Ranajit Mandal. Their collaboration, shared insights, and emotional support were instrumental in sustaining my momentum, even during difficult times. I feel truly fortunate to have worked in such a warm and encouraging environment.

I extend my deepest gratitude to my collaborators— Dr. Ahmad Husain, Prof. Rajadurai Chandrasekar, Dr. Ganesh Chandra Nandi, Dr. Nayim Sepay, and Dr. Atanu Panda—for their significant contributions and partnership. I am especially thankful to Prof. Arup Gayen, Dr. Partha Mahata, Prof. Chittaranjan Sinha, Prof. Samaresh Bhattattacharya and Dr. Bibhuti Bhushan Shaw for their unwavering support and motivating encouragement throughout my research career.

I wish to convey my heartfelt appreciation to Prof. Debajyoti Ghoshal, Prof. Gourhari Maiti, Prof. Rina Ghosh, Prof. Umesh Chandra Halder, Prof. Sujoy Kumar Baitalik, Prof. Shouvik Chattapadhyay, Prof. Kajal Krishna Rajak, Prof. Amrita Saha, and Prof. Partha Roy for their consistent encouragement and invaluable guidance throughout my journey. Their thoughtful suggestions and support have been instrumental in shaping my work. Additionally, I extend my gratitude to the other esteemed faculty members of the Department of Chemistry, as well

as to the Office of the Head of the Department and the Dean, for their prompt and helpful assistance, which has greatly facilitated my research efforts.

I am deeply thankful to Gopal da, Sourav da, Aruntima di, Anupam, Arijit, Osman, Ayan da, Adwitiya di, Rabi da, and Paramita di, whose support has been invaluable. I also extend my heartfelt gratitude to Krishna, Shippy, Paramita, Pravat da, Prasita, Uday, Soumitra , Rajdeep, Subhajit, Abhishek, Santu da, Suman, and Srimanta da. Whether through direct involvement or indirect encouragement, their contributions have played a crucial role in my achievements. The impact of their support, in all its forms, has been profound and deeply appreciated, and I am sincerely grateful for their presence and assistance throughout this journey.

I would also like to express my sincere gratitude for the financial support generously provided by the Council of Scientific and Industrial Research (CSIR), India. Additionally, I am deeply appreciative of the essential infrastructure and laboratory facilities offered by Jadavpur University. These resources were instrumental in enabling me to complete my thesis, and their contribution to my research cannot be overstated.

I extend my deepest gratitude to my beloved parents, whose constant love, support, and encouragement have been my guiding light throughout this journey. The moral values they imparted to me from a young age have formed the bedrock of my life, and their unwavering emotional and inspirational support has carried me through every challenge. I am also profoundly thankful to my sister-in-law, Moumita Khanra Giri, my elder sister, Krishna Kanta Giri, and my nephew, Arghyadeep Giri, for their enduring love and support throughout my academic career. Their presence and encouragement have been immensely valuable, and I am deeply appreciative of their steadfast support.

I am also deeply grateful to my parents for respectingmy decision to pursue a Ph.D. and for standing by me every step of the way.

Department of Chemistry

Jadavpur University

Kolkata 700032

Prasenjit Giri

Contents

Abstract

SOFT MOLECULAR MATERIALS FOR SENSING AND ACTUATION

Index number: 14/21/Chem./27 dated. 16/03/2021

The thesis work titled "SOFT MOLECULAR MATERIALS FOR SENSING AND ACTUATION" focusses on developing soft molecular crystalline material that are mechanically responsive to light illumination. These materials are a class of smart materials that have exceptional ability to directly convert light energy into various types of mechanical response such as bending, shape change, jumping, cracking, volume expansion etc due to the photoinduced chemical transformation of the molecules in solid state. The molecular motion generated due to photoinduced reaction is amplified to macroscopic motion by cooperative mechanism which is manifested as actuation. The research work is divided in four chapters. First chapter includes literature survey on soft actuating materials.

In the second chapter, I have carried out the synthesis of a new green fluorescent organic compound (***E*-ArF$_2$**) which display light controlled actuation and shape change in presence of 390 nm light. We have demonstrated that the direction of the motion of the solid crystals can be manipulated and steered by controlling the illumination direction.

In the third chapter, we reported the first example of two crystal solvatomorphs (solvates) of an anthracene-hydrazide based molecule (Ant) that display very distinct photo-responsive behaviour when 365 or 405 nm or visible light is illuminated. While one solvatomorph (**Ant-H$_2$O**) display an unique photo-puffing behaviour with large volume expansion that mimic the phenomenon of rice puffing (by heat treatment), the other solvatomorph (**Ant-DMF**) display photoinduced cracking, bending and jumping behaviour in presence of 405 nm light.

The last chapter discusses about the synthesis and distinct photo-responsive behaviour of two geometric isomers of a single molecule (**NMe$_2$CNF$_2$**) synthesis of a new green fluorescent organic compound (**NMe$_2$CNF$_2$**) by Knoevenagel condensation reaction. The single crystals of the *trans*- (*-E*- **NMe$_2$CNF$_2$**) isomer display photo-actuation, and salient property in presence of 405 nm light, while the corresponding *cis*-isomer. *Z*-**NMe$_2$CNF$_2$** is silent to light illumination. Our mechanistic investigation reveals that the distinct photo-response in solid state is rooted to their molecular configuration, packing and intermolecular interactions in solid state.

In summary, the work presented in my thesis demonstrate some novel photo-responsive systems that can perform direct energy transduction from light. These results have been published in various mainstream journals such as *Chemistry-A European Journal*, *Angew Chem, Int. Ed*, *CrystEngComm*, *Cryst Growth & Design* etc

SIGNATURE OF SUPERVISOR
(with seal)

Dr. Manas Banda
Assistant Professor
Department of Chemistry
Jadavpur University
Kolkata-700 032

Prasenjit Giri

(FULL SIGNATURE OF THE CANDIDATE)

Date 08/07/2025

I have obtained significant number of interesting results on light-responsive materials and their possible applications. I have published several papers in the mainstream journals such as Chemistry-A European Journal, Angewandte Chem, Int. Ed, CrystEngComm etc. The references of these papers are given below---

[1].Light-fueled rapid macroscopic motion of a green fluorescent organic crystal. **Giri, P.**, Mazumder, A., Dey, D., Garani, S., Raveendran, A., & Panda, M. K. (2021). *CrystEngComm*, *23*(34), 5876–5881.https://doi.org/10.1039/d1ce00460c

[2].Photoinduced Puffing with Large Volume Expansion and Photomechanical Motions induced by Topochemical [4+4] Reactions in Molecular Crystal Solvates. **Giri, P.**, Panda, A., & Panda, M.K.(2024).*Chemistry-A European Journal*. https://doi.org/10.1002/chem.202303836

[3].Aggregation induced emission and mechanochromic luminescence by cyanostilbene-based organic luminophores. Dey, D., **Giri, P.**, Sepay, N., Husain, A., & Panda, M. K. (2023). *Journal of Photochemistry and Photobiology. A: Chemistry*, *437*, 114480. https://doi.org/10.1016/j.jphotochem.2022.114480

[4].Dimension Engineering of Stimuli-Responsive 1D Molecular Crystals into Unusual 2D and 3D Zigzag Waveguides. Annadhasan, M., Kumar, A. V., **Giri, P.**, Nandy, S., Panda, M. K., Jose, K. V. J., & Chandrasekar, R. (2023). *Angewandte Chemie* Int. Ed. *135*(25). https://doi.org/10.1002/anie.202302929

[5].Tunable Photoresponsive Behavior of Organic Materials by Polymorphic Variation: Topochemical [2 + 2] Cycloaddition vs E–Z Isomerization. Shabashini, A., **Giri, P.**, Richard, S., Husain, A., Panda, M. K. & Nandi, G.C.(2024). *Cryst. Growth Des.* 24(19), 7897–7903. https://doi.org/10.1021/acs.cgd.4c00759

[6].Polymorphism and Substitutional Effect on the Thermoresponsive and Luminescence Properties of Organic Molecular Crystals. Mazumder, P., Dey, D., **Giri, P**., Garani, S., Mandal, R., Husain, A. & Panda, M.K. (2024). *Cryst. Growth Des.* 2024, 24(19), 7925–7935. https://doi.org/10.1021/acs.cgd.4c00827

1.1 Introduction

Actuation is a critical concept in various fields like engineering, robotics, control systems, biology, and more. At its core, **actuation** refers to the process of initiating or triggering a mechanical action or movement within a system or mechanism. It is the means by which a system responds to input signals or stimuli, transforming energy into a physical action or output. In simple terms, it's what makes a system "do something."

The term "actuator" is used to describe the device that carries out the actuation process. An actuator takes energy (usually electrical, hydraulic, or pneumatic) and converts it into motion or force that achieves a desired outcome, such as moving an object, adjusting a valve, or positioning a robotic limb. Photomechanical actuation is the phenomenon in which materials undergo mechanical motion or deformation in response to light. This light-induced motion can manifest as bending, twisting, jumping, rotation, cracking, expansion, or other physical displacements. Among various photo mechanically active systems, **organic molecular crystals** have emerged as an exciting class of materials that exhibit diverse and tunable actuation behaviours under optical stimuli.

Organic crystals, owing to their highly ordered molecular arrangement and the presence of photoresponsive functional groups, provide an ideal platform for understanding and engineering light-induced mechanical responses. These crystals offer not only aesthetic optical properties but also functional mechanical transformations, making them highly relevant in the design of next-generation light-powered actuators, sensors, and smart materials.

Mechanism of Photomechanical Actuation

The mechanical response of organic crystals to light originates from photochemical or photophysical changes that occur at the molecular level and propagate to the macroscopic scale. The key mechanisms include:

1. **Photoisomerization**: Molecules such as azobenzene undergo cis-trans isomerization when exposed to UV or visible light. This geometric change introduces mechanical strain in the crystal lattice, leading to deformation or bending.
2. **Photodimerization or Photocleavage**: Certain organic molecules undergo bond formation (e.g., [2+2] cycloaddition of anthracenes or cinnamic acid derivatives) or

bond cleavage upon irradiation. These reactions cause local changes in molecular volume or packing, generating mechanical stress that results in visible actuation.

3. **Photothermal Expansion**: Light absorption by the crystal may lead to localized heating, causing anisotropic thermal expansion. In crystals with directionally dependent expansion coefficients, this results in bending, curling, or rotation.
4. **Charge Transfer and Dipole Change**: In some crystals, light induces intramolecular or intermolecular charge transfer, leading to changes in dipole interactions and packing forces. This electronic rearrangement can also cause crystal deformation.

The **direction, magnitude, and type of actuation** depend strongly on the crystal morphology, growth facets, molecular orientation, and nature of non-covalent interactions such as hydrogen bonding and π–π stacking.

Representative Examples and Observations

Numerous organic crystals have been reported to exhibit photomechanical behaviour. One prominent class involves anthracene derivatives, which undergo photodimerization reactions upon UV exposure. For example, anthracene-based solvatomorphs can demonstrate dramatic mechanical responses such as chopping, cracking, or puffing when irradiated with a 395–405 nm laser.

A particularly novel example is the Ant-H_2O solvatomorph, which exhibits a rare puffing phenomenon—a sudden and substantial volumetric expansion (up to 50% within 104 seconds) under continuous laser irradiation. This puffing is reminiscent of the puffing of rice under heat and results from structural transformation and hydrogen bond weakening due to light-induced molecular reorientation. SEM images show that, as irradiation time increases, multiple surface layers are formed and the interlayer distance decreases due to repeated delamination, a behavior not reported in conventional photomechanical systems.

Another example is salicylideneaniline and azobenzene crystals, which bend and curl reversibly upon exposure to alternating UV and visible light, driven by the reversible cis-trans photoisomerization process. Similarly, crystals of diarylethenes undergo irreversible bending or expansion due to photocyclization reactions, which significantly alter molecular geometry.

Applications of Photomechanical Organic Crystals

The ability of organic crystals to convert light directly into mechanical motion makes them highly attractive for a range of emerging technologies:

- **Soft Robotics**: Organic crystals can act as miniature actuators that bend, twist, or propel microstructures upon light exposure, enabling motion without motors or wiring.
- **Optical Switches and Sensors**: The light-induced shape change can be used to design mechanical switches or sensors that respond to specific light wavelengths.
- **Drug Delivery Systems**: Photomechanical behavior can be exploited to create light-triggered capsules that open or expand to release their contents on demand.
- **Artificial Muscles**: Some crystals demonstrate reversible expansion-contraction cycles that can mimic the action of biological muscles when exposed to pulsed light.
- **Microfluidics and Lab-on-a-Chip Devices**: Controlled deformation can serve as light-driven valves or pumps for directing fluid flow in small-scale systems.

Challenges and Future Outlook

Despite their potential, photomechanical organic crystals face several challenges that must be addressed for practical applications:

- **Mechanical Fatigue**: Repeated actuation may degrade crystal integrity over time due to fracture or defect accumulation.
- **Limited Scalability**: Crystals are often small and delicate, making it difficult to use them in large-scale devices.
- **Environmental Sensitivity**: Many organic crystals are sensitive to moisture, oxygen, and thermal conditions, requiring controlled environments for stability.
- **Low Conversion Efficiency**: The conversion of light energy to mechanical motion is still relatively low compared to conventional actuators.

However, with ongoing advances in **crystal engineering, computational modeling, and hybrid composite systems**, these challenges are being progressively overcome. Future research may focus on **stimuli-responsive co-crystals**, **multi-functional hybrid materials**, and **3D-printed photomechanical structures** that combine the precision of organic crystal actuation with robustness and tenability.

1.2 Background of this study: Literature Survey

With the rapid progression of technology, intelligent responsive actuators- materials capable of converting chemical or physical stimuli into large-scale deformation- have found growing application in both engineering and daily life[1]. These actuators can be activated by a variety of external triggers, including pH,[2-7] gases,[8-10] temperature,[11-14] as well as stimuli like light,[15-16] electric fields, and magnetic fields[17-20]. Their exceptional softness, multifunctionality, and unique mechanical traits—such as easy modification, simple processing, and straightforward assembly—have made them a focal point of research in advanced materials science[21-22]. As a result, the development of multi-responsive, highly selective, and ultra-sensitive smart films has emerged as an urgent research direction.

Traditional rigid robots, while effective in controlled environments, suffer from limited flexibility, being restricted mainly to linear motion and rotation[23-24]. In contrast, soft actuators, essential components of soft robots, can undergo significant deformation, absorbing energy from contacts and collisions while adapting to their surroundings. These flexible actuators primarily transform light, heat, or electrical energy into mechanical motion, mimicking the function of human body effectors[25-26]. For optimal performance, soft actuating materials must possess high flexibility, enabling large-scale bending and stretching similar to muscles and skin, along with intelligent responsiveness that manifests through deformation, stress generation, electrical signal production, or variations in the electric field.

Among the various external stimuli, light stands out due to its cleanliness, the flexibility to adjust the stimulation area, remote controllability, and the abundance of light sources. Consequently, significant research efforts have focused on developing light-responsive actuators[27-30]. Intensive work has gone into creating diverse light-responsive materials and structures capable of rapid, sensitive, and large-scale deformation responses[31-33].

To fully realize the potential of light-responsive actuation systems and expand their applicability across various fields, further in-depth research into their working mechanisms, structural innovations, and application strategies is critically needed. Among these stimuli, light is especially attractive due to its ability to remotely and precisely control material behaviour.

A unique class of such responsive systems is molecular crystals, which possess the remarkable ability to translate light-induced molecular motion into observable mechanical actuation. This property has promising implications for fields such as soft robotics, medical devices, artificial muscles, and adaptive machinery. Crucially, molecular cooperativity within the crystal lattice plays a key role in amplifying nanoscale molecular transformations into large-scale movement. Most reported photomechanical molecular crystals—whether organic or metal–organic—feature photoresponsive units like azobenzene, anthracene, salicylidenephenylethylamines, styryl benzene, or diarylethene. These systems typically respond to UV light, undergoing reactions such as geometric isomerization, photocycloaddition, ring-opening/closing, or phase transitions. These localized photo-induced transformations generate surface strain differences, resulting in bimorphic deformation and subsequent macroscopic actuation.

Recently in 2018, Danial & co-workers have developed a light-responsive bilayer actuator using 3D printing and smart materials, enabling 4D-printed structures to change shape upon exposure to light. These actuators are made from poly(siloxane) polymers functionalized with azobenzene side groups, which respond rapidly to light through trans–cis isomerization. Two photoactive polymers were synthesized, including one reported for the first time, and tested in bilayer systems. The bilayers exhibited fast, reversible actuation with stresses ranging from 1.03 to 1.70 MPa. While the P2/Kapton configuration produced higher stress levels, the P1/Kapton bilayers showed greater bending angles. Future improvements, such as shortening alkyl linkers or increasing azobenzene content, could enhance the efficiency of light-to-motion conversion in these smart materials.

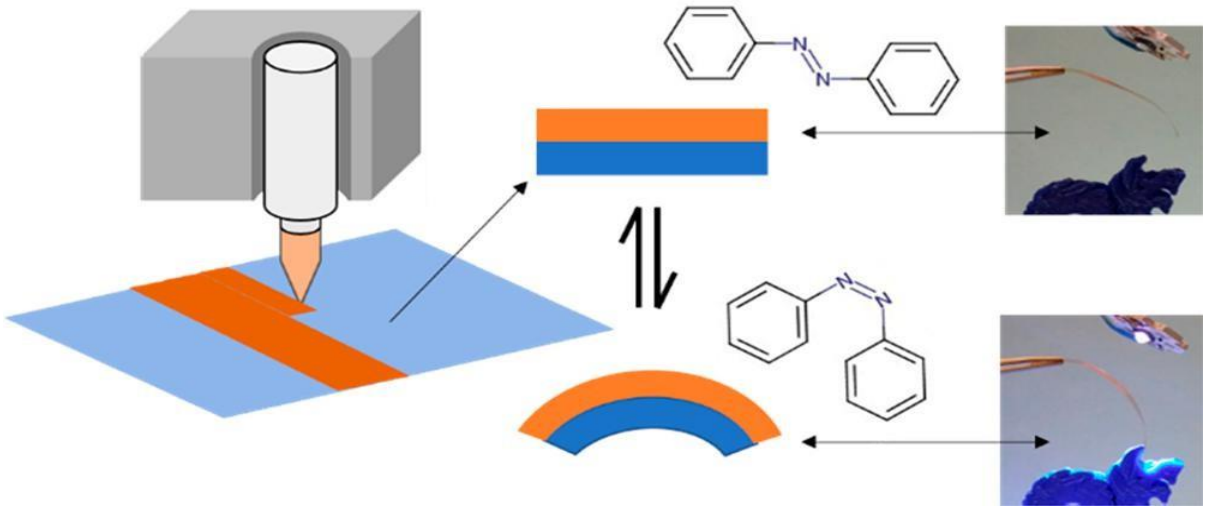

Figure 1. Danial & co-workers have developed photo activated polymeric bilayer actuators fabricated via 3D printing. Figures were taken from reference 34 and reprinted with copyright permission from ACS/RSC.

Recently in 2024, Jiawei & co-workers have shown a small chemical change (methyl to ethyl group) in similar molecular crystals drastically alters their mechanical and photomechanical behaviour. Crystal 1 (methyl) bends plastically and displays strong, reversible photomechanical motion under UV light, while crystal 2 (ethyl) exhibits elastic/plastic bending but no visible photomechanical response. Crystal 2 has stronger intermolecular interactions, higher elastic strain, and double the surface hardness compared to crystal 1. The rate of [2 + 2] photocycloaddition is faster in crystal 1 due to closer double bonds and weaker interlayer forces. Crystal 1's light-induced deformation enables it to move objects thousands of times its mass, achieving superior output force and work densities compared to traditional actuators. Overall, this work highlights how subtle changes in crystal packing control dynamic behaviour & material performance.

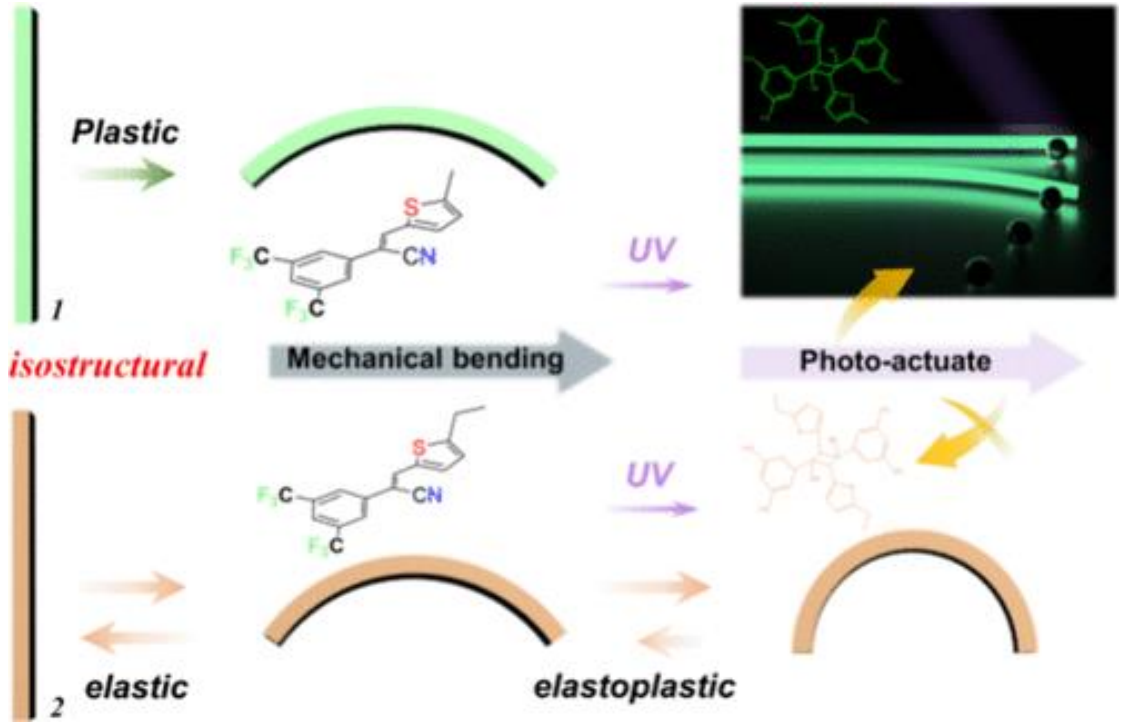

Figure 2. Jiawei & co-workers have shown a small chemical change (methyl to ethyl group) in similar molecular crystals drastically alters their mechanical and photomechanical behaviour.. Figures were taken from reference 35 and reprinted with copyright permission from ACS/RSC/ELSEVIER.

Recently in 2023, Min & co-workers have developed a method for developing photo-responsive liquid crystal elastomers (LCEs) that exhibit unique, light-induced periodic swing deformation. Two types of azobenzene-based LCEs, P(AZ-UPy) with high glass transition temperature (Tg) and P(AZ-BMA-UPy) with low Tg, were synthesized and analyzed. The low-Tg LCE showed typical reversible deformation under light, while the high-Tg P(AZ-UPy) displayed a distinct periodic swing motion when exposed to alternating 365 nm and 470 nm light. This motion was achieved by switching the light source on and off, inducing bending toward or away from the light. The unique swing deformation is attributed to the combination of high Tg and the photo-thermal effect of azobenzene groups. These findings offer a new strategy for designing LCEs with controllable deformation, useful for applications in soft robotics and smart devices.

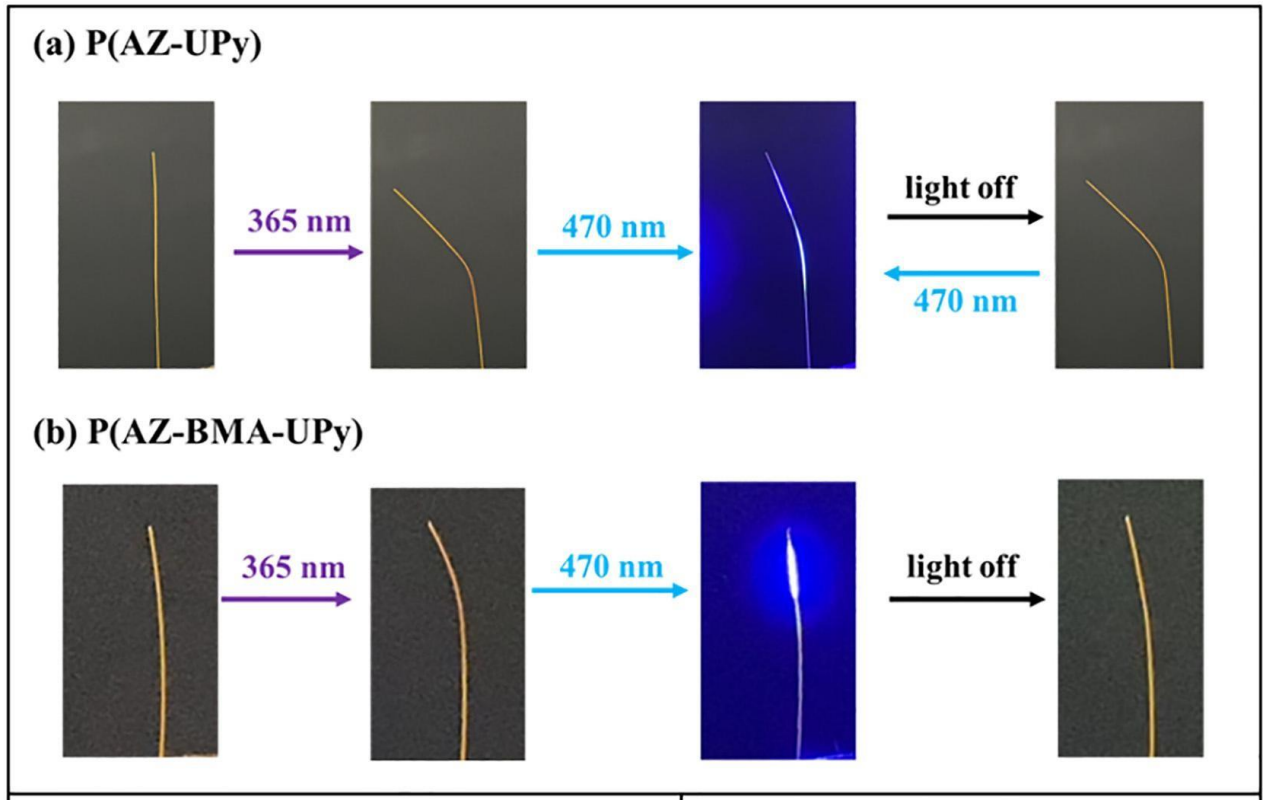

Figure 3. Xiaohu & co-workers have developed a shape memory polyurethane composite with self-healing and recyclable properties, activated by near-infrared (NIR) light. The photo-responsive deformation of LCEs fibers: (a) The photo-induced swing deformation of P(AZ-UPy) fibers. (b) The photo-induced reversible deformation of P(AZ-BMA-UPy) fibers. Figures were taken from reference 36 and reprinted with copyright permission from ACS/RSC/ELSEVIER.

Recently in 2022, Yuanxin & co-workers study introduces a supramolecular strategy for creating light-responsive helical microfibers that mimic biological shape-changing systems. The fibers are built using azobenzene units and multiple hydrogen bonds, which allow reversible spiral deformation without disassembling the structure upon light exposure. The localized isomerization of azobenzene triggers deformation at the molecular level, which is then amplified to micrometer-scale motion. The key innovation lies in the hydrogen-bond network, which restricts dissociation and enables coordinated movement. This approach offers a noncovalent pathway for designing robust, biomimetic materials capable of mechanical actuation. It opens new possibilities for soft actuators and stimuli-responsive materials inspired by nature.

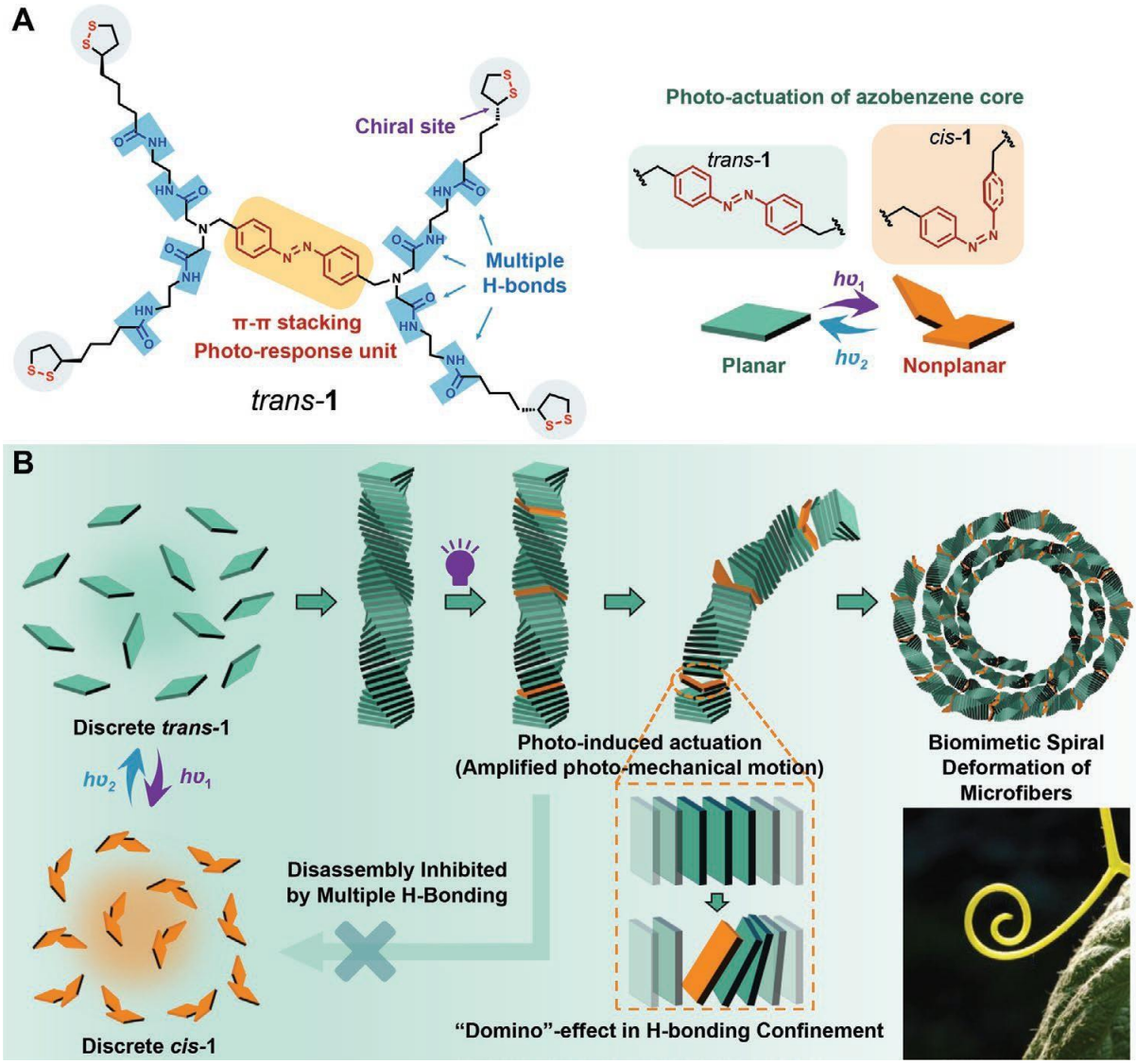

Figure 4.Yuanxin & co-workers study introduces a supramolecular strategy for creating light-responsive helical microfibers that mimic biological shape-changing systems. Structural design and schematic representation of the assembly of the photoresponsive building block. A) Molecular structure and photoisomerization of the trans-1 and geometrical change leading to possible photomechanical actuation (hν1 = 365 nm, hν2 = 420 nm). B) Schematic representation of the light-induced deformation of the assemblies of trans-1. The supramolecular assembly of trans-1 is initiated by lowering solvent polarity, leading to the formation of helical fibers, which can bend and spiral into coils upon irradiation of UV light ((hν1 = 365 nm, hν2 = 420 nm). The inset image shows a typical spiral plant stem in Nature. Figures were taken from reference 37 and reprinted with copyright permission from ACS/RSC/ELSEVIER.

Recently in 2019, Hao Li & co-workers report the development of ultrafast, dual-driven all-carbon actuators made from graphene oxide (GO) and oriented carbon nanotubes (CNTs). These actuators respond to both humidity and near-infrared (NIR) light, exhibiting rapid deformation (as fast as 0.08 seconds) and large-scale movements like bending, twisting, jumping, and lifting. Their performance includes precise directional control, high deformation amplitude (up to 70°/mm), and excellent durability with no fatigue after 10,000 cycles. The CNT orientation allows for programmable and complex motion styles, including chiral twisting and vertical jumping. These actuators demonstrate practical capabilities such as throwing or catching fast-moving objects and lifting loads over 20 times their weight. Their unique combination of speed, strength, and responsiveness makes them highly suitable for artificial muscles, soft robotics, and smart devices**.**

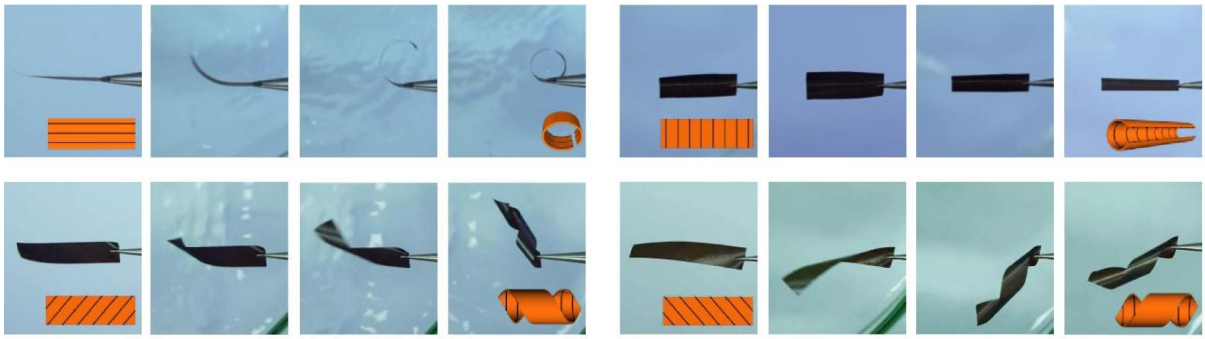

Figure 5. Hao Li & co-workers report the development of ultrafast, dual-driven all-carbon actuators made from graphene oxide (GO) and oriented carbon nanotubes (CNTs). Humidity-

driven deformation of GO−CNT actuators. (A−D) Real-time actuation images of the actuators with different α values (A: strip-0°, B: strip-90°, C: strip-45°, D: strip-135°) in response to humidity change from 56 to 80%. Figures were taken from reference 38 and reprinted with copyright permission from ACS/RSC/ELSEVIER.

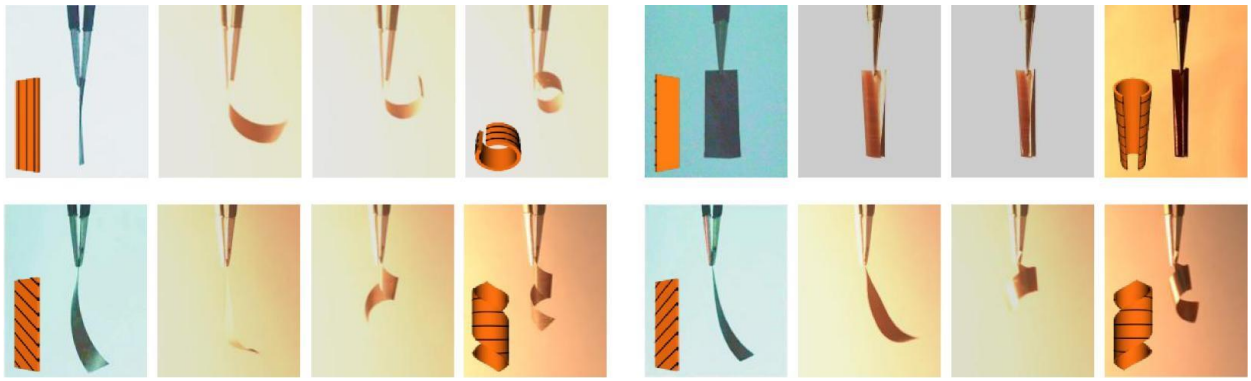

Figure 6. Hao Li & co-workers report the development of ultrafast, dual-driven all-carbon actuators made from graphene oxide (GO) and oriented carbon nanotubes (CNTs). NIR light-driven deformation of GO−CNT actuators. (A−D) Real-time actuation images of the actuators with different α values (A: strip-0°, B: strip-90°, C: strip-45°, D: strip-135°) in response to NIR light irradiation with an intensity of 300 mW/cm^2. Figures were taken from reference 38 and reprinted with copyright permission from ACS/RSC/ELSEVIER.

Recently in 2017, Inspired by the intelligence and responsiveness of biological systems, Owies & co-workers have developed a soft, light-powered artificial flytrap capable of autonomous action. This device, created using a light-responsive liquid-crystal elastomer mounted on the tip of an optical fiber, mimics the behaviour of natural flytraps by using optical feedback to trigger motion. The fiber delivers light to power the system and also acts as a sensor, detecting reflected or scattered light from nearby objects. This feedback mechanism enables the device to autonomously close and even distinguish between different objects, functioning as a miniature, self-regulating robotic gripper. The innovation opens new possibilities for intelligent, soft micro-robotics with applications in delicate manipulation and environmental sensing.

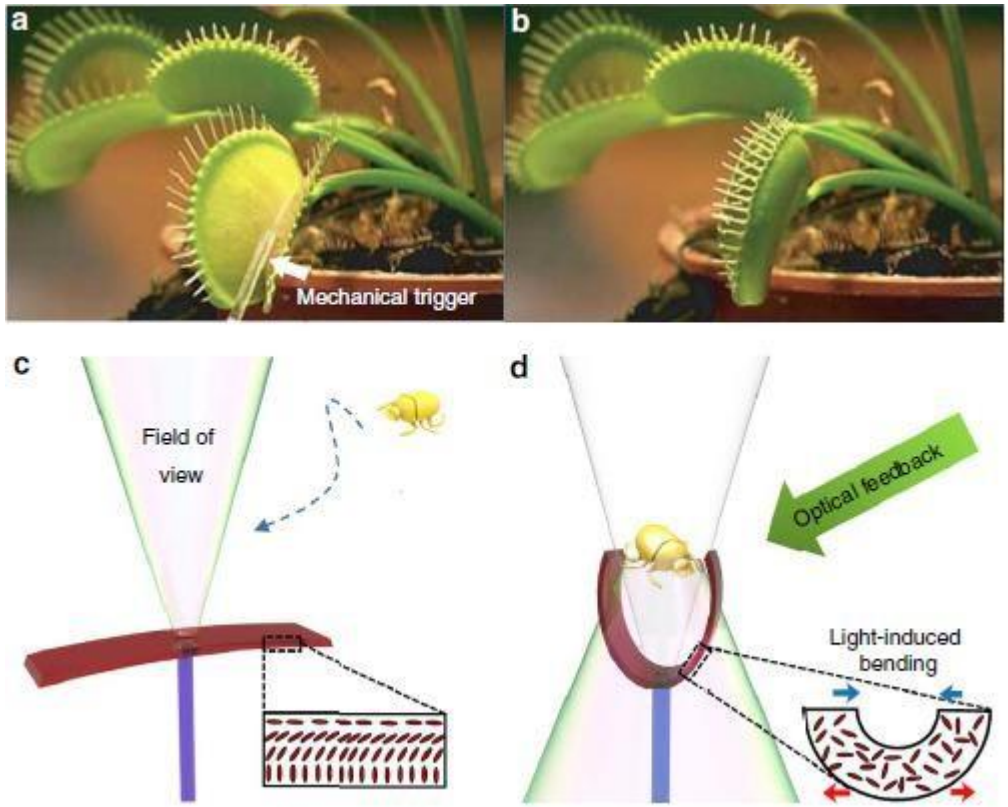

Figure 7. Owies & co-workers have developed a soft, light-powered artificial flytrap capable of autonomous action. (a) A Venus flytrap at its open stage, (b) closes upon mechanical stimulation. (c) Schematic drawing of the light-triggered artificial flytrap at its open stage, when no object has entered its field of view. No light is back-reflected to the LCE actuator, which remains in the open stage. (d) The flytrap closes when an object enters its field of view and causes optical feedback to the LCE actuator. Light-induced bending of the LCE leads to closure action, thus capturing the object. The insets of c and d show the schematic molecular orientation in LCE actuator at the open and closed stages.. Figures were taken from reference 39 and reprinted with copyright permission from ACS/RSC/ELSEVIER.

Recently in 2024, Wangxiang Li & co-workers have reported that the crystals of 4-Fluoro-9-anthracenecarboxylic acid (4F-9AC) undergo a reversible [4 + 4] photodimerization reaction that can induce bending and twisting in microcrystals. In larger crystals, which resist deformation, the reaction can be directly visualized and is seen to begin at the crystal edges, propagating inward as a reaction front. A new kinetic model explains this behavior by proposing a mechanically induced, exponentially decaying reaction field that catalyzes the photochemical process. This field extends about 20 nm from the reacted to unreacted regions, enabling the reaction to spread across the crystal. The speed and direction of this propagation

can be controlled by adjusting light intensity or embedding amorphous barriers using electron beam lithography. These findings demonstrate that spatially complex reaction dynamics can be achieved in solid crystals under uniform illumination, opening possibilities for precise control in photomechanical materials.

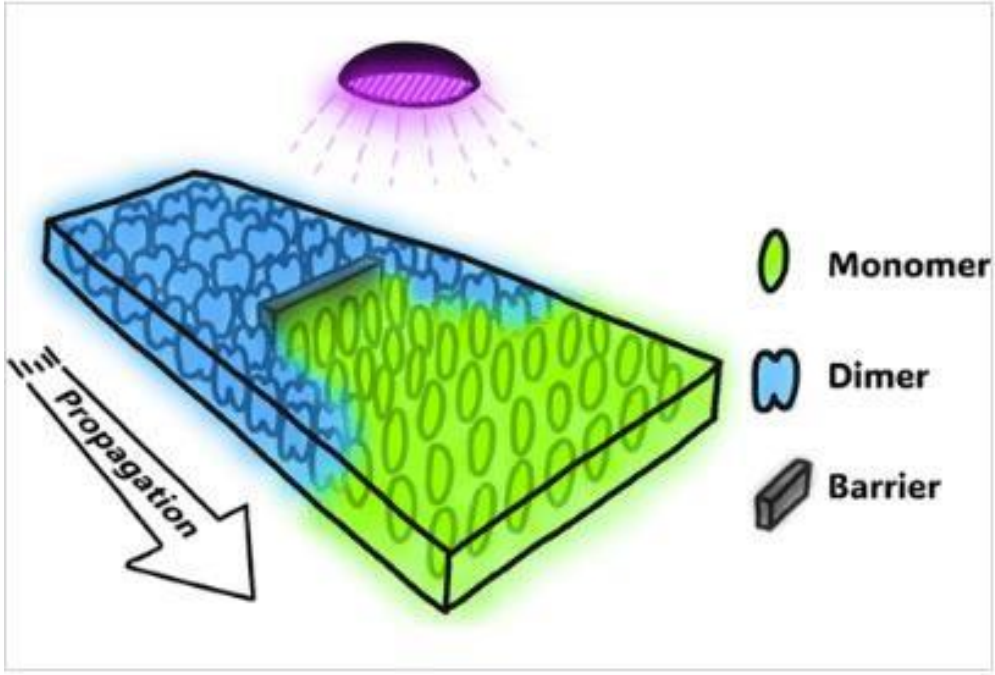

Figure 8. Wangxiang Li & co-workers have reported that the crystals of 4-Fluoro-9-anthracenecarboxylic acid (4F-9AC) undergo a reversible [4 + 4] photodimerization reaction that can induce bending and twisting in microcrystals. Figures were taken from reference 40 and reprinted with copyright permission from ACS/RSC/ELSEVIER.

Recently in 2024, Uma & co-workers have introduced six novel photoreactive Zn(II)-based coordination compounds that mimic natural mechanisms like seedpod explosion and bark peeling. These compounds, synthesized from 4-vinylpyridine derivatives and halide colinkers, exhibit dynamic mechanical responses such as rolling, cracking, jumping, and peeling under UV light. Structural analysis confirmed that compounds 1–5 are isostructural with partial photoreaction, while compound 6 showed complete photoreaction due to both linkers being planar. Interestingly, even nonplanar linkers that don't meet Schmidt’s criteria reacted, albeit at slower rates. Compound 6 uniquely exhibited a bark-like peeling effect, attributed to its distinct crystal packing and noncovalent interactions. These findings highlight the potential of Zn(II) coordination compounds for biomimetic photoactuation and optical switching applications.

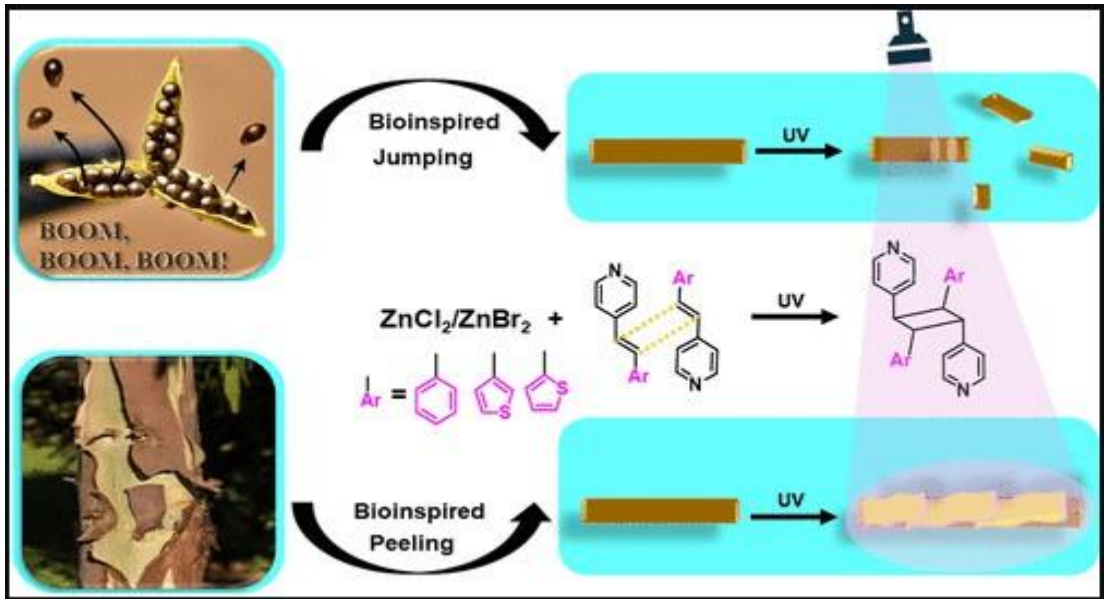

Figure 9. Uma & co-workers have introduced six novel photoreactive Zn(II)-based coordination compounds that mimic natural mechanisms like seedpod explosion and bark peeling. Figures were taken from reference 41 and reprinted with copyright permission from ACS/RSC/ELSEVIER.

Recently in 2024, Marieh & co-workers have introduced a significant breakthrough in self-healing for atomistically ordered materials using anilinium bromide crystals. Traditionally limited by slow mass transport and alignment requirements, such materials now show rapid and efficient healing—up to 49% within seconds and 95% after 100 minutes—through ferroelastic detwinning. Favorable surface alignment and strong ionic bonding enable this rapid self-repair. Real-time strain analysis revealed that pristine areas also undergo deformation, and the healed region does not necessarily become the weakest point. The study emphasizes that visual crack disappearance can be misleading, and mechanical testing is essential to confirm healing. These findings position organic crystals as competitive with polymers in self-healing performance, challenging conventional assumptions about their mechanical limitations.

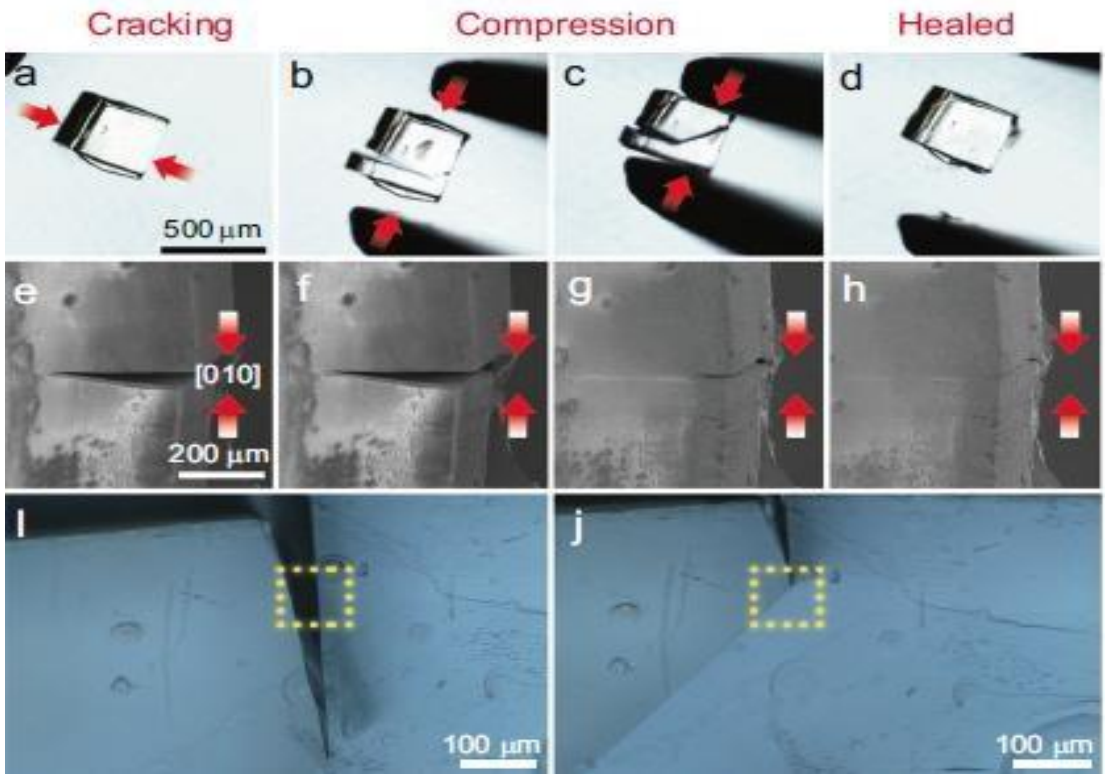

Figure 10. Marieh & co-workers have introduced a significant breakthrough in self-healing for atomistically ordered materials using anilinium bromide crystals. a–d Optical images of a crystal of P@AniHBr that has been partially separated and then healed by light compression taken at time points 0, 17, 28, and 49 s. e–h A series of electron micrographs of a crystal being compressed and healed in situ by using a tensile tester. i, j Optical images of a crystal that has been partially separated (i) and subsequently partially healed (j). Figures were taken from reference 42 and reprinted with copyright permission from ACS/RSC/ELSEVIER.

Recently in 2021, Jingjing & co-workers have introduced Phototropism which allows organisms to optimize light harvesting, inspiring artificial systems to do the same. Traditional photocatalytic technologies are limited by their reliance on fixed light sources and inability to autonomously track light. To overcome this, a bionic sunflower based on phototropic smart hydrogels was developed. This system can track light from 0° to 90° and recover energy losses caused by oblique light incidence. It maintains high and stable photocatalytic efficiency compared to static control samples. This innovation presents a promising strategy for enhancing solar energy utilization in photocatalytic applications.

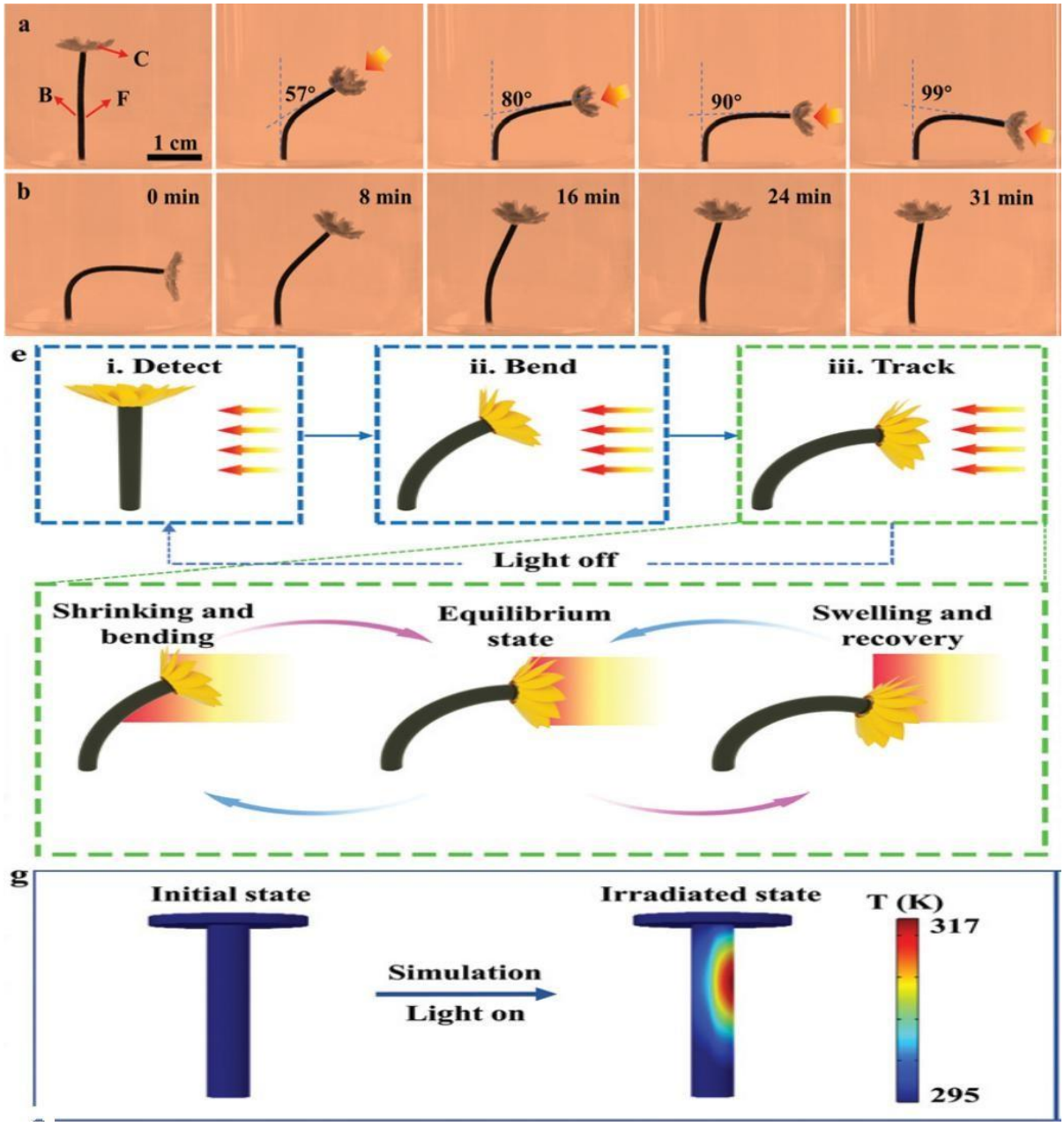

Figure 11. Jingjing & co-workers have introduced phototropism which allows organisms to optimize light harvesting, inspiring artificial systems to do the same. (a) Photographs of a bionic sunflower at different angles of incident light. (b) Photographs for the shape recovery process of a bended bionic sunflower. (c) The shape stability for the light-responsive behaviour of the bionic sunflower. (d) Normalized volume curve of the RPH with increasing temperature. (e) The as-proposed phototropic principle and process of the bionic sunflower. (g) The simulated thermal distribution in the RPH model. the bionic sunflower. (g) The simulated thermal distribution in the RPH model. Figures were taken from reference 43 and reprinted with copyright permission from ACS/RSC/ELSEVIER.

Recently in 2018, Hongmiao & co-workers have introduced optically driven active materials enable remote, precise, and contactless control of motion and deformation. In this study, a polydopamine (PDA)-coated liquid crystal elastomer (LCE) was developed, which responds rapidly to near-infrared (NIR) light due to the photo thermal effect of PDA and thermal responsiveness of LCE. The film can generate actuating stress up to 1.5 MPa—much higher than that of mammalian skeletal muscle—and responds in as little as one-tenth of a second. By adjusting the light exposure, the film can bend, contract, or roll, allowing for diverse motion patterns. A robotic swimmer prototype powered by these films demonstrated controlled swimming at the water–air interface using light-induced bending motions. These findings highlight PDA-coated LCE as a promising material for artificial muscles in soft robotics and opto-mechanical devices.

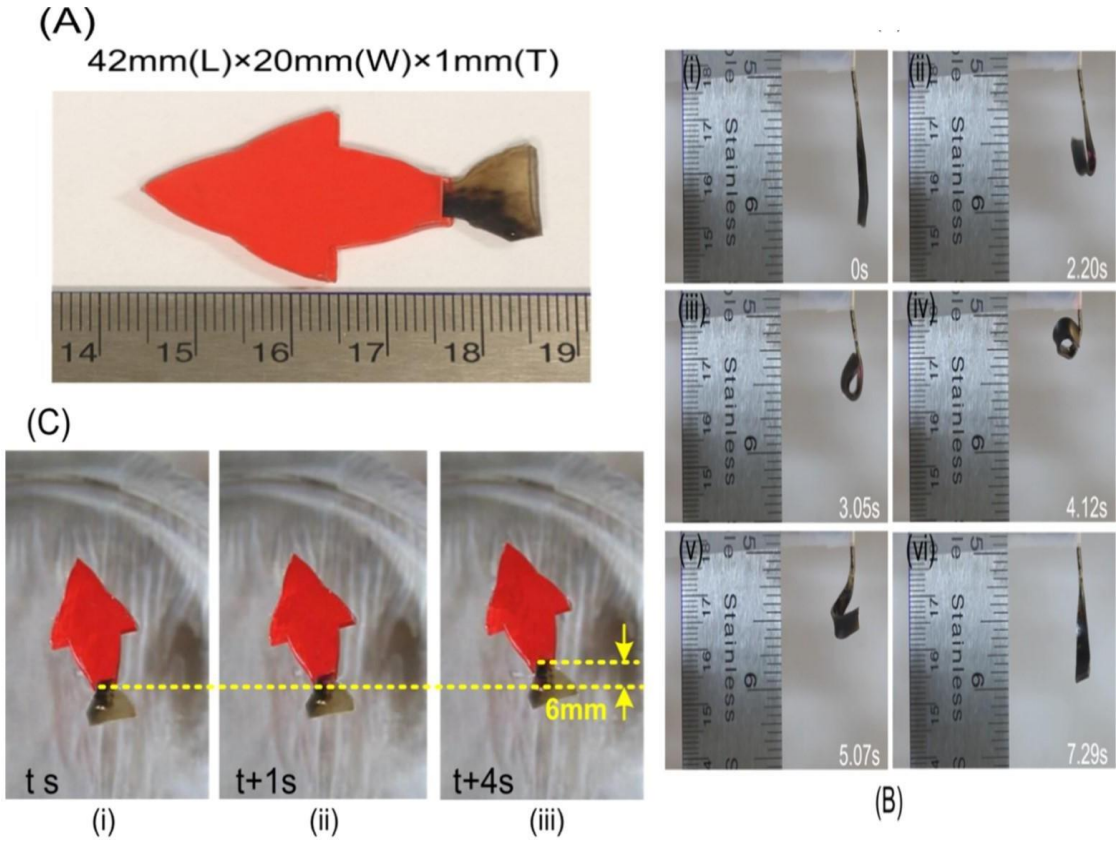

Figure 12. Hongmiao & co-workers have introduced optically driven active materials enable remote, precise, and contactless control of motion and deformation. (A) Geometry of the designed soft robotic swimmer. (B) Rolling up of PDA-coated monodomain LCE film with light scanning on the surface of a film from bottom to top. At 4.12 s, the laser was turned off and the PDAcoated LCE film recovered back to its original flat shape within 3 s. (C) Measurement of the swimming distance during one swimming stroke, and the swimming

distance of the swimmer as a function of time. Figures were taken from reference 44 and reprinted with copyright permission from ACS/RSC/ELSEVIER.

Recently in 2016, Jue & co-workers have introduced an achieving complex, tunable mechanical actuation in response to environmental stimuli is crucial for many advanced applications. This study presents a versatile strategy to create various photomechanical motions—ranging from bending to 3D helical buckling—by controlling the orientation of one-dimensional nanomaterials. Inspired by plant mechanisms, the actuators mimic natural motion by manipulating aligned nanostructures similar to cellulose fibrils. These actuations occur within milliseconds and can be repeated over 100,000 cycles without fatigue. The technology enables sophisticated integrated movements, demonstrated through a light-controlled robotic arm and a solar energy harvesting system. This approach offers a scalable fabrication method and a framework for designing advanced photo responsive devices with diverse, programmable motions.

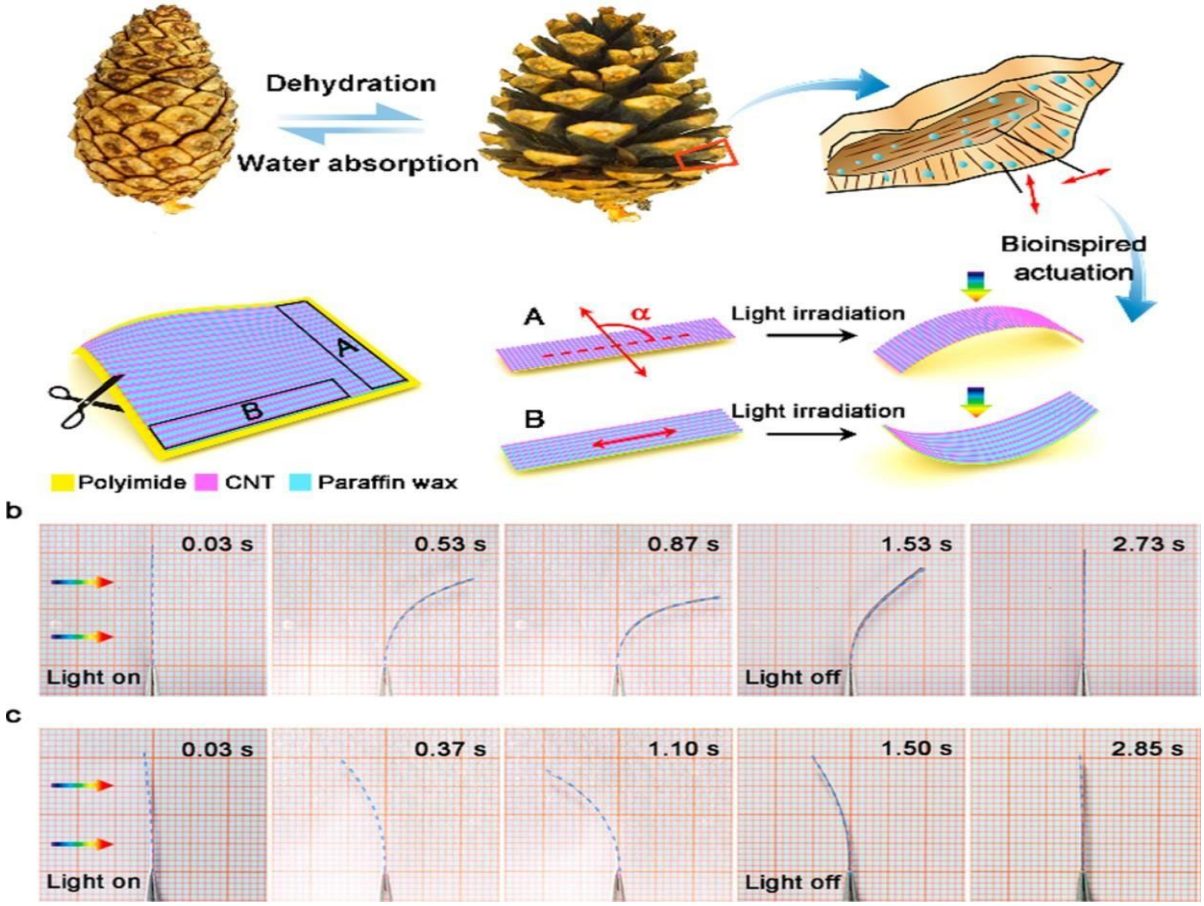

Figure 13. Schematic illustration of the apheliotropic and phototropic bending of the composite strips with different aligned directions of CNTs.(b) Photographs of Strip A (length

of 20 mm, width of 4 mm, and thickness of 23 μm) in response to visible light (illuminated from the left, with an intensity of 100 mW cm−2). (c) Photographs of Strip B in response to visible light. Figures were taken from reference 45 and reprinted with copyright permission from ACS/RSC/ELSEVIER.

Recently in 2018, Jianbo & co-workers have introduced photomechanical molecular crystals (PMMCs) based on SQDPA that respond to light with multimodal motions such as translation, rotation, and jumping. These motions are precisely controlled by adjusting the laser beam's position, intensity, and polarization. Unlike previous methods requiring dual beams or heat, this system uses a single 400 nm femtosecond laser to induce motion. The mechanism involves ultrafast conical internal conversion, which enables rapid and reversible molecular conformational changes. A notable demonstration includes rotating a cross-shaped crystal at over 2 Hz by rotating the laser's polarization. This advancement opens pathways for light-controlled micro robots and energy-harvesting devices.

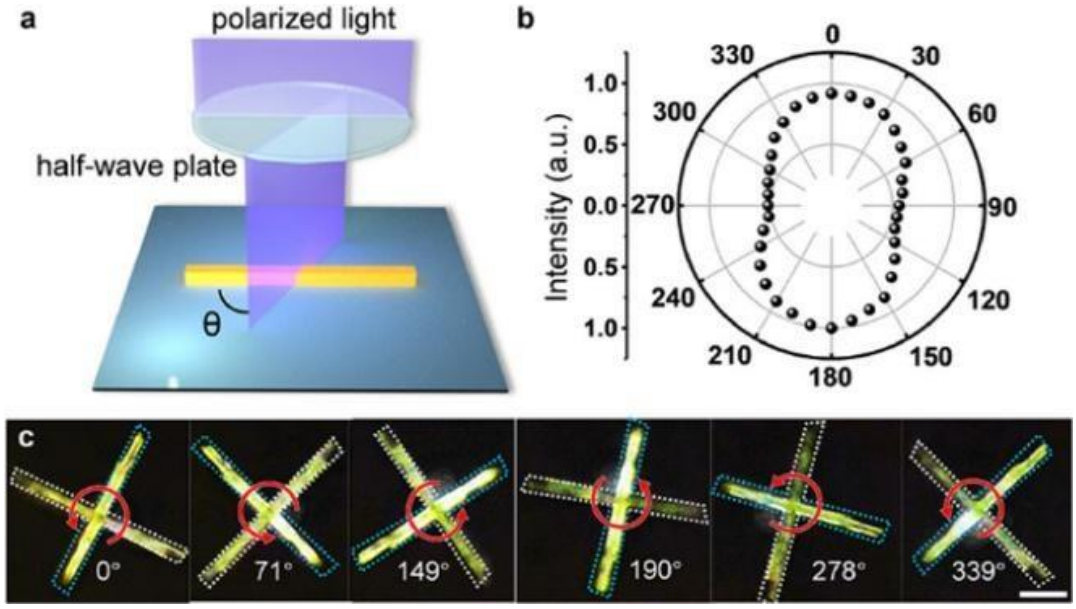

Figure 13. Recently in 2018, Jianbo & co-workers have introduced photomechanical molecular crystals (PMMCs) based on SQDPA that respond to light with multimodal motions such as translation, rotation, and jumping. (a) Schematic illustration of the measurement setup for polarized excitation. The angle, θ, refers to the relative angle between the polarization of the excitation laser and the length direction of SQDPA pMCs. (b) Normalized fluorescence emission intensity as a function of θ = 0−360°. (c) Snapshots show the rotation of a crossshaped sample consisting of two pMCs by rotating the polarization of the laser. The

rotation angle is determined by the brighter crystal(blue dashed line). Figures were taken from reference 46 and reprinted with copyright permission from ACS/RSC/ELSEVIER.

Recently in 2012, Fumitaka & co-workers have introduced wireless molecular-crystal actuators that function under light, eliminating the need for wires unlike traditional piezoelectric crystals. These rodlike mixed crystals bend rapidly and reversibly when exposed to alternating UV (365 nm) and visible light (>500 nm). The bending is fatigue-resistant and occurs at sizes from micrometers to millimeters, making them suitable for miniaturized applications. Unlike polymer-based artificial muscles, this system translates molecular-level structural changes into macroscopic mechanical motion**.** A striking demonstration includes the crystal hitting and rotating a gearwheel upon UV light exposure, showcasing actual photomechanical work. This advancement represents a step forward in creating light-powered, wire-free microactuators.

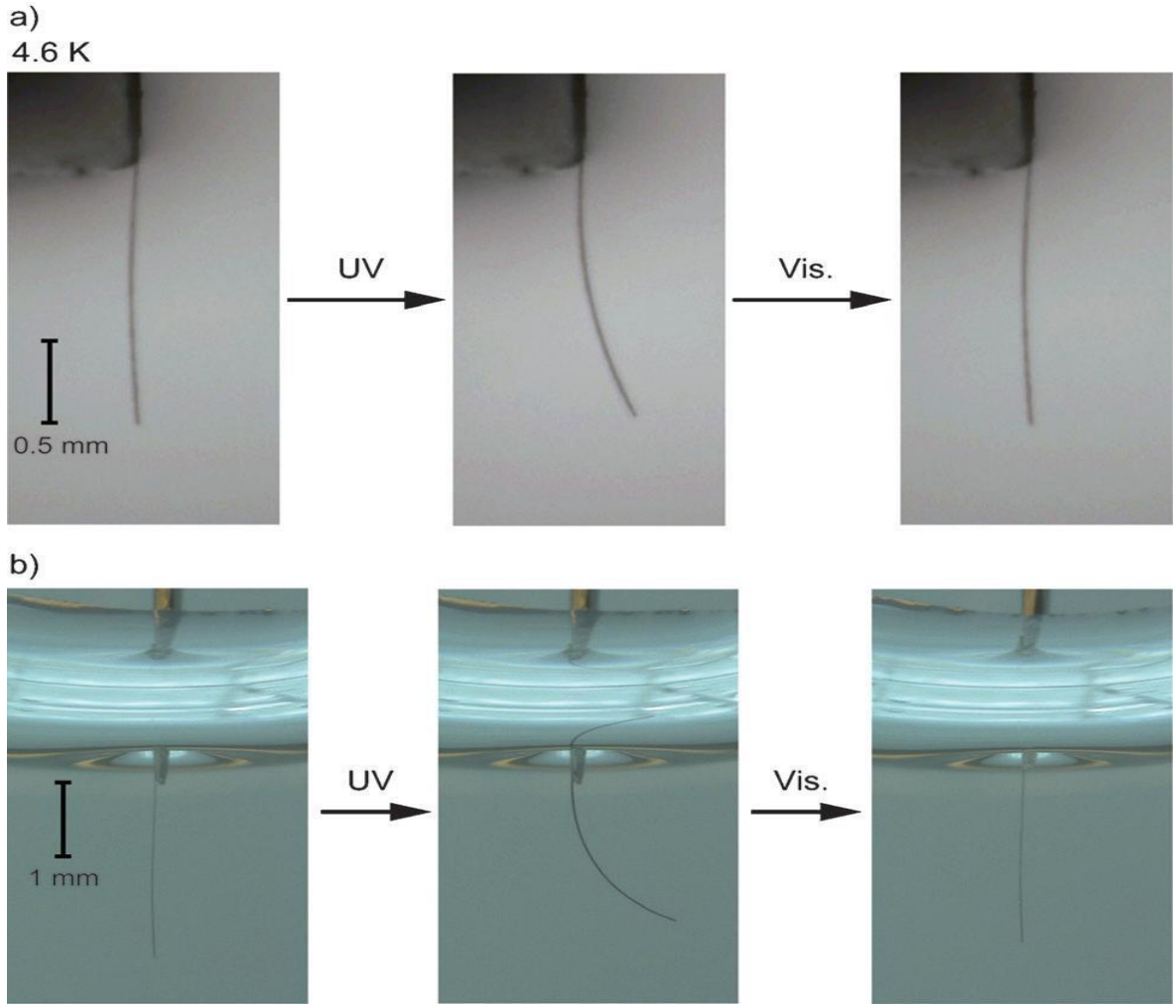

Figure 14. Recently in 2012, Fumitaka & co-workers have introduced wireless molecular-crystal actuators that function under light, eliminating the need for wires unlike traditional piezoelectric crystals. Bending of the rodlike two-component mixed crystal containing 1a and

2a (1a:2a=63/37) at 4.6 K and in water. Figures were taken from reference 47 and reprinted with copyright permission from ACS/RSC/ELSEVIER.

Recently in 2020, Hamed & co-workers have introduced light-driven, untethered soft robots inspired by aquatic invertebrates like sea slugs and snails. Using monolithic liquid crystal gels (LCGs) with intrinsic light responsiveness and molecular anisotropy, the researchers achieved diverse underwater motions, including crawling, walking, jumping, and swimming. These motions result from spatiotemporally controlled optical stimulation, which induces localized deformations and wave-like bending. The LCGs respond quickly due to their low transition temperatures, offering advantages over purely photochemical systems. Their high deformability, anisotropic mechanical properties, and fast response make them promising for applications in biomedical devices and fluidic environments. This work lays the foundation for the development of programmable, untethered soft aquatic robots capable of complex locomotion and navigation.

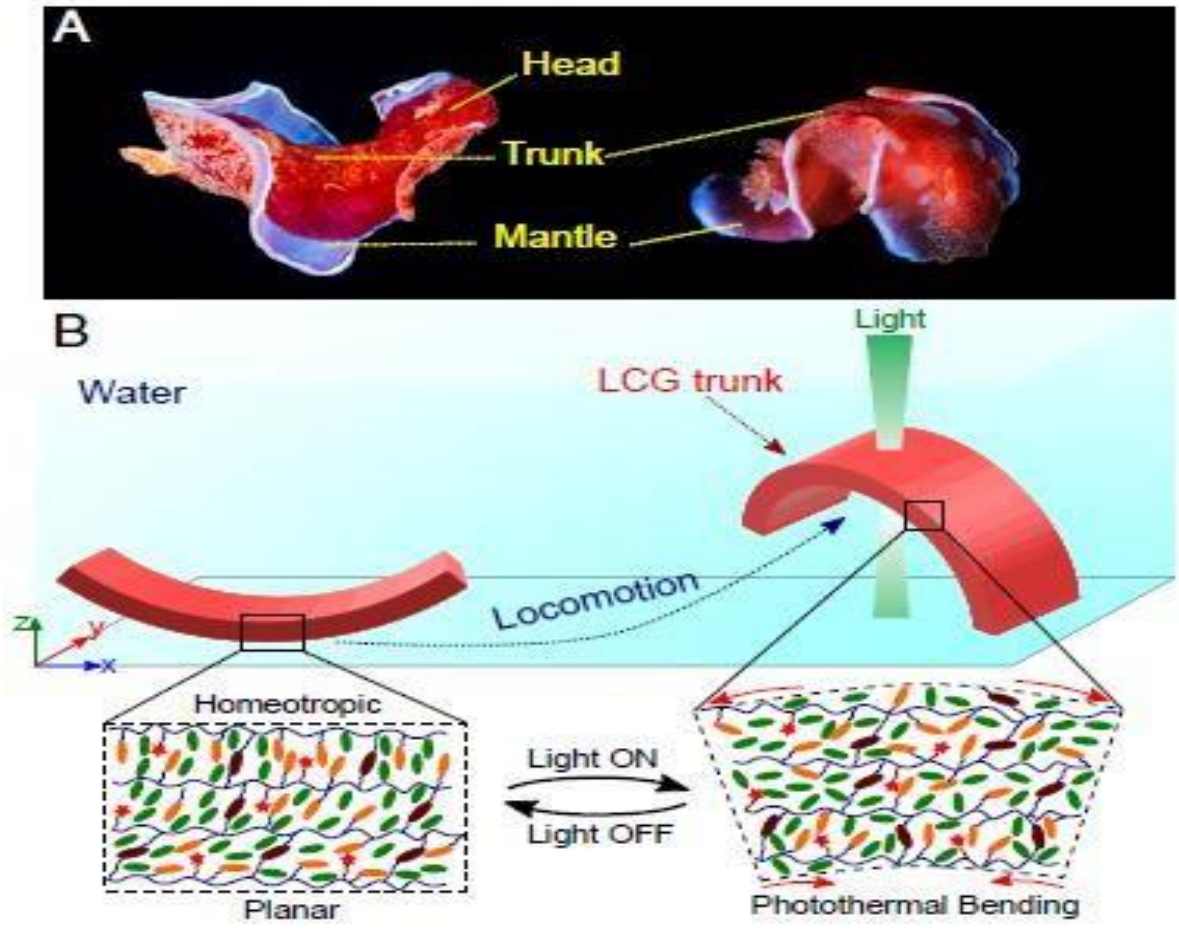

Figure 15. Recently in 2020, Hamed & co-workers have introduced light-driven, untethered soft robots inspired by aquatic invertebrates like sea slugs and snails. Shape morphing in a sea slug and artificial monolithic analogs from LCGs. Figures were taken from reference 48 and reprinted with copyright permission from ACS/RSC/ELSEVIER.

Recently in 2020, Fei & co-workers have introduced a novel photomechanical behaviuor in cis-DMAAM microcrystals**,** which exhibit controlled, light-induced delamination. When exposed to a 405 nm light pulse, part of the crystal undergoes photo-isomerization to the trans form, creating an amorphous cis-trans layer that peels away from the parent block. Unlike uncontrolled fracturing seen in larger crystals, this peeling is reproducible and localized, enabled by precise control over crystal shape and size through surfactant-directed growth. The phenomenon offers a new approach to harnessing photomechanical responses without damaging the material's integrity. This controlled peeling could be applied in adhesives, mechanical switching, or self-renewing surfaces. Overall, the work introduces a promising strategy for achieving functional, repeatable light-driven crystal transformations.

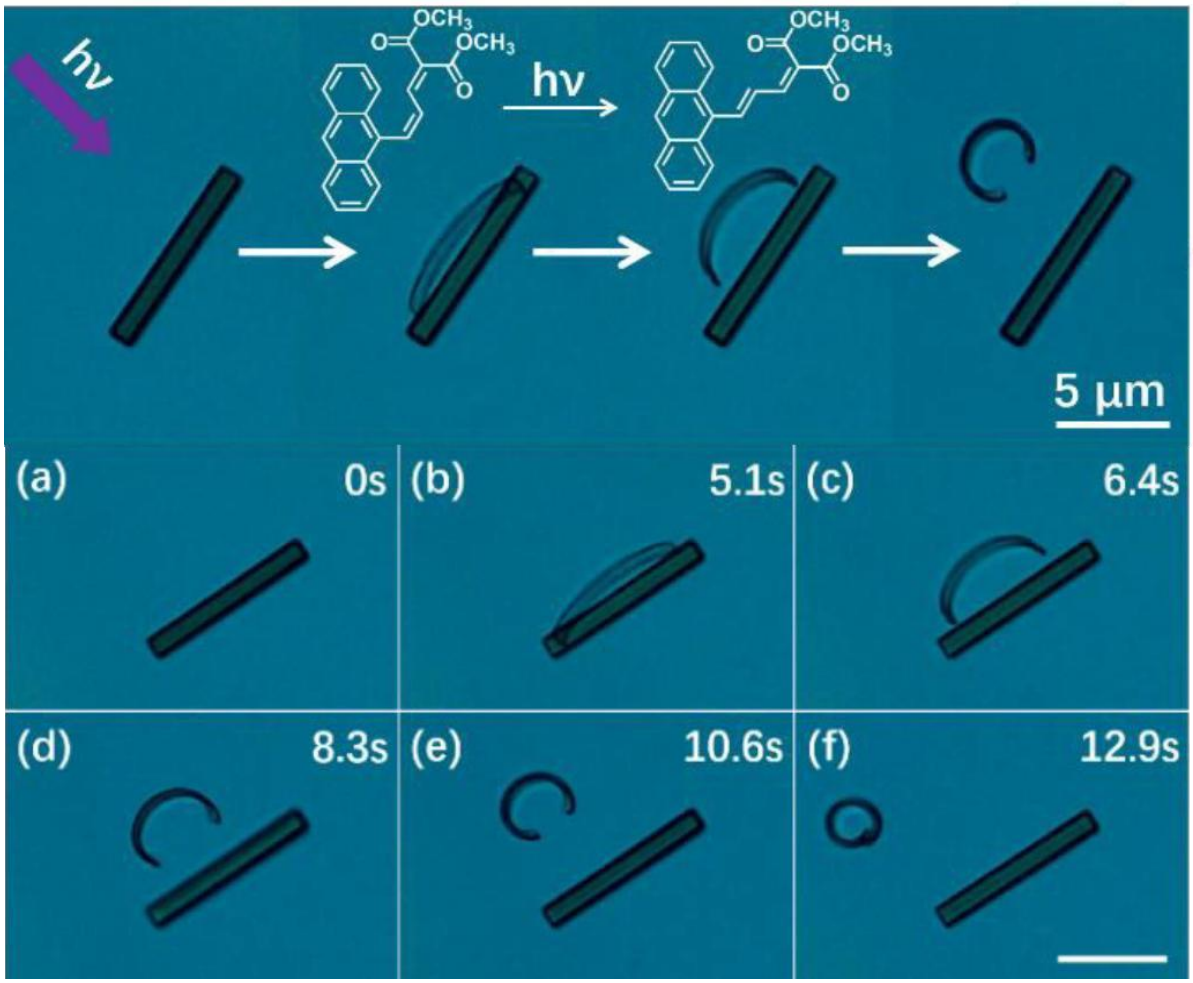

Figure 16. Recently in 2020, Fei & co-workers have introduced a novel photomechanical behaviour in cis-DMAAM microcrystals**,** which exhibit controlled, light-induced delamination. Sequence of optical microscopy images of a *cis*-**DMAAM** microcrystal undergoing photoinduced peeling Process. Figures were taken from reference 49 and reprinted with copyright permission from ACS/RSC/ELSEVIER.

References

[1]. H. Son, C. Yoon, *Actuators* 2020, ***9*(4)**, 115; https://doi.org/10.3390/act9040115.

[2]. M. Karg, A. Pich, T. Hellweg, T. Hoare, L.A. Lyon, J.J. Crassous, D. Suzuki, R.A. Gumerov, S. Schneider, I.I. Potemkin, et al. *Langmuir* 2019, **35**, 6231–6255.

[3]. C.X. Ma, W. Lu, X.X. Yang, J. He, X.X. Le, L. Wang, J.W. Zhang, M.J. Serpe, Y.J. Huang & T.Chen, *Adv. Funct. Mater*. 2018, **28**, 7.

[4]. S.G. Roy, P.De, *J. Appl. Polym. Sci*. 2014, **131**, 12.

[5]. L.L. Yu, M.J. Cheng, M.M. Song, D.Q. Zhang, M. Xiao, F. Shi, *Adv. Funct. Mater.* 2015, **25**, 5786–5793.

[6]. X. Lu, H. Zhang, G. Fei, B. Yu, X. Tong, H. Xia, Y. Zhao, *Adv. Mater.* 2018, **30**, e1706597.

[7]. M. Lahikainen, H. Zeng, A. Priimagi, *Nat. Commun*. 2018, **9**, 4148.

[8]. N. An, M. Li, J. Zhou, *Soft Mater*. 2018, **16**, 151–159.

[9]. M.E. Giannaccini, C. Xiang, A. Atyabi, T. Theodoridis, S. Nefti-Meziani, S. Davis, *Soft Robot*. 2018, **5**, 54–70.

[10]. A.A. Calderon, J. C. Ugalde, L. Chang, J. Cristobal Zagal, N.O. Perez-Arancibia, *Bioinspir. Biomim*. 2019, **14**, 1–19.

[11]. C. Dong, B. Chen, *Proc. Math. Phys. Eng. Sci.* 2017, **473**, 20170092.

[12]. T.H. Lee, J.Y. Jho, *Macromol. Res.* 2018, **26**, 659–664.

[13]. Y. Xiao, B. Wu, Z. Liu, L. Jiang, J. Lei, R. Wang, *J. Appl. Polym. Sci.* 2018, **136**, 1–6.

[14]. S. Zhou, F. Cun, Y. Zhang, L. Zhang, Q. Yan, Y. Sun, W. Huang, *J. Mater. Chem. C* 2019, **7**, 7609–7617.

[15]. M. Yang, Z. Yuan, J. Liu, Z. Fang, L. Fang, D. Yu, Q. Li, *Adv. Opt. Mater.* 2019, **7**, 1–30.

[16]. M.P. da Cunha, Y. Foelen, R.J.H. van Raak, J.N. Murphy, T.A.P. Engels, M.G. Debije, A. Schenning, *Adv. Opt. Mater.* 2019, **7**, 1–8.

[17]. H. Shao, S. Wei, X. Jiang, D.P. Holmes, T.K. Ghosh, *Adv. Funct. Mater.* 2018, **28**, 1–9.

[18]. Y. Wu, J.K. Yim, J. Liang, Z. Shao, M. Qi, J. Zhong, Z. Luo, X. Yan, M. Zhang, X. Wang, *Sci. Robot. Res. Artic.* 2019, **4**, 1–9.

[19]. S.B. Choi, H.C. Kim, C. Han, P. Kim, *Sens. Actuator A—Phys.* 2015, **235**, 281–291.

[20]. L. Engel, O. Berkh, K. Adesanya, J. Shklovsky, E. Vanderleyden, P. Dubruel, Y. Shacham-Diamand, S. Krylov, *Sens. Actuator B—Chem*. 2014, **191**, 650–658.

[21]. M. Medina-Sánchez, V. Magdanz, M. Guix, V.M. Fomin, O.G. Schmidt, *Adv. Funct. Mater.* 2018, **28**, 1707228.

[22]. C. Xiang, J. Guo, J. Rossiter, *Smart Mater. Struct.* 2019, **28**, 055034.

[23]. B.D. Lou, Y.J. Ni, M.H. Mao, P. Wang, Y. Cong, *Robotics* 2017, **6**, 30.

[24]. A. Fekih, S. Mobayen, C.-C. Chen, *Energies* 2021, **14**, 1791.

[25]. A. De Greef, P. Lambert, A. Delchambre, *Precis. Eng.-J. Int. Soc. Precis. Eng. Nanotechnol.* 2009, **33**, 311–321.

[26]. L. Zhang, G. Bao, Q. Yang, F. Gao, *China Mech. Eng.* 2008, **19**, 2891–2897.

[27]. Z. Cai, Z. Song, L. Guo, *ACS Appl. Mater. Interfaces* 2019, **11**, 12770–12776.

[28]. S. Ikejiri, Y. Takashima, M. Osaki, H. Yamaguchi, A. Harada, *J. Am. Chem. Soc.* 2018, **140**, 17308–17315.

[29]. X. Pang, J. Lv, C. Zhu, L. Qin, Y. Yu, *Adv. Mater.* 2019, **31**, e1904224.

[30]. P. Zhang, B. Wu, S. Huang, F. Cai, G. Wang, H. Yu, *Polymer* 2019, **178**, 121644.

[31]. W. Shen, B. Du, J. Liu, H. Zhuo, C. Yang, S. Chen, *Mater. Chem. Front.* 2021, **5**, 3192–3200.

[32]. B. Chen, R. Zhang, Y. Hou, J. Zhang, S. Chen, Y. Han, X. Chen, X. Hou, *Light Sci. Appl.* 2021, **10**, 127.

[33]. M.P. da Cunha, M.G. Debije, A.P.H.J. Schenning, *Chem. Soc. Rev.* 2020, **49**, 6568–6578.

[34]. D. E. Hagaman, S. Leist, J. Zhou & H.-F. Ji, *ACS Appl. Mater. Interfaces* 2018, **10**, 27308−27315.

[35]. J. Lin, J. Zhou, L. Li, I. Tahir, S. Wu, P. Naumov & J. Gong, *Chem. Mater.* 2024, **36**, 8338−8348.

[36]. M. Liu, G. Guo, Z. Liu, Y. Yuan & H. Zhang, *Reactive and Functional Polymers* 2023, **182**, 105458.

[37]. Y. Deng, Q. Zhang, T. Nie, F. Xu, R. Costil, X.-Q. Gong, H. Tian, B. L. Feringa & D.-H. Qu, *Adv. Optical Mater.* 2022, **10**, 2101267.

[38]. H. Li & J. Wang, *ACS Appl. Mater. Interfaces* 2019, **11**, 10218−10225.

[39]. O. M. Wani, H. Zeng & A. Priimagi, *Nature Communications* 2017, 8:15546 | DOI: 10.1038/ncomms15546.

[40]. W. Li, T. J. Gately, D. Kitagawa, R. O. Al-Kaysi & C. J. Bardeen, *J. Am. Chem. Soc.* 2024, **146 (47)**, 32757-32765. DOI: 10.1021/jacs.4c12670.

[41]. U. Kurakula, A. Ekka, B. Dutta, M. H. Mir, N. R. Halcovitch & R. Medishetty, *Cryst. Growth Des.* 2024, **24**, 7066−7074.

[42]. M. B. Al-Handawi, P. Commins, A. S. Dalaq, P. A. Santos-Florez, S. Polavaram, P. Didier, D. P. Karothu, Q. Zhu, M. Daqaq, L. Li & P. Naumov, *Nature Communications* 2024, 15:8095. https://doi.org/10.1038/s41467-024-51625-x

[43]. J. Qin, K. Chu, Y. Huang, X. Zhu, J. Hofkens, G. He, I. P. Parkin, F. Lai & T. Liu, *Energy Environ. Sci*., 2021, **14**, 3931. DOI: 10.1039/d1ee00587a

[44]. H. Tian, Z. Wang, Y. Chen, J. Shao, T. Gao & S. Cai, *ACS Appl. Mater. Interfaces* 2018, **10**, 8307−8316.

[45]. J. Deng, J. Li, P. Chen, X. Fang, X. Sun, Y. Jiang, W. Weng, B. Wang & H. Peng, *J. Am. Chem. Soc.* 2016, **138**, 225−230. DOI: 10.1021/jacs.5b10131

[46]. J. De, Q. Liao, X. Xiao, H. Liu, W. Chen, L. Chen, H. Geng, Y. Liao & H. Fu, *ACS Appl. Mater. Interfaces* 2020, **12**, 27493−27498.

[47]. F. Terao, M. Morimoto & M. Irie, *Angew. Chem. Int. Ed*. 2012, **51**, 901 –904. DOI: 10.1002/anie.201105585

[48]. H. Shahsavan, A. Aghakhani, H. Zeng, Y. Guo, Z. S. Davidson, A. Priimagi & M. Sitti, PNAS, 2020 ,**117(10)**, 5125–5133. www.pnas.org/cgi/doi/10.1073/pnas.1917952117

[49]. F. Tong, M. Al-Haidar, L. Zhu, R. O. Al-Kaysi & C. J. Bardeen, *Chem. Commun*., 2019,**55**, 3709-3712. DOI: 10.1039/C8CC10051A.

CHAPTER-2

Rapid and Versatile Macroscopic Movement by a Green Fluorescent Organic Crystal under Light Illumination

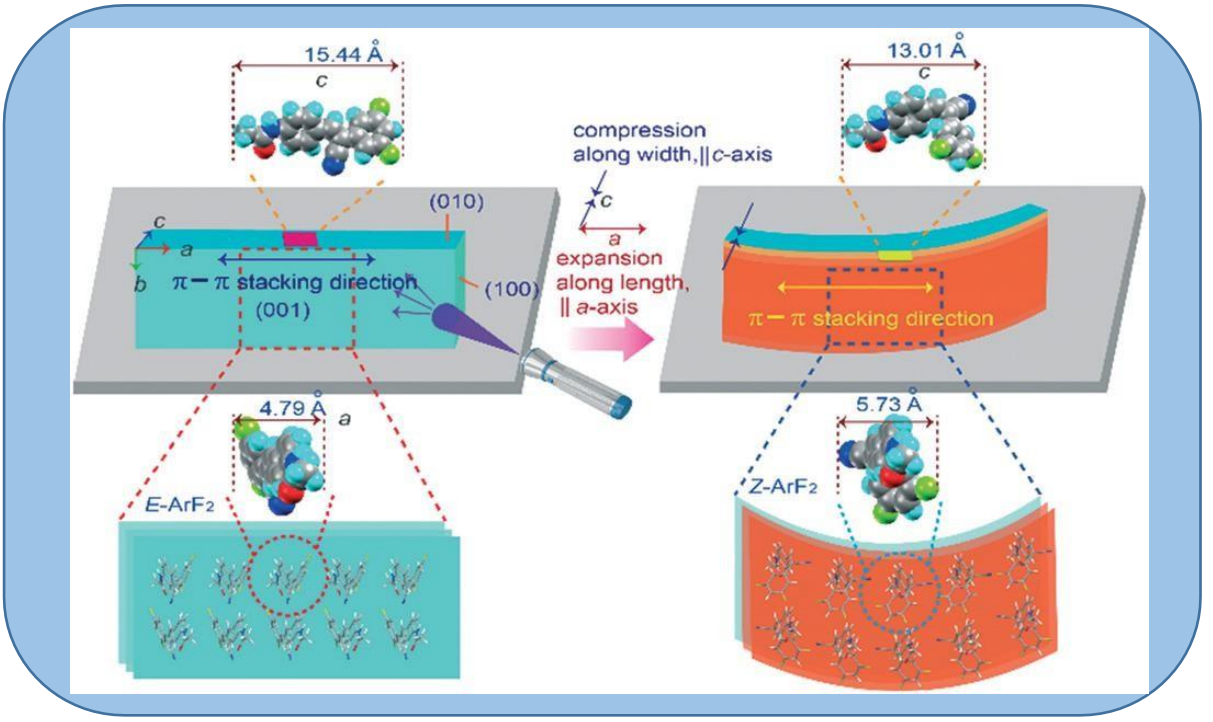

CHAPTER-2

Rapid and Versatile Macroscopic Movement by a Green Fluorescent Organic Crystal under Light Illumination

2.1. Introduction

One of our goal of this project was to design and synthesize molecules that are expected to have light-responsive actuation property. Although many azobenzene based molecules have already been reported in literature, the necessity of developing new molecules having novel physical property seems to be a never-ending effort. Compared to azobenzene-based actuators, acylhydrazones based molecules or cyanovinyl based molecules are comparatively new and thus have a better scope to be explored to a greater extent. Moreover, by changing the functional group and substituent group in the molecule, we can attain a diverse range of molecules that could have tunable optical as well as actuation property. In this report, we have described our recent published work on cyanovinyl derivative based molecule, the crystal of which exhibited light fuelled movement in bulk scale. Our rationale behind designing the molecule is to keep the photoactive functional (C=C-CN) in the core with an auxiliary functional group (F/Cl etc) or substituents that can engage in non-covalent interaction for facile supramolecular reconfiguration during photo isomerization.

Smart responsive materials that are capable of transforming light, heat, pressure or hygro stimuli into macroscopic motion are of immense importance in fundamental and technological research.[1–12] Among the various stimuli generally being used, light has special importance because of the advantage that it can be remotely controlled to manipulate the properties of the material. Certain molecular crystals have extraordinary ability to transform light-triggered molecular motion into macroscopic actuation[13–20] and thus can be used in soft robotics, machinery devices, medical devices, artificial muscles, etc. It is notable to mention here that molecular cooperativity is important to amplify such nanoscopic molecular motion into macroscopic actuation. Among various reports of such molecular crystals (organic/metal–organic), the majority of them contain azobenzene,[21–25] anthracene,[26–28] salicylidenephenylethylamines,[29,30] a styryl benzene ring,[31–36] and diarylethene[37,38] molecules as the photoactive functional group and are capable of displaying macroscopic actuation when UV light is shone on them. The macroscopic motions in these crystals are rooted to photoinduced geometric isomerization, photocycloaddition, ringopening/closing reactions,

phase transitions, etc. that occur in the light illuminated surface and thereby generating a bimorphic strain that drives the crystal shape deformation followed by actuation. Recently, a new class of crystals based on acylhydrazone molecules that exhibit photomechanical actuation is reported.[39,40] However, to our knowledge, reports on photomechanical crystals based on a cyanovinyl-derivative are really scarce and there exist only a few examples of cyanovinyl based molecules that exhibit photo induced bending.[41–43] Achieving precise control of crystal motion or rapid and on-demand shape deformation using light stimuli remains a formidable challenge. Thus, there is a long-standing demand to develop new molecular materials equipped with light responsive functionality and suitable intermolecular interactions that can exhibit a delicate interplay between light-responsivity and crystal elasticity for rapid and controllable actuation. A rational approach via molecular design and crystal engineering is necessary to develop efficient photo-responsive crystals. Herein, we report a new class of fluorescent organic crystals based on an amide functionalized cyanovinyl derivative (***E*-ArF$_2$**) that displays rapid and on-demand shape deformation in the presence of UV light (390 nm). The molecule contains an amide functional group that is engaged in intermolecular H-bonding interactions while the π–π stacking interaction between the phenyl rings effectively brings the acrylonitrile double bond within the critical distance for [2 + 2] photo-cycloaddition reaction in the solid state. Schmidt criteria for solid state photocycloaddition the reacting double bonds should be parallel and within a close distance (typically around 4.2 Å) for the reaction to proceed readily. The actuation of the ***E*-ArF$_2$** crystal can be precisely controlled by irradiating light on the specific position of the crystal surface or by changing the illumination direction. We establish that the actuation of the ***E*-ArF$_2$** crystal is a macroscopic manifestation of light-fueled *E*- to *Z*-isomerization and the [2 + 2] cycloaddition reaction in the solid-state.

2.2 Experimental

2.2.1. Materials & methods

4-acetamidobenzaldehyde & 3, 5-difluorobenzylcyanide were purchased from TCI India and used as received without further purifications. Tetrabutyl ammonium hydroxide (TBAH), Potassium tert-butoxide acquired from Merck Chemicals, was also used in its commercially available form. For synthesis, Merck ACS-grade solvents were employed, while spectroscopy-grade solvents facilitated crystallization and spectroscopic studies to ensure high-quality results. Several Analytical Techniques Utilized as follows,

NMR Spectroscopy: Both ^{1}H NMR (300 MHz) and ^{13}C NMR spectra were recorded on a Bruker AVANCE 300 spectrometer using $CDCl_3$ or DMSO-d_6 as the solvent. The chemical shifts (δ) are reported in ppm for precision.

Scanning Electron Microscopy (SEM): SEM images of the samples were captured using a FEI INSPECT F50 instrument with an operating voltage of 5 kV. The samples were coated with a thin layer of gold to enhance conductivity and image clarity.

High-Resolution Mass Spectrometry (HRMS): The HRMS of compound ***E*-ArF$_2$** & its dimer were acquired using a QTOF Micro YA263 mass spectrometer operated in electrospray ionization (ESI) mode.

UV-Vis and Fluorescence Spectroscopy: UV-Vis absorption spectra were recorded with a Shimadzu UV-2401C spectrophotometer in solution and solid-state configurations. For fluorescence studies in the solid state, a HORIBA Jobin Yvon Fluorolomax-4 spectrofluorometer was employed. Additionally, lifetime measurements were performed on a Modular Time-Correlated Single Photon Counting (TCSPC) system equipped with a Delta Flex detector (PPD850).

Infrared Spectroscopy (IR): IR spectra were recorded using a PerkinElmer LX-1 FT-IR spectrometer to examine functional group characteristics and molecular interactions.

Powder X-ray Diffraction (PXRD): PXRD patterns were obtained using a Bruker D8 Advanced Diffractometer with Cu Kα radiation (λ = 1.5418 Å), operating at 40 kV and 40 mA. The Lynxeye detector was utilized for data acquisition with a scanning rate of 0.2 seconds per step over a 2θ range of 0° to 50°.

Single Crystal X-ray Diffraction

High-quality single-crystal X-ray diffraction data for ***E*-ArF$_2$** was collected using a Bruker D8 Venture APEX 3 diffractometer equipped with a CCD area detector and MoKα radiation (λ = 0.71069 Å). The SAINT program (version 8.38A) was used for data reduction, and XPREP (within the APEX 3 suite, version 2017.3–0) ensured structural agreement. Absorption corrections were performed with SADABS, and the structures were solved using SHELXT (version 2018/2) and refined with SHELXL-2014. Non-hydrogen atoms were refined

anisotropically, while hydrogen atoms were calculated and refined isotropically. Crystallographic data for ***E*-ArF$_2$** has been deposited at the Cambridge Crystallographic Data Centre (CCDC) under deposition no. 2075638.

2.2.2 Synthesis & Characterizations:

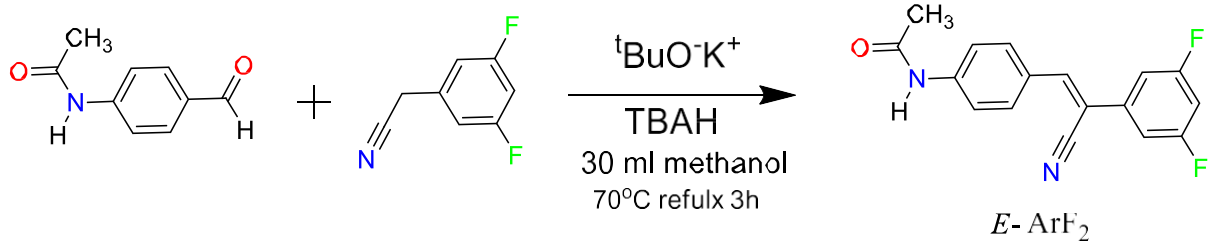

Scheme 1. Synthetic scheme to ***E*-ArF$_2$**

With the aim of developing photomechanical crystal we have first synthesized a cyanovinyl based molecule. The double bond which is introduced by Knoevenagel condensation may undergo photocycloaddition or cis-trans geometrical isomerization reaction. The highly electronegative atoms which are present in ***E*-ArF$_2$** (such as N, O, F) are essential for supramolecular interaction & stabilize the crystal structure. The Compound ***E*-ArF$_2$** was synthesized by Knoevenagel condensation (Scheme 1). A 100 mL round-bottom flask equipped with a magnetic stirrer and reflux condenser was charged with 4-acetamidobenzaldehyde (0.143g, 8.8×10^{-4} mol), 3,5-difluoro benzyl cyanide (0.1 ml ,8.8×10^{-4} mol) in 30 mL of methanol solution. Potassium tert-butoxide (0.148 g, 1.313×10^{-3} mol) and tetrabutyl ammonium hydroxide (TBAH, 25 % methanol solution, 1.3 ml, 1.313×10^{-3} mol) was added to it and the resulting mixture was heated at 70 °C for 4 hours. The product was precipitated from the solution which was filtered and washed with methanol and air dried (0.178 g, 68 %).

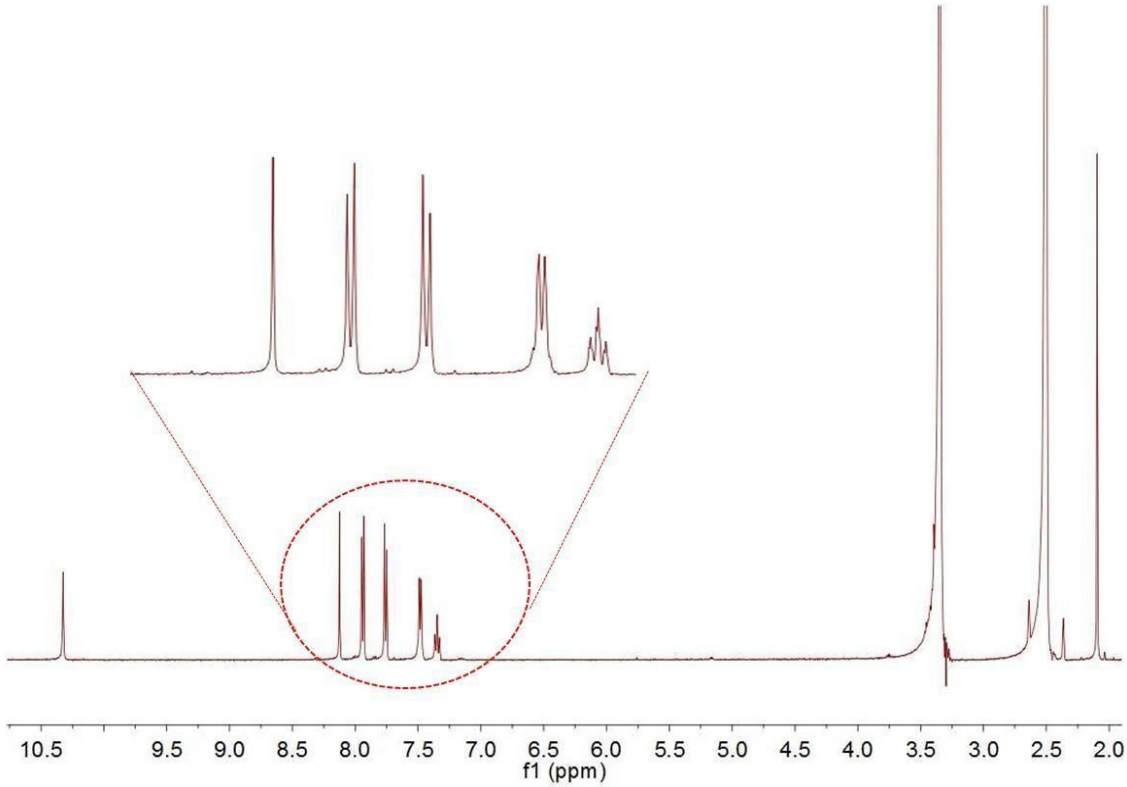

Figure 1. ^{1}H NMR spectra of ***E*-ArF$_2$** in $CDCl_3$ solvent.

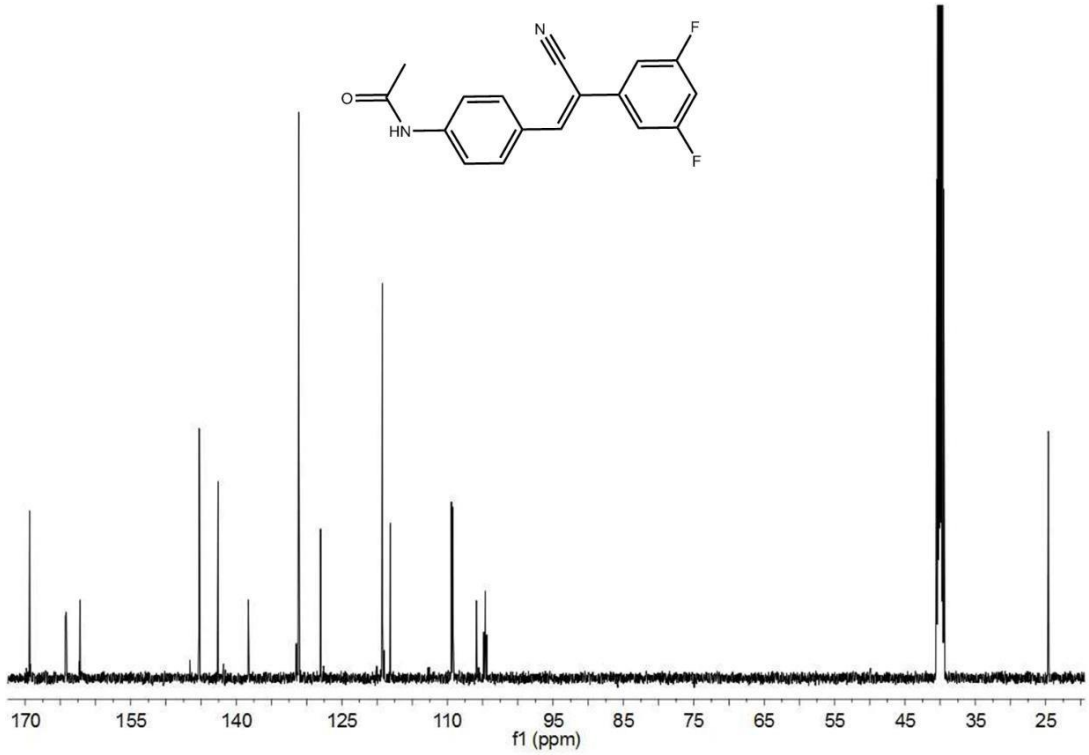

Figure 2. ^{13}C NMR spectra of ***E*-ArF$_2$** in $CDCl_3$ solvent.

For, ^{1}H NMR spectra 5 mg compound is added in 0.6 ml $CDCl_3$ solvent. Then I made a homogeneous solution of the mixture by shaking & slight heating then ^{1}H NMR spectra is recorded. High concentration solution is required for ^{13}C NMR spectra. Approximately 25 mg compound is added to 0.6 ml $CDCl_3$ solvent. Then I made a homogeneous solution of the mixture by shaking & heating then ^{13}C NMR spectra is recorded.

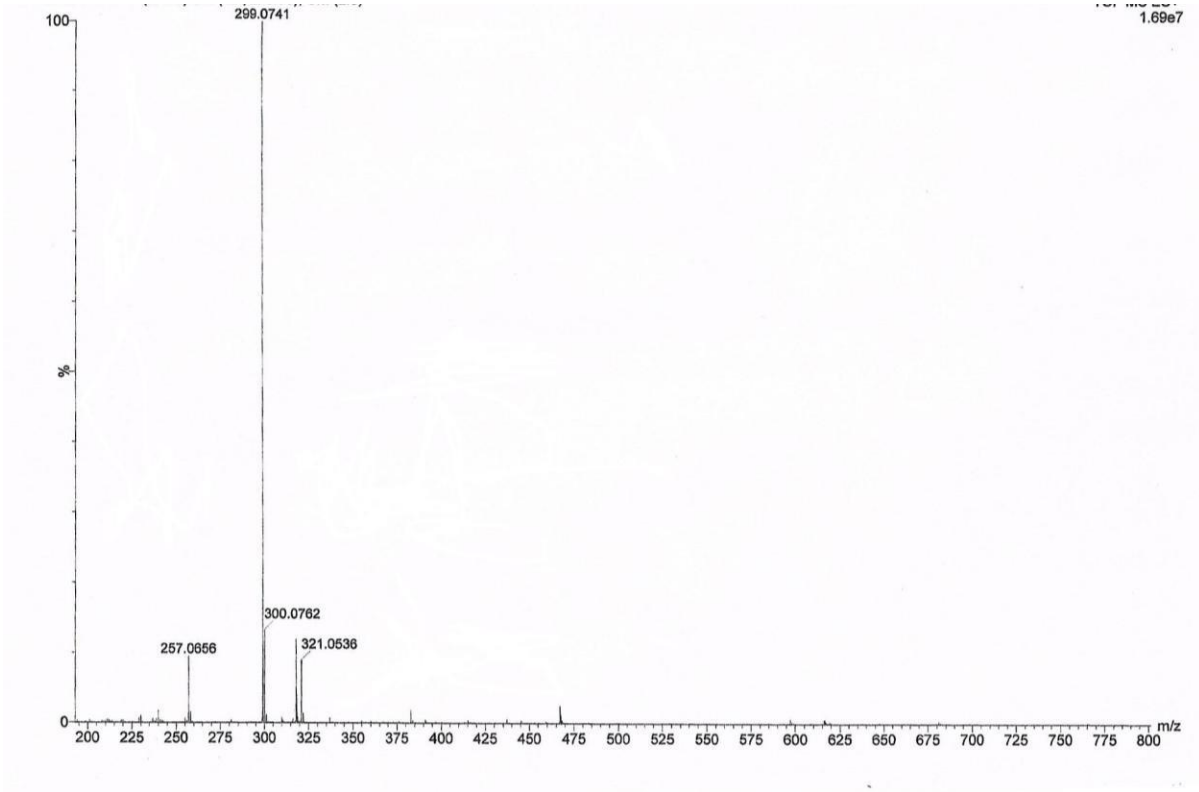

Figure 3. High-resolution mass spectra (HRMS) of compound ***E*-ArF$_2$** showing [M+1] peak at 299.0741 and [M+23] peak at 321.0536.

The compound was thoroughly characterized by ^{1}H NMR,^{13}C NMR, and mass spectrometry (Figure 1–3). ^{1}H NMR (500 MHz, $CDCl_3$): δ (ppm), 10.32 (s, 1H, N*H*), 8.12 (s, 1H, Ar*H*), 7.94 (d, 2H, J= 8Hz, Ar*H*), 7.74 (d, 2H, J= 8 Hz, Ar-*H*), 7.49 (d, 2H, Ar*H*), 7.35 (t, 1H, J= 8 Hz, Ar*H*), 2.10 (s, 3H, C*H*$_3$). ^{13}C NMR (125 MHz, $CDCl_3$) δ (ppm). 169.37, 164.28, 164.17, doublet 162.32, 162.21, 145.27, 142.59, 138.30, 131.12, 128.03, 119.25, 118.11, 109.44, 109.22. 105.92, 104.63, 24.63. HRMS: calculated for $C_{29}H_{18}F_6N_2$ is 298.0918, obtained m/z = 299.0741 (M+H), 321.0536 (M+23).

2.3 Result and Discussion:

The compound **ArF_2** contains only one aliphatic proton ($–CH_3$), while all remaining protons are aromatic. In the ^1H NMR spectrum, the most downfield signal appears at 10.32 ppm and is attributed to the –N**H** proton. Aromatic proton signals are observed within the range of 8.12 to 7.49 ppm, consistent with the expected chemical environment. The aliphatic methyl proton (–C**H**$_3$) gives a distinct singlet at 2.10 ppm. All the observed chemical shifts in the ^1H NMR spectrum are in excellent agreement with the proposed structure of the compound, thereby confirming its identity.

In the ^{13}C NMR spectrum, all aromatic carbon signals are observed within the expected range of 169 to 104 ppm, indicating the presence of a conjugated aromatic system. A distinct peak near 109 ppm is attributed to the nitrile (–C≡N) carbon, which typically resonates in this region due to its strong electron-withdrawing nature and sp-hybridized character. Additionally, the aliphatic carbon signal corresponding to the methyl group (–**C**H_3) appears at 24.63 ppm, consistent with a saturated carbon environment. The observed chemical shifts in the ^{13}C NMR spectrum are in good agreement with the structural features of the compound, further confirming its identity and purity.

High- resolution mass spectra (HRMS) of compound ***E*-ArF_2** was taken to confirm synthesis of my compound. Calculated formula mass of ***E*-ArF_2** ($C_{29}H_{18}F_6N_2$) is 298.0918. HRMS peaks are recorded

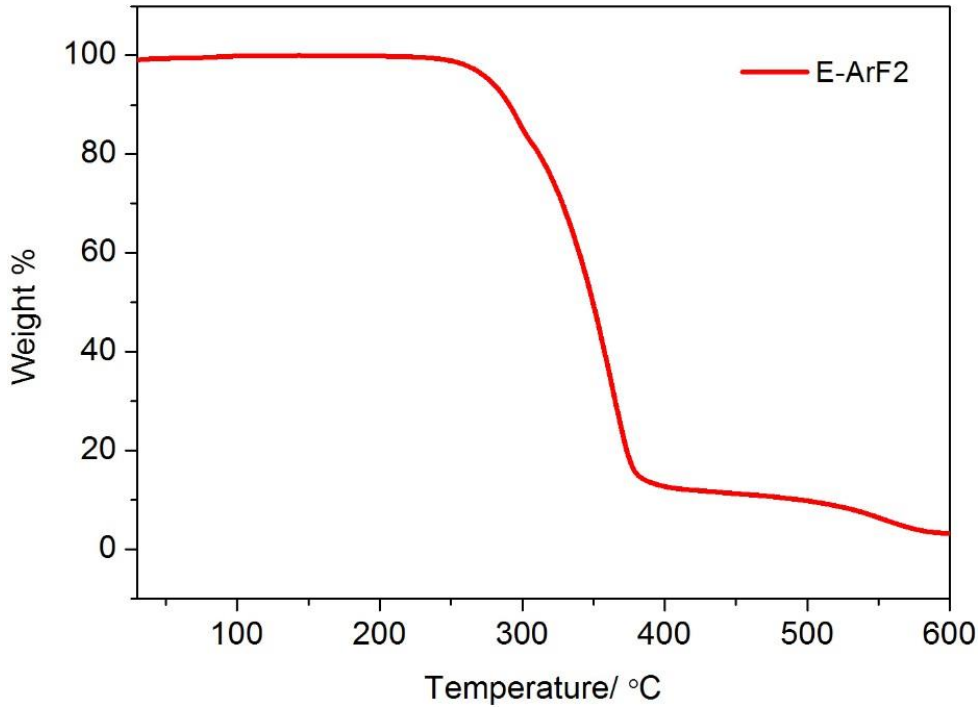

Figure 4. Thermogravimetric analysis (TGA) of ***E*-ArF$_2$** crystal at m/z 299.0741 associated with (M+H) peak & 321.0536 represents (M+23).

Thermogravimetric analysis (TGA) was conducted to evaluate the thermal stability of the compound. The results indicate that the compound remains thermally stable up to approximately 250 °C, with no significant weight loss observed below this temperature. This high decomposition onset temperature reflects the excellent thermal stability of the compound, making it suitable for applications requiring resistance to elevated temperatures.

2.3.1 Solid state actuation property

Thermogravimetric analysis suggests that the compound is thermally stable up to 250 °C (Figure 4). Crystallization of the compound from DMF solution gives fibre like crystals, some of which are inherently bent. The molecular structure of the crystal was confirmed by single crystal X-ray diffraction which reveals the trans (*E)* geometry of two aromatic rings around the acrylonitrile bond (Fig. 1c). When observed under a fluorescence microscope, needle shaped pristine crystals of ***E*-ArF$_2$** emit green light ($\lambda_{em,max}$ = 503 nm, $\phi_{crystal}$ = 0.03, Fig. 1b). The ***E*-ArF$_2$** compound does not show any visually detectable AIE effect in solution (THF : water mixture). The mechanism of actuation is photoinduced *E* to *Z*-isomerization around the double bond of the ***E*-ArF$_2$** molecule in the solid crystal. On heating the photo-bent crystal at 100 °C

for 6 hours, it slowly returned to nearly its original straight shape. According to our knowledge, this is the first example of an acrylonitrile based organic crystal which shows optical response (i.e. green fluorescence) as well as mechanical response (i.e. macroscopic actuation) in the presence a single stimulus, i.e. UV light.

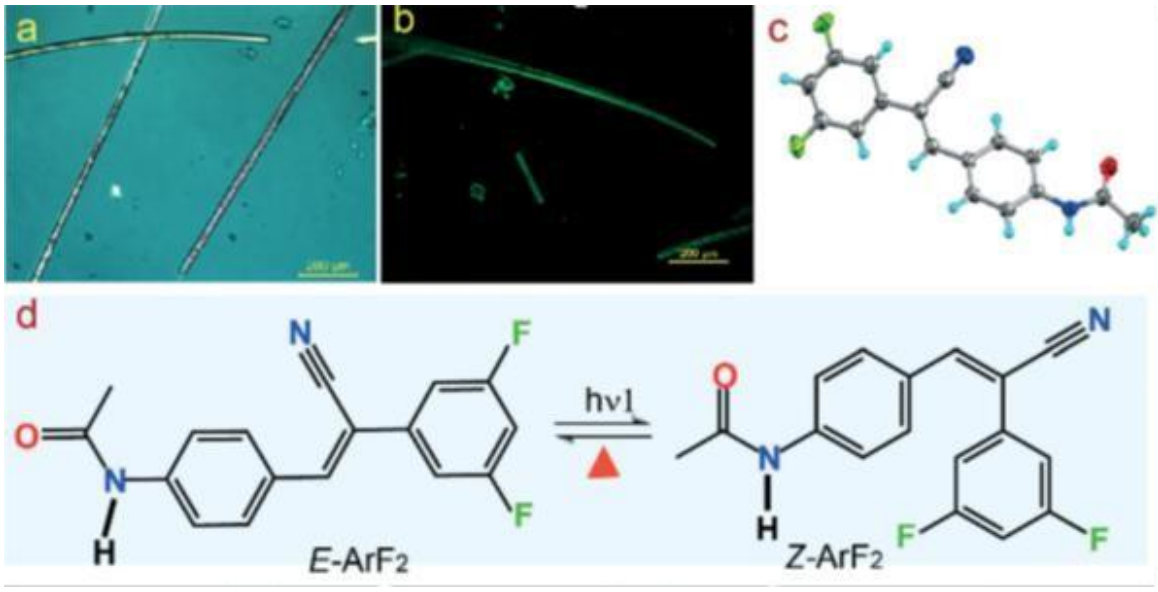

Figure 5. (a) Optical microscope image of the ***E*-ArF$_2$** crystal, (b) image of the ***E*-ArF$_2$** crystal showing green fluorescence, (c) molecular structure of ***E*-ArF$_2$** showing trans-geometry, (d) schematic diagram of *E*- to *Z*-isomerization upon UV irradiation

The fibre like crystal of ***E*-ArF$_2$** undergoes photo-mechanical actuation in presence of UV light (390 nm). These crystals bend away from the direction of the incident light. We have done a systematic study of bending of the crystal. The crystal was placed on a glass slide under the microscope attached with a camera and the video of crystal actuation upon light illumination was recorded. When a thin fibre shaped crystal of ***E*-ArF$_2$** was irradiated with 390 nm light (torch light, power density 5 mW) on the wider (001) face, the crystal instantaneously bends away from the light source. The shape deformation can be manipulated by controlling the illumination at different positions of the crystal. As shown in Fig. 6(a–f), the straight crystal can be gradually bent by a flash of UV light at the specific position on the crystal surface (shown by arrow) and the deflection angle is changed from 0° → 56° → 88° → 142° → 155°

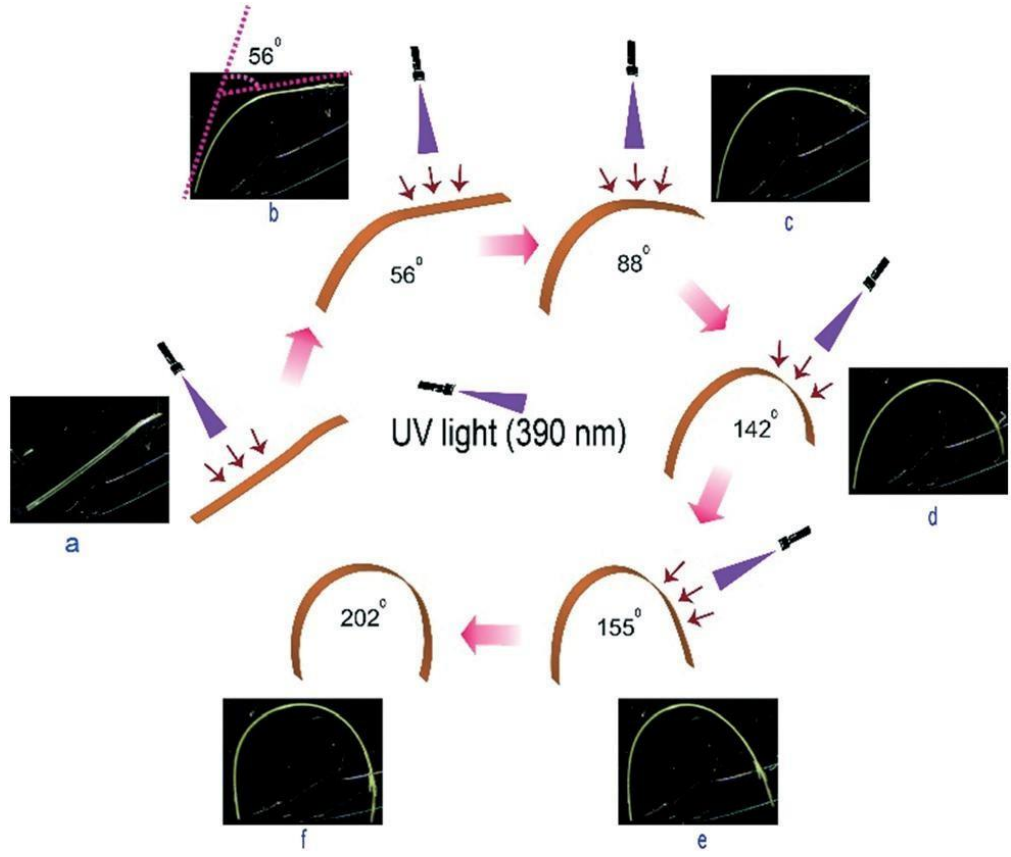

Figure 6. (a–f) Stepwise and controlled bending of a straight ***E*-ArF$_2$** crystal to a U-shape by light irradiation (390 nm) at specific positions. The change in deflection angles is given and the maximum deflection angle of 202° was attained at the bent "U" shape. The image snapshots were extracted from Movie of Actuation of ***E*-ArF$_2$**.

and finally reaches its maximum at ~202° forming a U-shape. As observed under an optical microscope, the U-shaped crystal retained its macroscopic integrity without the formation of any crack or fracture on the surface. The SEM images showed no change in the surface morphology of the crystal surface after the 1st cycle of photomechanical bending.

2.3.2 X-ray Structure and Intermolecular Interactions

Single crystal diffraction was carried out to reveal the 3-D structure of the ***E*-ArF$_2$** crystal. Slow evaporation from DMF solution yielded cuboid shaped orthorhombic crystals with the $P2_12_12_1$ space group. Several intermolecular H-bonding interactions involving (O=C) N–

H···NC, H_2C–H···NC and (NH)C=O···H groups as well as π–π stacking interactions which play an essential role in maintaining crystal integrity during photomechanical bending (Figure 7b).

The carbonyl oxygen of the amide group is connected to two neighbouring antiparallel molecules involving a trifurcated H-bonding interaction (H···A distances are 2.491 Å, 2.593 Å and 2.689 Å) which is extended along the b-axis of the crystal. The nitrogen atom of the CN group also engaged in bifurcated H-bonding interaction (H···A distance 2.675 Å) with the C–H and N–H protons of the neighbouring molecule.

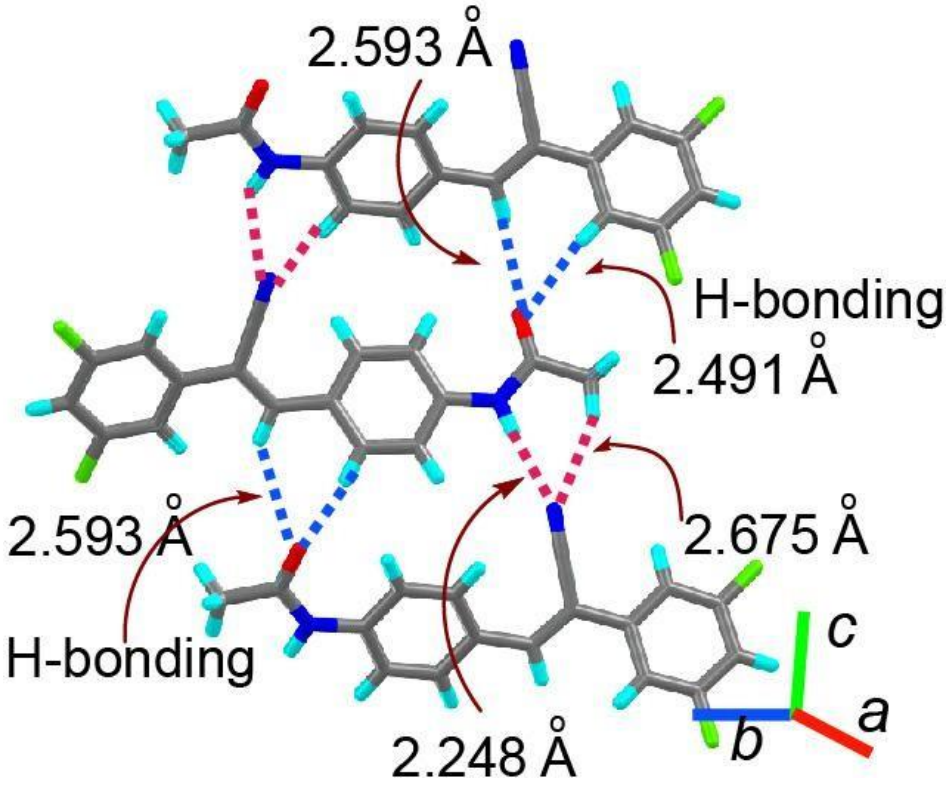

Figure 7. Various types of H-bonding interactions present in ***E*-ArF$_2$** crystal

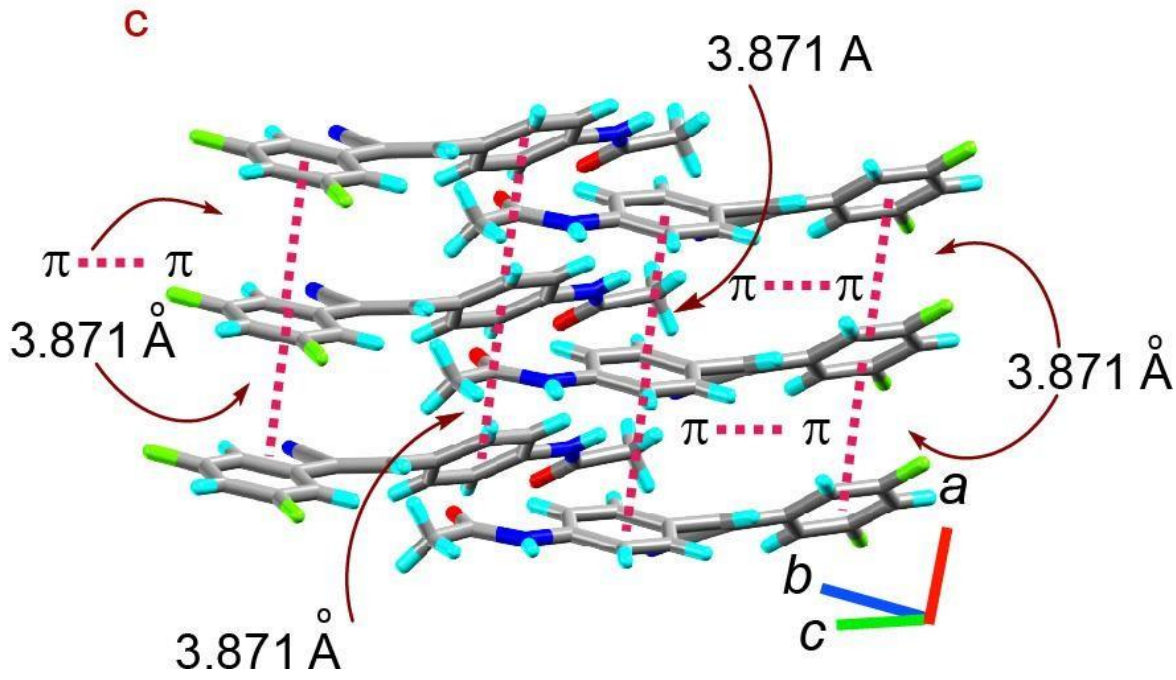

Figure 8. π–π stacking interactions present in ***E*-ArF$_2$** molecule.

The phenyl rings of the ***E*-ArF$_2$** molecule are engaged in π–π stacking interaction in a parallel fashion (centroid to centroid distance 3.871 Å) which is extended along the length (a-axis) of the crystal (Figure 8). This interaction plays an important role in maintaining the crystal integrity during the photomechanical bending. The π–π stacking of the aromatic rings brings the vinylidene double bonds of two neighbouring molecules within the distance of 3.871 Å which is smaller than 4.2 Å and the obtuse angle (<C8–C7–C7′) between these double bonds is 98.67° (Figure 9) and thus, according to Schmidt's criteria this double bond is susceptible to photo- dimerization reaction in the solid crystal. In fact, as mentioned earlier, prolonged or repeated UV irradiation of the crystal leads to a small fraction of the [2 + 2] cycloaddition product. Despite our repeated attempts we were unsuccessful in obtaining a good quality crystal of the photoproduct (photo-irradiated crystal) for X-ray diffraction.

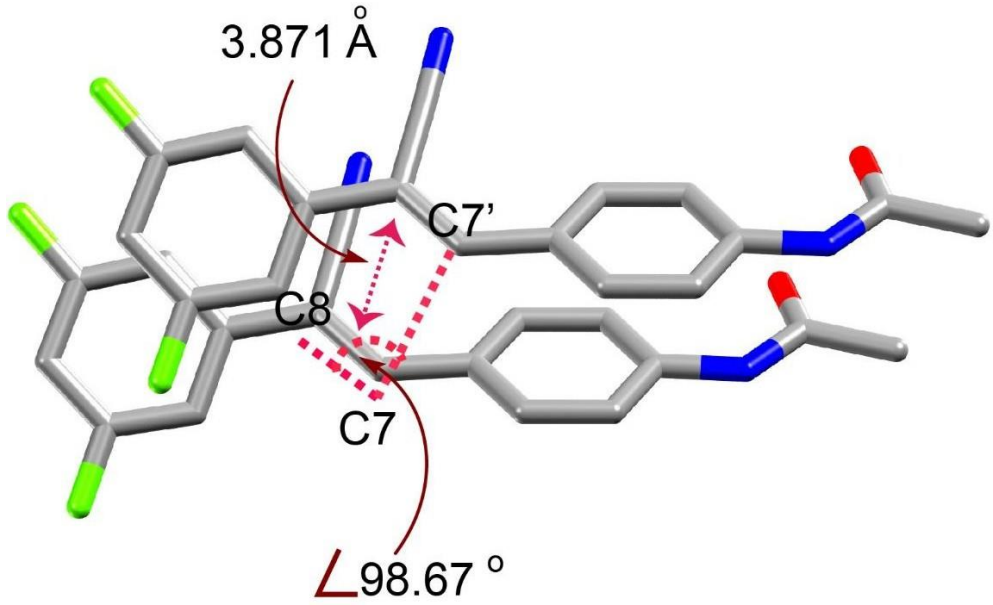

Figure 9. Distance between two olefinic double bond in ***E*-ArF$_2$** crystal that satisfy Schmidt's criteria for photodimerization.

Mechanism of actuation:

To understand the molecular level changes of the macroscopic actuation of the ***E*-ArF$_2$** crystal, we have carried out ^{1}H NMR, UV-vis, PXRD and IR spectroscopy. As observed from the ^{1}H NMR spectra of ***E*-ArF$_2$** (in DMSO-d$_6$ solution), the chemical shift of –N**H** protons at

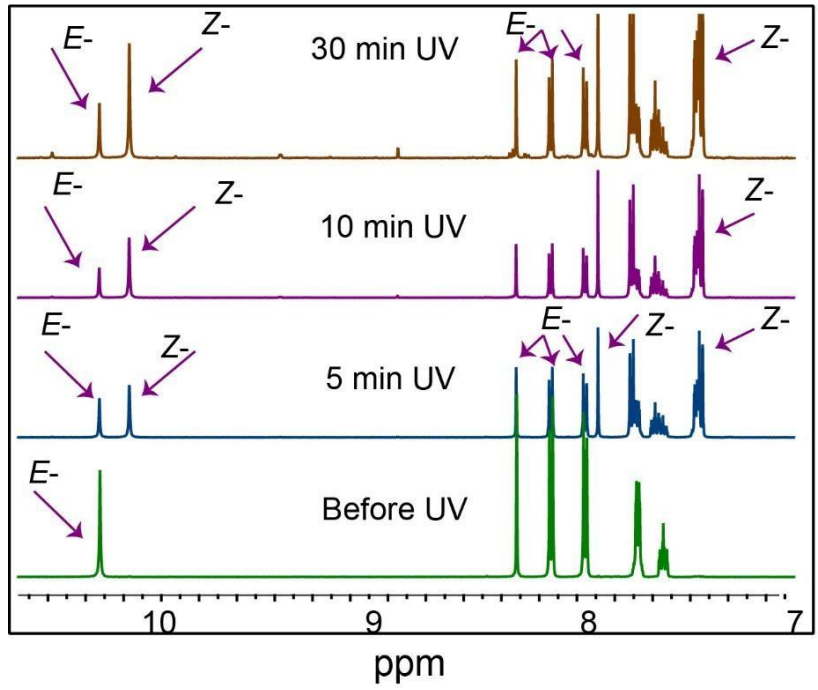

Figure 10. ^{1}H NMR (DMSO-d$_6$) spectra of ***E*-ArF$_2$** before and after UV light irradiation.

10.45 ppm in the *E*-isomer is shifted to the high-field region at 10.32 ppm that corresponds to the *Z*-isomer upon photoirradiation (390 nm LED light, 1 mW, Fig. 10). Similarly, the proton of the CH=C moiety shifted from 8.2 ppm in the *E*-isomer to 7.7 ppm in the *Z*-isomer. By comparing the intensities of NH proton peaks, 71% conversion was observed in 5 minutes of UV irradiation in solution. Longer irradiation of the solution leads to the [2 + 2] cycloaddition product after which no change of peak intensity was observed indicating the attainment of the photostationary state in solution.

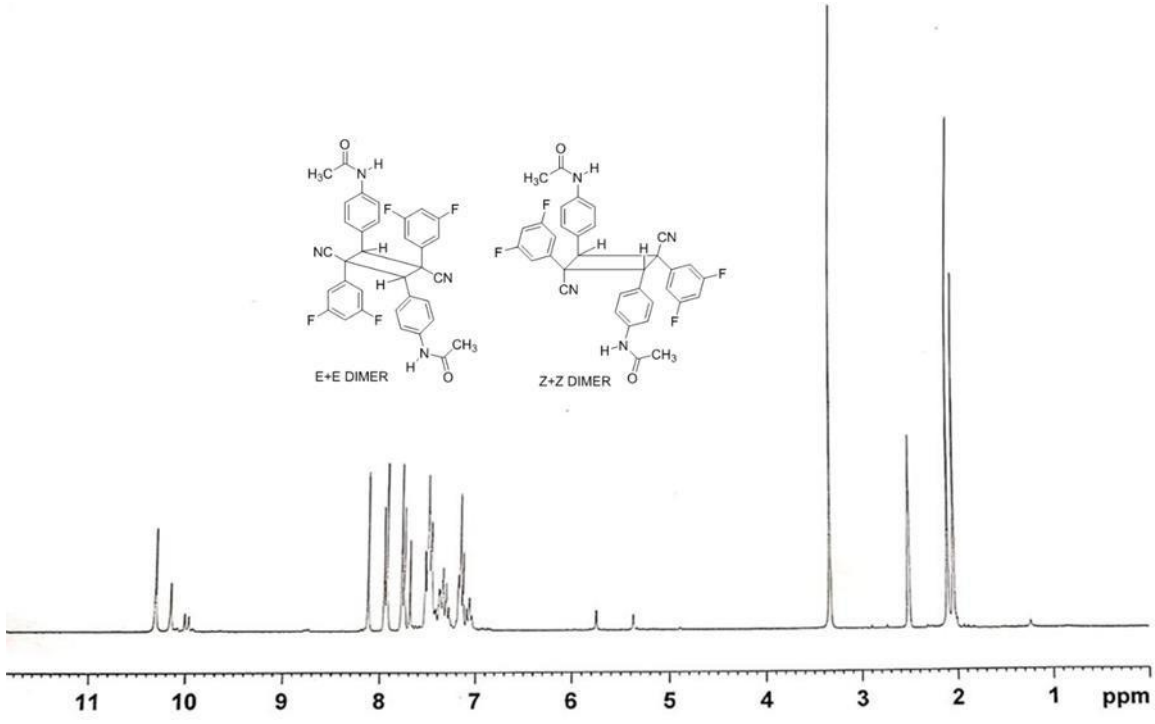

Figure 11. ^{1}H NMR spectra of ***E*-ArF$_2$** after Irradiation in DMSO-d_6 solvent. ***E*-ArF$_2$, *Z*-ArF$_2$** & **ArF$_2$-dimer** all are present in the NMR- mixture.

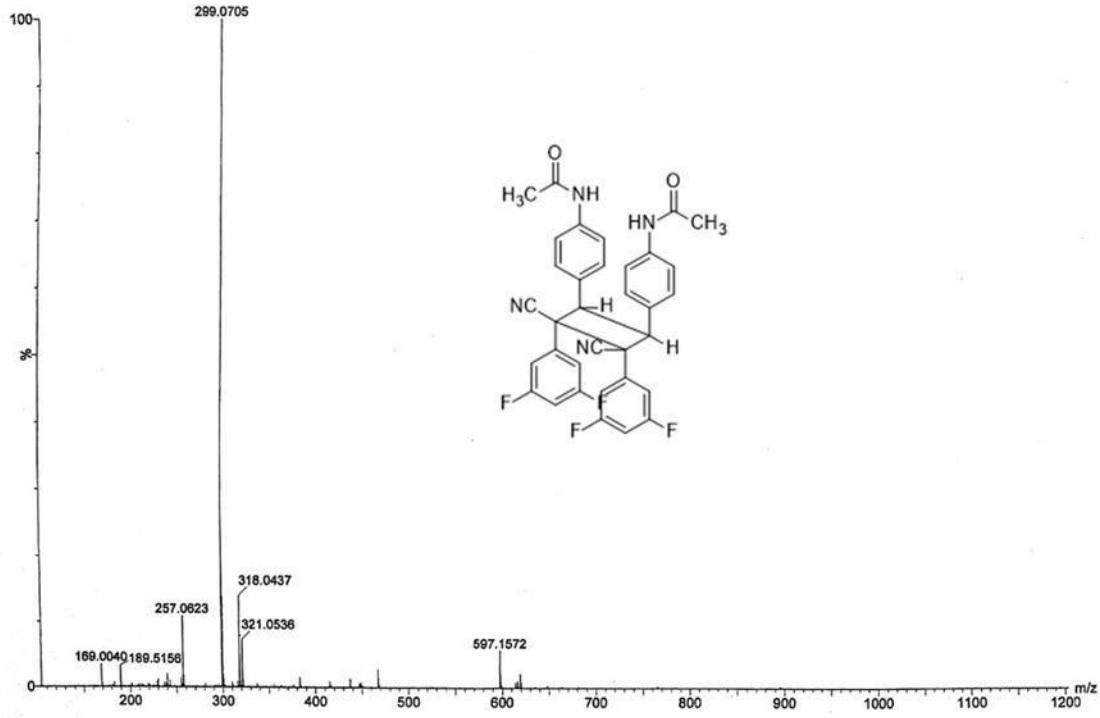

Figure 12. High-resolution mass spectra (HRMS) of compound ***E*-ArF$_2$** after Irradiation showing dimer of ***E*-ArF$_2$** showing [2M+1] at 597.157 where M is the mass of monomer of **ArF$_2$**.

This photochemical reaction is slightly different in the solid state. To observe this, ***E*-ArF$_2$** crystals were irradiated with UV light (390 nm, 5 mW cm^{-2}) for 5 minutes, and subsequently dissolved in DMSO-d_6 and ^{1}H NMR spectra were recorded. As observed in the ^{1}H NMR spectra a mixture of the photo-isomerized product (major) and photo dimerized (minor) products was obtained (Figure 11). Two different proton peaks in the region of 5–6 ppm could be attributed to two different cyclobutane rings which indicates the possibility of the [2 + 2] cycloaddition reaction occurring in both the *E*- and photo converted *Z*-isomer. Mass spectra of the same solution showed a distinct peak at m/z 597.157 that corresponds to the [2 + 2] cycloaddition product and corroborates with the above observation (Figure 12). Thus, crystal actuation under UV light is presumably due to the combined effect of geometric isomerization and the [2 + 2] cycloaddition reaction in the solid-state.

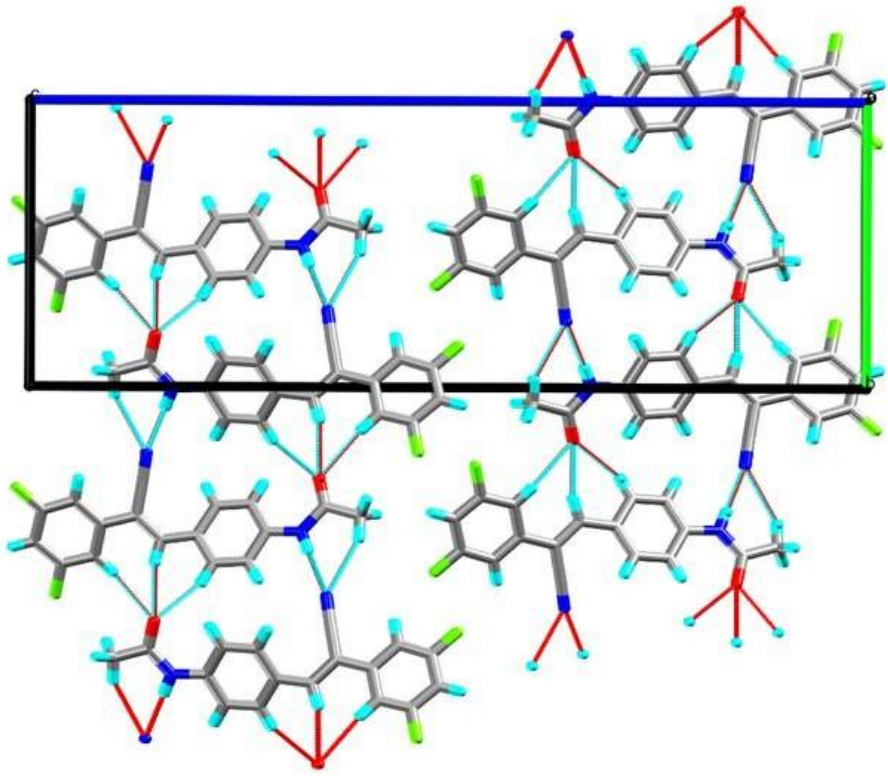

Figure 13. Molecular packing of ***E*-ArF$_2$** Crystal viewed along *a*-axis.

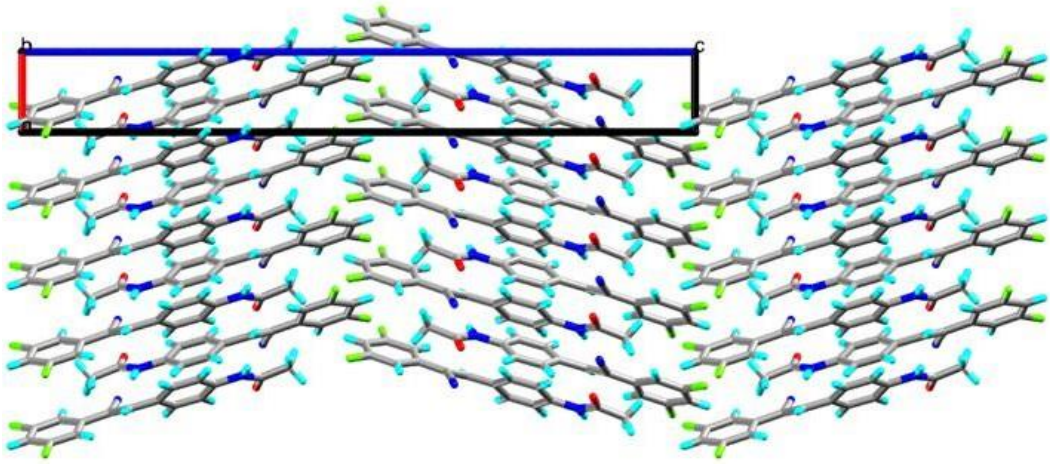

Figure 14. Molecular packing of ***E*-ArF$_2$** crystal viewed along *b*-axis.

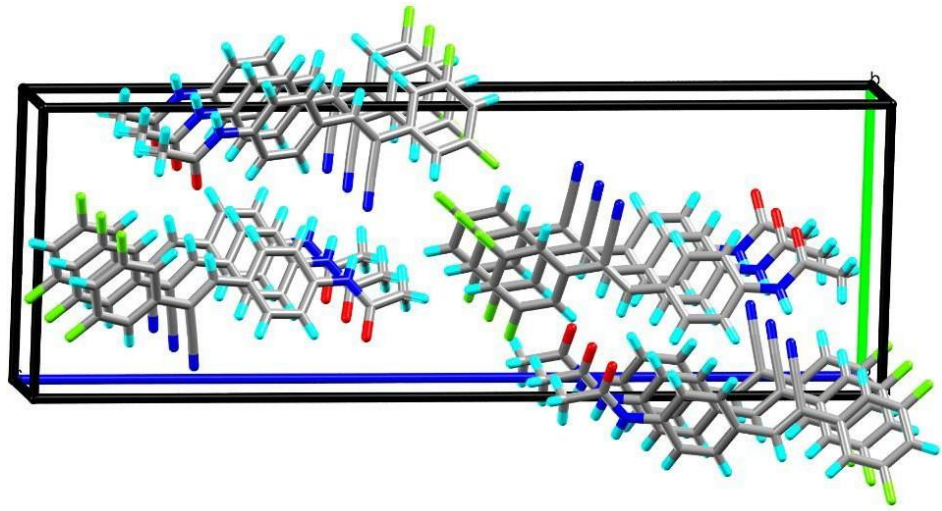

Figure 15. Molecular packing of ***E*-ArF$_2$** crystal along *c*-axis.

UV-vis spectra of ***E*-ArF$_2$** in DMF solution (1×10^{-5} M) exhibit two distinct absorption bands at 353 nm (λ_{max}) and 234 nm which when irradiated with UV light (390 nm) shifted to 343 nm and 244 nm, respectively (Figure 12). Accordingly, solid-state absorption bands of ***E*-ArF$_2$** also shifted from 339 nm and 244 nm to 329 and 253 nm, respectively, upon irradiation. The solid-state fluorescence maxima (λ_{max}) of the crystal change from 503 nm to 517 nm after irradiation. This change is attributed to the photoinduced *E*- to *Z*-isomerization in the solid crystal of ***E*-ArF$_2$**.

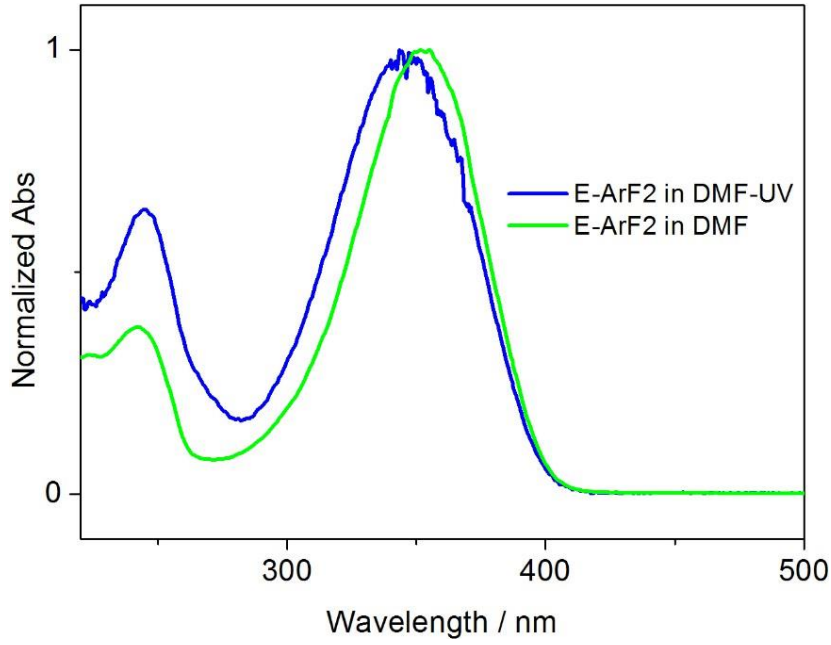

Figure 16. Absorption spectra of ***E*-ArF$_2$** in DMF solution before and after UV irradiation.

2.3.3 PXRD and IR Analysis: Insights into Photomechanical actuation:

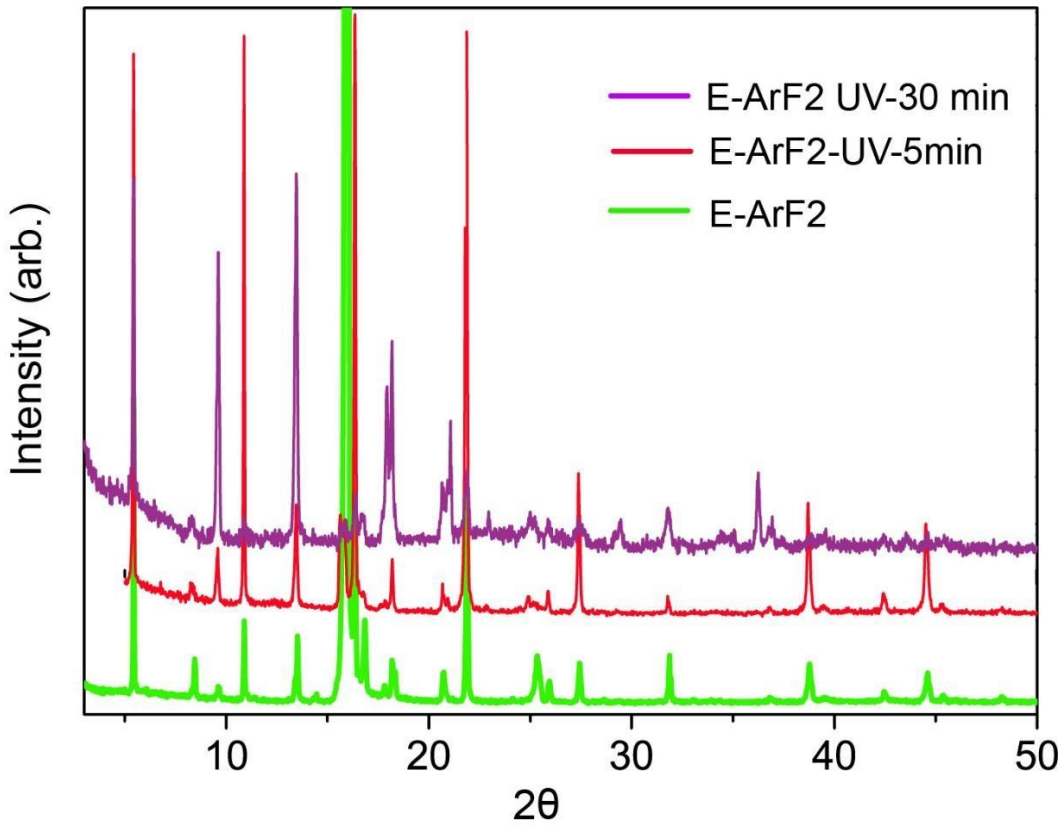

Figure 17. PXRD of ***E*-ArF$_2$** before and after UV irradiation, and (d) IR spectra of ***E*-ArF$_2$** before and after UV irradiation.

To see the change in supramolecular packing during photomechanical actuation, PXRD of ***E*-ArF$_2$** was carried out before and after irradiation the experimental PXRD pattern of ***E*-ArF$_2$** matches well with the simulated pattern (obtained from single crystal X-ray diffraction data using Mercury software). The peak intensity of ***E*-ARF$_2$** gradually decreases with increasing the time of UV irradiation (Figure 13) suggesting the loss of the degree of crystallinity that could be associated with the [2 + 2] cycloaddition product formed by longer UV irradiation.

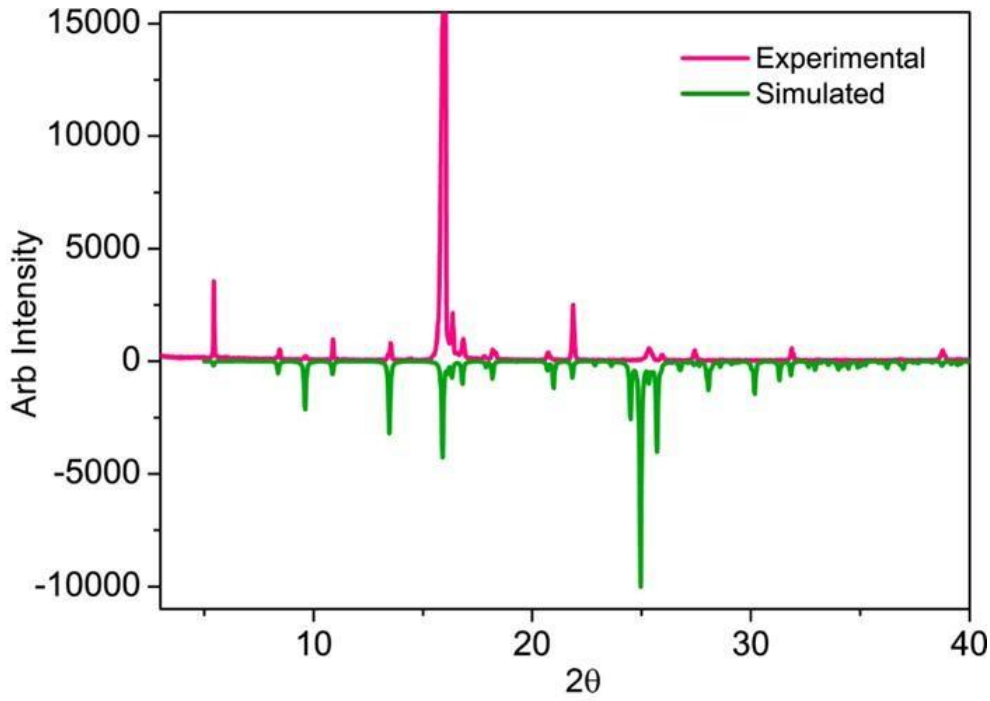

Figure 18. Overlap plot of experimental and simulated PXRD pattern.

In order to obtain the change in bond strength and associated non-covalent intermolecular interactions during photoisomerization, infrared spectra were recorded before and after UV irradiation. As observed from Figure 14, the stretching frequencies of both C=O (amide-1) and N–H in plane bending (amide-II) shifted from 1689 cm^{-1} and 1539 cm^{-1} to 1638 cm^{-1} and 1517 cm^{-1}, respectively, after UV irradiation. A notable change in peak shape was also observed. This suggests a significant change in symmetry of the molecule and the mode of non-covalent interactions associated with these bonds. In contrast to the red shift of the amide-I and amide-II frequency, the C=C stretching frequency showed a blue shift from 1593 cm^{-1} to 1597 cm^{-1} upon UV irradiation. A significant shift in the aromatic C–H bending frequencies at 1338, 1322 and 1122 cm^{-1} was observed upon UV illumination suggesting the reconfiguration of H-bonding interaction involving the (Ar)C– H bond during the photoreaction process.

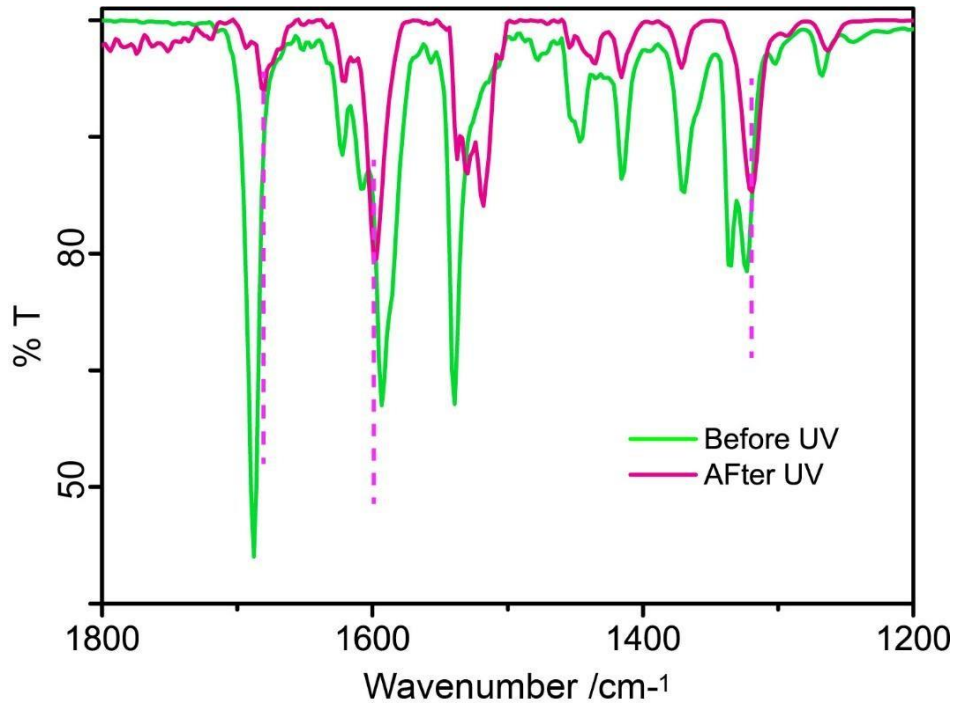

Figure 19. Changes in IR stretching frequency upon UV irradiation

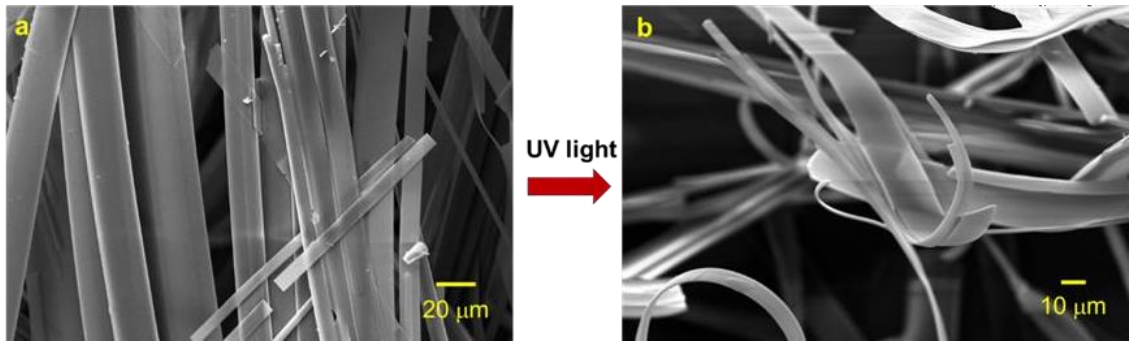

Figure 20. SEM images of ***E*-ArF$_2$**, (a) before UV irradiation, and (b) after UV irradiation.

Table S1. Single crystal X-ray parameters of ***E*-ARF$_2$** at 273 K

CCDC number	2075638
Chemical formula	$C_{17}H_{12}F_2N_2O$
M_r	298.29
Crystal system	Orthorhombic
Space group	$P2_12_12_1$
a / Å	3.8711(3)
b / Å	11.1490(10)
c / Å	32.557(3)
α / ° β / ° γ / °	90 90 90
V / Å^3	1405.1(2)
Zs	4
ρ_{calc} / (g cm^{-3})	1.410
μ / mm^{-1}	0.108
$F000$	616
θ_{min} / °	2.50
θ_{max} / °	26.94
Reflections collected	48393
Independent reflections	9997
GoF	1.196
Final R indices [$I > 2\sigma(I)$]	R_1 = 0.0396, wR_2 = 0.1265
R indices (all data)	R_2 = 0.0487, wR_2 = 0.1410

To obtain an overall picture of the photomechanical motion of the ***E*-ArF$_2$** crystal we have developed a plausible mechanistic model which is shown in Figure 15. The initial macroscopic motion of the ***E*-ArF$_2$** crystal is due to the collective evolution of molecular motion initiated by light triggered *E*- to *Z*-isomerization and the [2 + 2] cycloaddition reaction in the solid matrix. The differential packing arrangements (*E*-reactant and *Z*-product) create an interfacial bimorphic strain within the crystal and are responsible for shape deformation. The packing diagram reveals that the ***E*-ArF$_2$** molecules are longitudinally aligned along the width of the crystal (‖ c-axis). When UV light is shone on the (001) face, the molecules on the surface undergo *E*- to *Z*-isomerization which causes a significant decrease in effective molecular length along the width of the crystal (‖c-axis) and a slight increase in effective molecular length along the longitudinal axis of the crystal (‖a-axis). These two effects (in the illuminated face where the cis-photoproduct concentration is higher) on the molecular scale collectively amplify to the macroscopic scale and causes the shortening of the crystal width and the elongation of the crystal length on the illuminated side (001) and as a result it bends away from the light source. The same mechanism happens when light is shone on the opposite face and the bending occurs in the opposite direction with respect to the illumination direction. The π–π stacking interactions of the phenyl rings along the length of the crystal (‖a-axis) retain the crystal integrity during bending, however after repeated and prolonged UV illumination the [2 + 2] cycloaddition reaction occurs which destroys the π–π stacking interaction and as a result the crystal integrity deteriorates and the long range molecular order is diminished. As observed from PXRD (Figure 13), the long-range order of the molecules also diminished due to the formation of a mixture of photoproducts (geometric isomers, cycloaddition products, etc.) upon prolonged irradiation which could be the possible reason why the crystal stops actuation after a few cycles.

2.4 Schematic representation of photomechanical actuation:

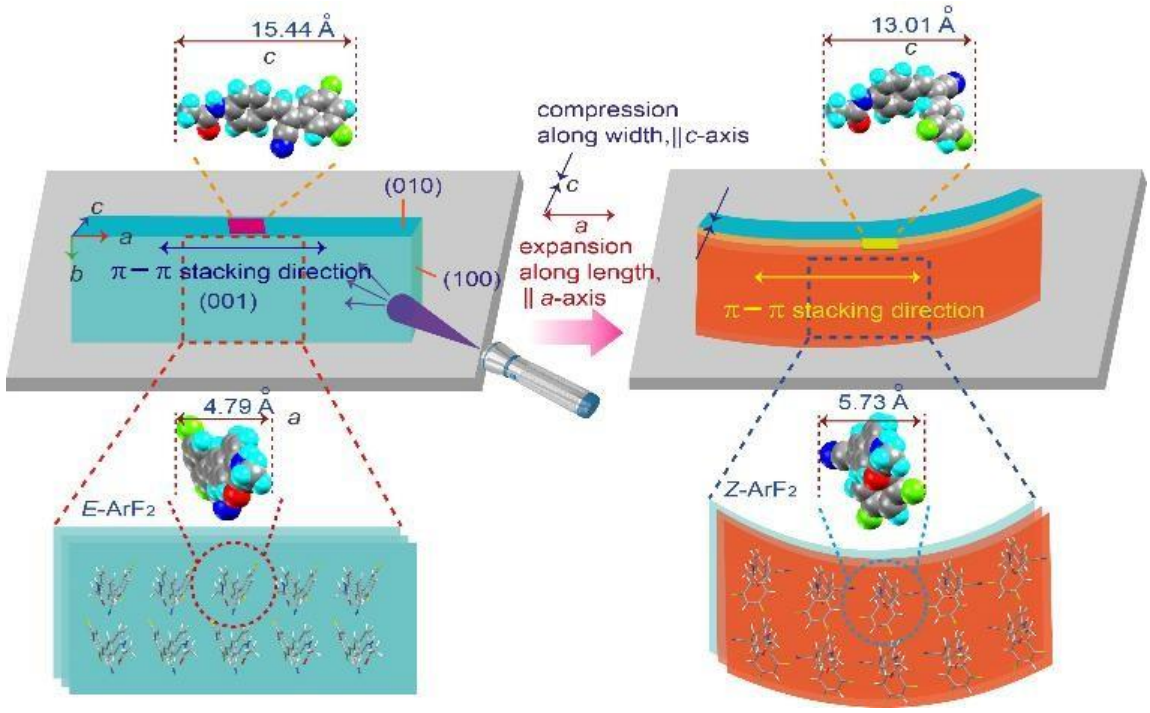

Figure 21. Mechanistic model of ***E*-ArF$_2$** actuation by UV illumination. The orientation of ***E*-ArF$_2$** (viewed along the c-axis) was taken from the crystal structure and the arrangement of molecules is shown for representative purposes.

To obtain an overall picture of the photomechanical motion of the ***E*-ArF$_2$** crystal we have developed a plausible mechanistic model which is shown in Figure 21. The initial macroscopic motion of the ***E*-ArF$_2$** crystal is due to the collective evolution of molecular motion initiated by light triggered *E*- to *Z*-isomerization and the [2 + 2] cycloaddition reaction in the solid matrix. The differential packing arrangements (*E*-reactant and *Z*-product) create an interfacial bimorphic strain within the crystal and are responsible for shape deformation. The packing diagram shown in Figure 15 reveals that the ***E*-ArF$_2$** molecules are longitudinally aligned along the width of the crystal (‖c-axis). When UV light is shone on the (001) face, the molecules on the surface undergo *E*- to *Z*-isomerization which causes a significant decrease in effective molecular length along the width of the crystal (‖c-axis) and a slight increase in effective molecular length along the longitudinal axis of the crystal (‖a-axis). These two effects (in the illuminated face where the cis-photoproduct concentration is higher) on the molecular scale collectively amplify to the macroscopic scale and causes the shortening of the crystal width and the elongation of the crystal length on the illuminated side (001) and as a result it bends

away from the light source. The same mechanism happens when light is shone on the opposite face and the bending occurs in the opposite direction with respect to the illumination direction. The π–π stacking interactions of the phenyl rings along the length of the crystal (||a-axis) retain the crystal integrity during bending, however after repeated and prolonged UV illumination the [2 + 2] cycloaddition reaction occurs which destroys the π–π stacking interaction and as a result the crystal integrity deteriorates and the long range molecular order is diminished. As observed from PXRD (Figure 17), the long range order of the molecules also diminished due to the formation of a mixture of photoproducts (geometric isomers, cycloaddition products, etc.) upon prolonged irradiation which could be the possible reason why the crystal stops actuation after a few cycles.

2.5 Conclusion

We have demonstrated a light-fueled macroscopic actuator that displays various types of shape deformation that can be controlled remotely in an on demand fashion using UV light. More importantly, our light-powered actuator has the capability to optically reconfigure to reverse the direction of the movement when the irradiation direction is reversed. With the aid of NMR, IR and X-ray diffraction studies, we have developed a mechanistic model that might be applicable to other molecular systems that show similar photo-actuation behaviour. In addition to optomechanical behaviour, the same crystal emits green fluorescence. Examples of such dual responsive materials (optical and mechanical response) under a single stimulus (light) are extremely rare. These smart materials have immense potential to be utilized in various technological tools in artificial limbs, medicinal equipment, and soft robotics applications.

References:

[1]. P. Naumov, D. P. Karothu, E. Ahmed, L. Catalano, P. Commins, J. M. Halabi, M. B. Al-Handawi and L. Li, *J. Am. Chem. Soc*., 2020, **142**, 13256–13272.

[2]. L. Zhang, H. Liang, J. Jacob and P. Naumov, *Nat. Commun*., 2015, **6**, 7429, DOI: 10.1038/ncomms8429.

[3]. S. C. Sahoo, N. K. Nath, L. Zhang, M. H. Semreen, T. H. Al- Tel and P. Naumov, *RSC Adv.*, 2014, **4**, 7640–7647.

[4]. D. P. Karothu, J. L. Weston, I. T. Desta and P. Naumov, *J. Am. Chem. Soc*., 2016, **138**, 13298–13306.

[5]. M. K. Panda, R. Centore, M. Causà, A. Tuzi, F. Borbone and P. Naumov, *Sci. Rep*., 2016, **6**, 29610, DOI: 10.1038/srep29610.

[6]. G. Liu, J. Liu, Y. Liu and X. Tao, *J. Am. Chem. Soc*., 2014, **136**, 590–593.

[7]. M. Singh, S. Bhandary, R. Bhowal and D. Chopra, *CrystEngComm*, 2018, **20**, 2253–2257.

[8]. R. Samanta, S. Ghosh, R. Devarapalli and C. M. Reddy, *Chem. Mater*., 2018, **30**, 577–581.

[9]. R. Medishetty, A. Husain, Z. Bai, T. Runčevski, R. E. Dinnebier, P. Naumov and J. J. Vittal, *Angew. Chem., Int. Ed*., 2014, **53**, 1–6.

[10]. S. Ghosh, M. K. Mishra, S. Ganguly and G. R. Desiraju, *J. Am. Chem. Soc*., 2015, **137**, 9912–9921.

[11]. B. B. Rath and J. J. Vittal, *J. Am. Chem. Soc*., 2020, **142**, 20117–20123.

[12]. B. B. Rath, G. Gallo, R. E. Dinnebier and J. J. Vittal, *J. Am. Chem. Soc*., 2021, **143**, 2088–2096.

[13]. A. Takanabe, M. Tanaka, K. Johmoto, H. Uekusa, T. Mori, H. Koshima and T. Asahi, *J. Am. Chem. Soc*., 2016, **138**, 15066–15077.

[14]. N. K. Nath, T. Runčevski, C.-Y. Lai, M. Chiesa, R. E. Dinnebier and P. Naumov, *J. Am. Chem. Soc*., 2015, **137**, 13866–13875.

[15]. S. Li and D. Yan, *ACS Appl. Mater. Interfaces*, 2018, **10**, 22703–22710.

[16]. S. Kobatake, S. Takami, H. Muto, T. Ishikawa and M. Irie, *Nature*, 2007, **446**, 778–781.

[17]. M. Morimoto and M. Irie, *J. Am. Chem. Soc*., 2010, **132**, 14172–14178.

[18]. F. Terao, M. Morimoto and M. Irie, *Angew. Chem., Int. Ed*., 2012, **51**, 901–904.

[19]. P. Naumov, S. Chizhik, M. K. Panda, N. K. Nath and E. Boldyreva, *Chem. Rev*., 2015, **115**, 12440–12490.

[20]. T. Kim, L. Zhu, R. O. Al-Kaysi and C. J. Bardeen, *ChemPhysChem*, 2014, **15**, 400–414.

[21]. J. M. Halabi, E. Ahmed, S. Sofela and P. Naumov, *Proc. Natl. Acad. Sci. U. S. A.*, 2021, **118**, e2020604118, DOI: 10.1073/ pnas.2020604118.

[22]. L. Gao, Y. Hao, X. Zhang, X. Huang, T. Wang and H. Hao, *CrystEngComm*, 2020, **22**, 3279–3286.

[23]. O. S. Bushuyev, T. A. Singleton and C. J. Barrett, *Adv. Mater.*, 2013, **25**, 1796–1800.

[24]. Y. Ye, L. Gao, H. Hao, Q. Yin and C. Xie, *CrystEngComm*, 2020, **22**, 8045–8053.

[25]. H. Koshima and N. Ojima, *Dyes Pigm*., 2012, **92**, 798–801.

[26]. F. Tonga, M. Al-Haidar, L. Zhu, R. O. Al-Kaysi and C. J. Bardeen, *Chem. Commun*., 2019, **55**, 3709–3712.

[27]. H. Koshima, H. Uchimoto, T. Taniguchi, J. Nakamura, T. Asahi and T. Asahi, *CrystEngComm.*, 2016, **18**, 7305–7310.

[28]. T. Kim, L. Zhu, L. J. Mueller and C. J. Bardeen, *J. Am. Chem. Soc*., 2014, **136**, 6617–6625.

[29]. H. Koshima, R. Matsuo, M. Matsudomi, Y. Uemura and M. Shiro, *Cryst. Growth Des*., 2013, **13**, 4330–4337.

[30]. H. Koshima, K. Takechi, H. Uchimoto, M. Shiro and D. Hashizume, *Chem. Commun*., 2011, **47**, 11423–11425.

[31]. R. Mandal, A. Garai, S. Peli, P. K. Datta and K. Biradha, *Chem. – Eur. J*., 2020, **26**, 396–400.

[32]. Y. Shu, K. Ye, Y. Yue, J. Sun, H. Wang, J. Zhong, X. Yang, H. Gao and R. Lu, *CrystEngComm*., 2021, DOI: 10.1039/D1CE00086A.

[33]. J. Peng, K. Ye, C. Liu, J. Sun and R. Lu, *J. Mater. Chem. C*, 2019, **7**, 5433–5441.

[34]. J. K. Sun, W. Li, C. Chen, C.-X. Ren, D.-M. Pan and J. Zhang, *Angew. Chem., Int. Ed*., 2013, **52**, 1–6.

[35]. H. Wang, P. Chen, Z. Wu, J. Zhao, J. Sun and R. Lu, *Angew. Chem*., 2017, **129**, 9591–9595.

[36]. F. Tong, W. Xu, T. Guo, B. F. Lui, R. C. Hayward, P. Palffy- Muhoray, R. O. Al-Kaysi and C. J. Bardeen, *J. Mater. Chem. C*, 2020, **8**, 5036–5044.

[37]. D. Kitagawa and S. Kobatake, *Chem. Commun.*, 2015, **51**, 4421–4424.

[38]. D. Kitagawa, K. Kawasaki, R. Tanaka and S. Kobatake, *Chem. Mater*., 2017, **29**, 7524–7532.

[39]. A. Ryabchun, Q. Li, F. Lancia, I. Aprahamian and N. Katsonis, *J. Am. Chem. Soc*., 2019, **141**, 1196–1200.

[40]. P. Gupta, T. Panda, S. Allu, S. Borah, A. Baishya, A. Gunnam, A. Nangia, P. Naumov and N. K. Nath, *Cryst. Growth Des*., 2019, **19**, 3039–3044.

[41]. P. Li, J. Wang, P. Li, L. Lai and M. Yin, Mater. *Chem. Front*., 2021, **5**, 1355–1363.

[42]. L. Zhu, F. Tong, N. Zaghloul, O. Baz, C. J. Bardeen and R. O. Al-Kaysi, *J. Mater. Chem. C*, 2016, **4**, 8245–8252.

[43]. F. Tong, D. Kitagawa, I. Bushnak, R. O. Al-Kaysi and C. J. Bardeen, *Angew. Chem., Int. Ed*., 2021, **60**, 2414–2423.

[44]. Z. Wu, S. Mo, L. Tan, B. Fang, Z. Su, Y. Zhang and M. Yin, *Small*, 2018, **14**, 1802524.

[45]. X. Luo, J. Li, C. Li, L. Heng, Y. O. Dong, Z. Liu, Z. Bo and B. Z. Tang, *Adv. Mater*., 2011, **23**, 3261–3265.

[46]. G. M. J. Schmidt, *Pure Appl. Chem*., 1971, **27**, 647–678.

[47]. K. Biradha and R. Santra, *Chem. Soc. Rev.*, 2013, **42**, 950–967.

CHAPTER-3

Photo-Fueled Puffing, Shape Change and Movement of Solvatomorphic Crystals Induced by Topochemical [4+4] Cycloaddition Reaction

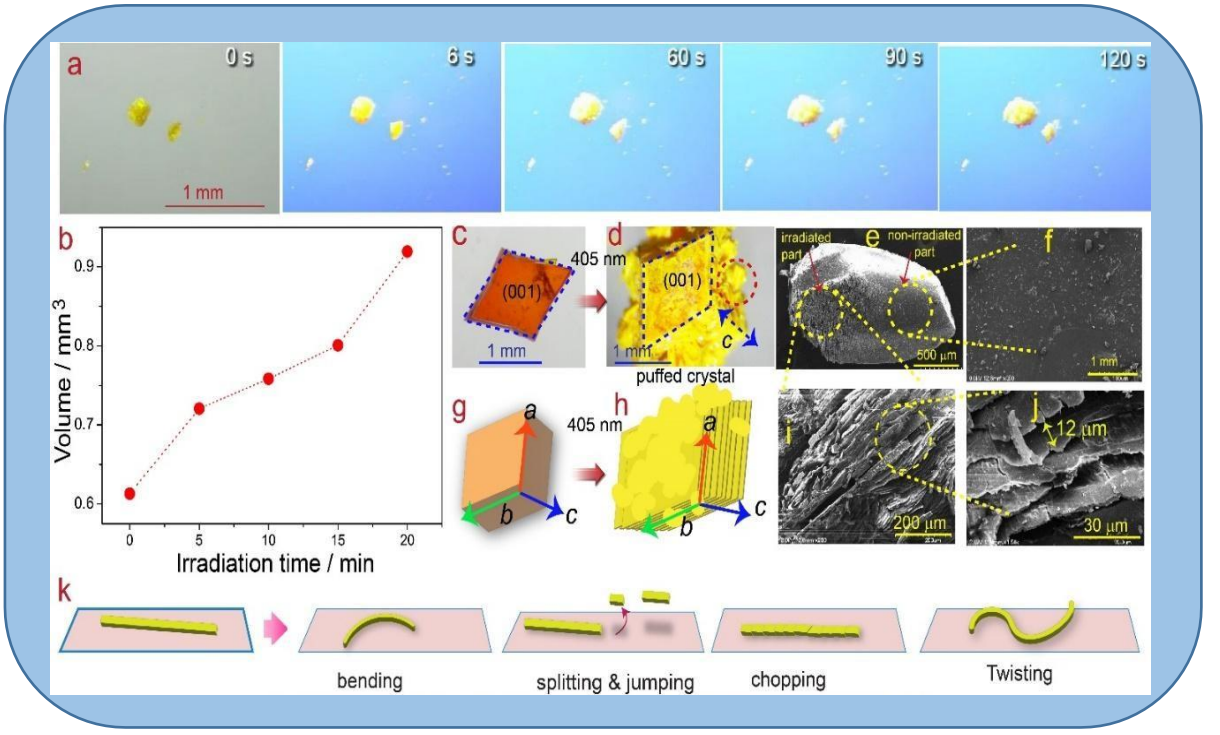

3.1. Introduction

One of our goals of this project was to design and synthesize molecules that are expected to have light-responsive actuation property. Although many azobenzene based molecules have already been reported in literature, the necessity of developing new molecules having novel physical property seems to be a never-ending effort. Compared to azobenzene-based actuators, acylhydrazones based molecules are comparatively new and thus have a better scope to be explored to a greater extent. Moreover, by changing the functional group and substituent group in the molecule, we can attain a diverse range of molecules that could have tunable optical as well as actuation property. In this report, we have described our recent research work on acylhydrazone based schiff base derivative-based molecule, the crystal of which exhibited light fuelled movement in bulk scale. Our rationale behind designing the molecule is to keep the photoactive functional group (C=N and cycloaddition) in the core with an auxiliary functional group (F/Cl,OH etc) or substituents that can engage in non-covalent interaction for facile supramolecular reconfiguration during photo isomerization. In this work, we report the first example of two crystal solvates of an anthracene-benzhydrazide based molecule (**Ant**) that display very distinct photo-responsive behaviour when 365 or 405 nm or visible light is illuminated. For the first time, the crystal hydrate that has water molecule in the lattice (hereafter named as **Ant-H_2O**) display fascinating puffing behaviour with large volume expansion upto 50 % accompanied with surface modulation when illuminated with 405 nm light, a phenomenon very much similar to the rice or popcorn puffing by thermal treatment. The other crystal solvate having DMF in the crystal lattice (hereafter named as **Ant-DMF**) responds to 405 nm light by bending, twisting, chopping, jumping or splitting etc. The chopping of **Ant-DMF** crystal was also observed under ambient / white light but at a slower rate compared to 405 nm light.

Nature provides a numerous example of light-powered organism that can change their shape, size or surface pattern autonomously in presence of light having different wavelength or intensity.[1-3] Such motions are often multi-stimuli responsive where both light intensity and aerial humidity play key role for the actuation of the plant body. However, mimicking such functions in the laboratory using soft molecular materials such as crystals, polymers etc poses a challenging task and demands huge imagination, design skills, and experimental efforts from the involved researchers.

"Dynamic single crystals",[4] an emerging class of smart materials that have special and extraordinary capability to transform external energy directly to macroscopic motion via

cooperative molecular and supramolecular pathway [5-15]. Several numbers of such crystals have recently been reported that can bend or deform,[16-22] hop,[23-24] twist,[25-27] walk and roll[28] when external stimuli such as heat, light, pressure, or humidity gradient is applied. These crystals are classic example of biomimetic materials that have huge potential to be utilized for various technological application such as machinery tools, micro fluidics, flexible optoelectronics, artificial muscles etc.[29-32]

Among the various stimuli, light is the most attractive one in the context that it can be remotely operated and tuneable by changing the wavelength or intensity and offers fine modulation of dynamic properties of the soft materials. Molecules with different photoactive functional groups that can undergo geometric (*trans-cis*) isomerization,[25,28] linkage isomerization,[24] ring opening-closing reaction,[5,35] cycloaddition reaction[14,15] etc have been employed by various researchers for triggering light-induced molecular motion and subsequent amplification to macroscopic actuation with the aid of easily reconfigurable non-covalent interactions. Along this interest, the Schmidt's topochemical [2+2] or [4+4] cycloaddition reactions have attracted great interest to realize photo-fueled bulk actuation of the single crystals. Numerous numbers of organic molecules with anthracene,[33-35] styryl pyridyl,[36-38] styrylbenzoxazole,[39] cyanovinyl moiety, [40-41] organoboron compounds, [42] have been reported to exhibit photomechanical motion of the crystals based on [2+2] or [4+4] cycloaddition reaction. In most of the above reports the macroscopic property of the crystal was tuned by using different substituents on the skeleton. On the contrary, such tuning can also be realized by employing polymorphs or solvatomorphs that are structurally different. However, the examples of polymorphic or solvatomorphic structures that display distinct photoresponsive behaviours as a result of [2+2] or [4+4] cycloaddition reactions is extremely rare.

In this chapter, we report the first example of two crystal solvates of an anthracene-benzhydrazide based molecule (**Ant**) that display very distinct photo-responsive behaviour when UV or visible light is illuminated on the crystals. Very interestingly, one of the crystal solvates namely **Ant-H_2O** exhibits photoinduced (405 nm) crystal puffing with large volume expansion (upto 50 %) and remarkable change in surface morphology as a result of the topochemical [4+4] cycloaddition reaction. In some cases, jumping (photosalient effect), small displacement was also observed during the photoreaction. Although there are several reports of photoinduced popping crystal, popularly known as "photosalient crystal",[24, 43] but to our knowledge, this is the first example of an organic crystal solvate that display photoinduced puffing behaviour with large volume expansion and enhanced surface porosity, a phenomenon that resembles puffed-rice made by the thermal treatment of rice grains (Figure 7). The other

crystal solvate **Ant-DMF** showed various types of photomechanical behaviour such as bending, twisting, slicing/chopping, splitting, and jumping behaviour when 365 nm or 405 nm light is illuminated on it.

3.2 Experimental

3.2.1. Materials & methods:

4-Hydroxybenzohydrazine was purchased from Sigma-Aldrich and used without further purifications. 9-Anthracenecarboxaldehyde was purchased from Sigma-Aldrich and used as commercially received. Glacial acetic acid was purchased from Merck India. It was used as commercially received. Merck ACS grade (Emplura) solvents were used for synthesis and spectroscopy grade solvents were used for crystallization and spectroscopy studies. Several Analytical Techniques Utilized as follows,

NMR Spectroscopy: Both ^{1}H NMR (300 MHz) and ^{13}C NMR spectra were recorded on a Bruker AVANCE 300 spectrometer using $CDCl_3$ or DMSO-d_6 as the solvent. The chemical shifts (δ) are reported in ppm for precision and referenced to the internal standard tetramethylsilane ($Si(CH_3)_4$). .

Scanning Electron Microscopy (SEM): SEM images of the samples were captured using a FEI INSPECT F50 instrument with an operating voltage of 5 kV. The samples were coated with a thin layer of gold to enhance conductivity and image clarity.

High-Resolution Mass Spectrometry (HRMS): The HRMS of compounds **Ant-DMF** & **Ant-H_2O** were acquired using a QTOF Micro YA263 mass spectrometer operated in electrospray ionization (ESI) mode.

UV-Vis and Fluorescence Spectroscopy: UV-Vis absorption spectra were recorded with a Shimadzu UV-2401C spectrophotometer in solution and solid-state configurations. For fluorescence studies in the solid state, a HORIBA Jobin Yvon Fluorolomax-4 spectrofluorometer was employed. Additionally, lifetime measurements were performed on a Modular Time-Correlated Single Photon Counting (TCSPC) system equipped with a Delta Flex detector (PPD850).

Infrared Spectroscopy (IR): IR spectra were recorded using a PerkinElmer LX-1 FT-IR spectrometer to examine functional group characteristics and molecular interactions.

Powder X-ray Diffraction (PXRD): PXRD patterns were obtained using a Bruker D8 Advanced Diffractometer with Cu Kα radiation (λ = 1.5418 Å), operating at 40 kV and 40 mA. The Lynxeye detector was utilized for data acquisition with a scanning rate of 0.2 seconds per step over a 2θ range of 0° to 50°.

Single Crystal X-ray Diffraction

High-quality single-crystal X-ray diffraction data for **Ant-DMF** & **Ant-H_2O** were collected using a Bruker D8 Venture APEX 3 diffractometer equipped with a CCD area detector and MoKα radiation (λ = 0.71069 Å). The SAINT program (version 8.38A) was used for data reduction, and XPREP (within the APEX 3 suite, version 2017.3–0) ensured structural agreement. Absorption corrections were performed with SADABS, and the structures were solved using SHELXT (version 2018/2) and refined with SHELXL-2014. Non-hydrogen atoms were refined anisotropically, while hydrogen atoms were calculated and refined isotropically. Crystallographic data for **Ant-DMF** & **Ant-H_2O** have been deposited at the Cambridge Crystallographic Data Centre (CCDC) under deposition no, 2297556 and 2297557.

3.2.2 Synthesis & Characterization:

Synthesis of Ant: A 100 mL round-bottom flask equipped with a magnetic stirrer and reflux condenser was charged with 9-Anthracenecarboxaldehyde (0.150g, 9.86×10-4mol), 4-Hydroxybenzohydrazine (0.201, 9.745 × 10-4 mol) in 30 mL (MeOH : THF = 25:5) solution. One drop glacial acetic was added to it and the resulting mixture was stirred at 70°C for 3 hours. The product was precipitated from the solution which was filtered and washed with methanol and air dried. ^{1}H NMR (300 MHz, D6-DMSO, 25°C): Ant δ (ppm), 11.909 (s, 1H, NH), 10.191 (s, 1H, OH), 9.648 (s, 1H, Csp2-H), 8.76 (d, 2H,J= 8.7 Hz, ArH) ,8.73 (s, 1H, ArH), 8.184 (d, 2H, J= 8.4 Hz, ArH), 7.93 (d, 2H, J= 8.4 Hz, Ar-H), 7.63 (m, 4H, ArH), 6.93 (d, 2H, J= 8.4 Hz , ArH); 13C NMR (75 MHz, D6-DMSO, 25°C) δ (ppm). 163.25 , 161.31, 146.50, 131.42, 130.23, multiplate, 129.46, 127.56 ,125.79 multiplate,125.42, 124.35, 115.63 HRMS: calculated for C22H16N2O2 is 340.1212 , obtained m/z = 341.0827 (M+H), 363.0614 (M+23).

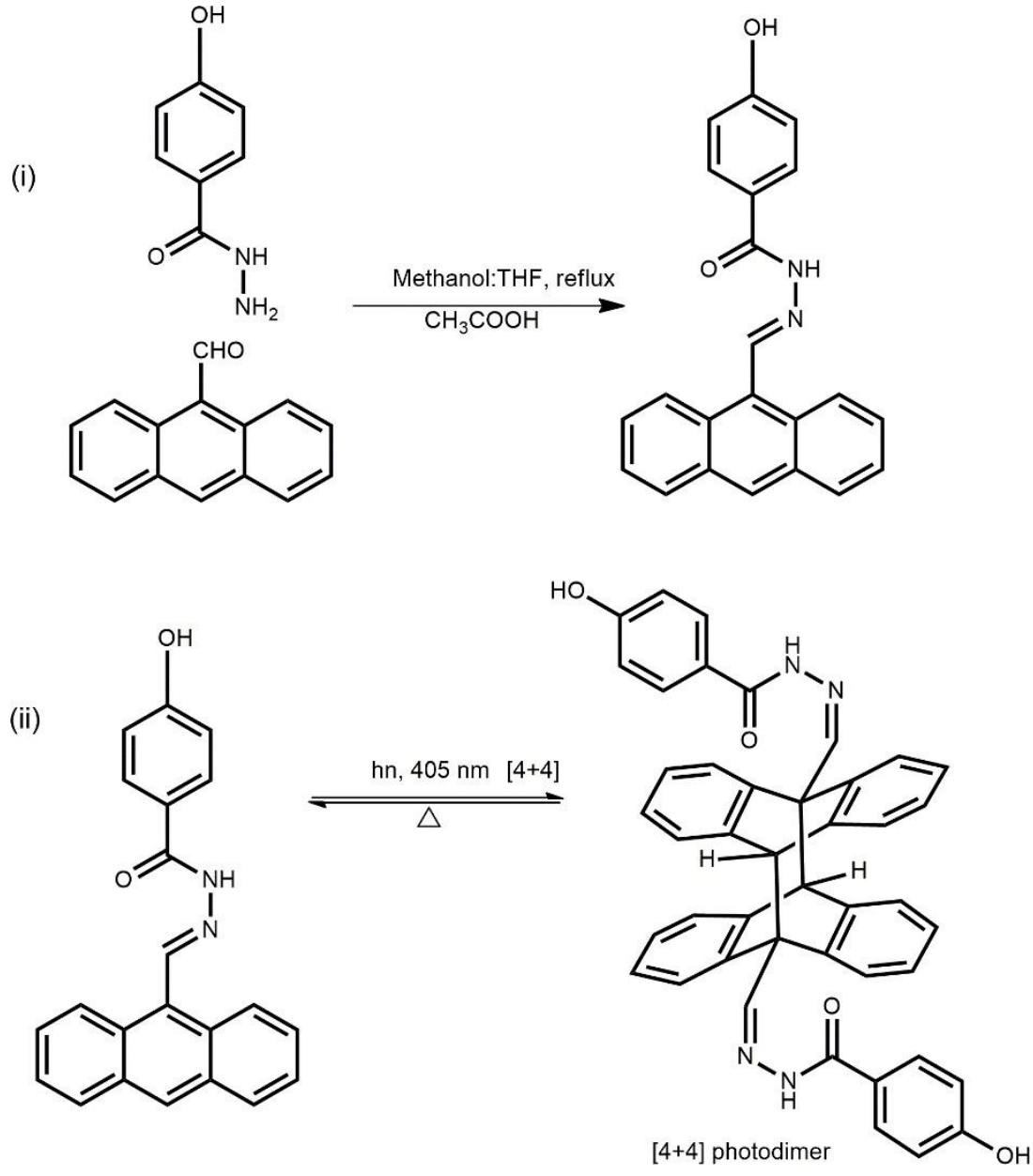

Scheme 1. (i) Synthetic scheme of Ant, (ii) photodimerization reaction under 405 nm light.

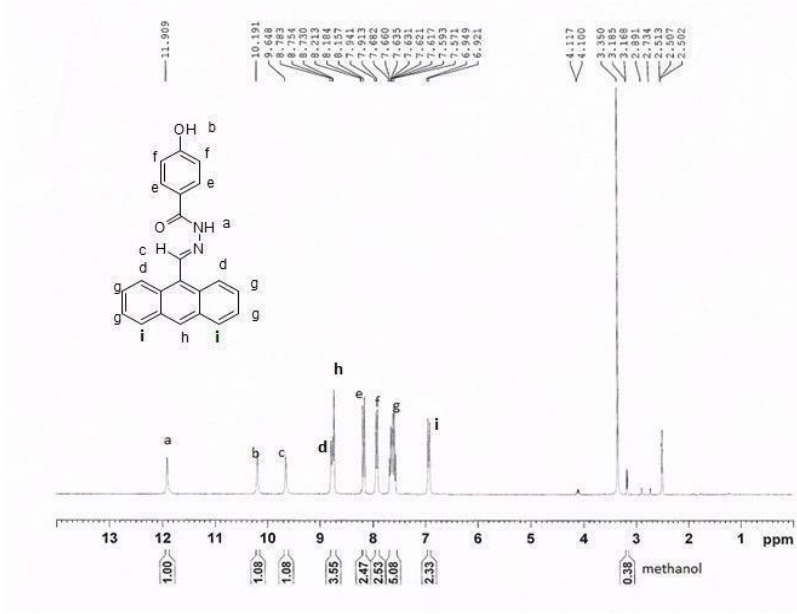

Figure 1. ^{1}H NMR spectra of **Ant** in DMSO d_6

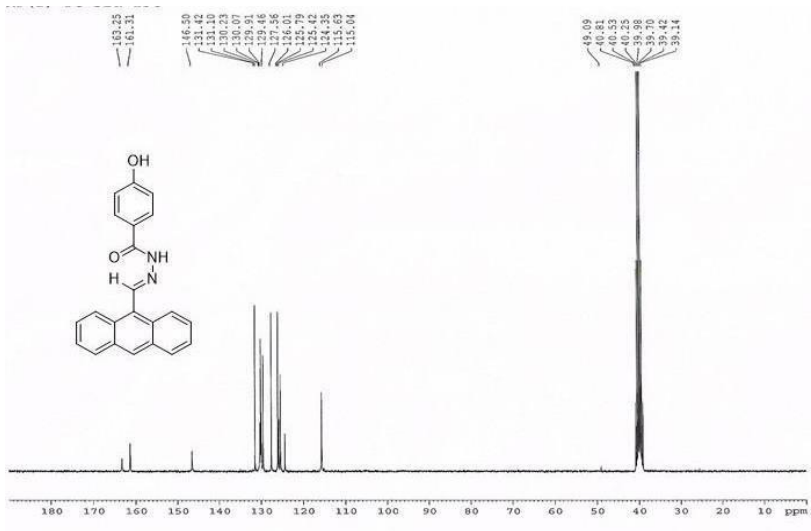

Figure 2. ^{13}C NMR spectra of **Ant** in DMSO d_6

The compound **Ant** contains one hydroxyl proton (–OH), one amine proton (–NH), one Csp^2–H proton, and the remaining protons are aromatic. In the ^{1}H NMR spectrum, the most downfield peak appears at 11.909 ppm and corresponds to the –NH proton. The signal at 10.191 ppm is attributed to the hydroxyl (–OH) proton, while the peak at 9.648 ppm represents the Csp^2–H proton. All other proton signals are observed in the aromatic region, ranging from 8.76 ppm to 6.93 ppm. The chemical shifts and pattern of the recorded ^{1}H NMR spectrum are in excellent agreement with the expected structure of the compound, confirming its identity.

In the ^{13}C NMR spectrum, the amide carbon resonance is observed at 163.25 ppm, which is consistent with the deshielded nature of carbonyl carbons in amide functional groups. All aromatic carbon signals appear in the expected region, between 164 ppm and 115 ppm. These chemical shifts align well with typical aromatic carbon environments. Together with the ^{1}H NMR data—where the chemical shifts and signal patterns perfectly match the proposed structure—the ^{13}C NMR results further confirm the identity and structural integrity of the compound.

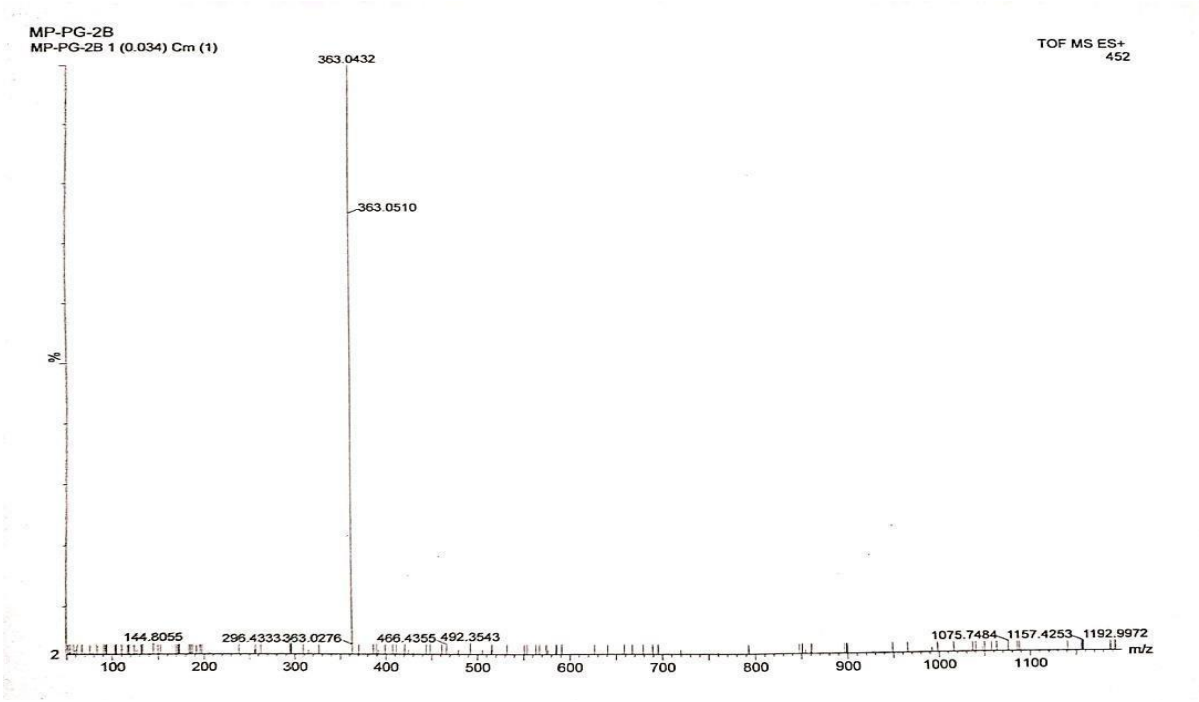

Figure 3. HRMS of **Ant** showing [M+23] peak at m/z = 363.0432.

High-resolution mass spectrometry (HRMS) was performed to confirm the successful synthesis of compound **Ant.** The calculated molecular mass of **Ant** ($C_{22}H_{16}N_2O_2$) is 340.1212 Da. In the HRMS spectrum, a prominent peak was observed at *m/z* 341.0827, corresponding to the protonated molecular ion $(M+H)^+$. Another peak at *m/z* 363.0614 was assigned to the sodium adduct $(M+Na)^+$. These values are in close agreement with the calculated mass, thereby supporting the identity and purity of the synthesized compound.

3.3 Results and Discussions:

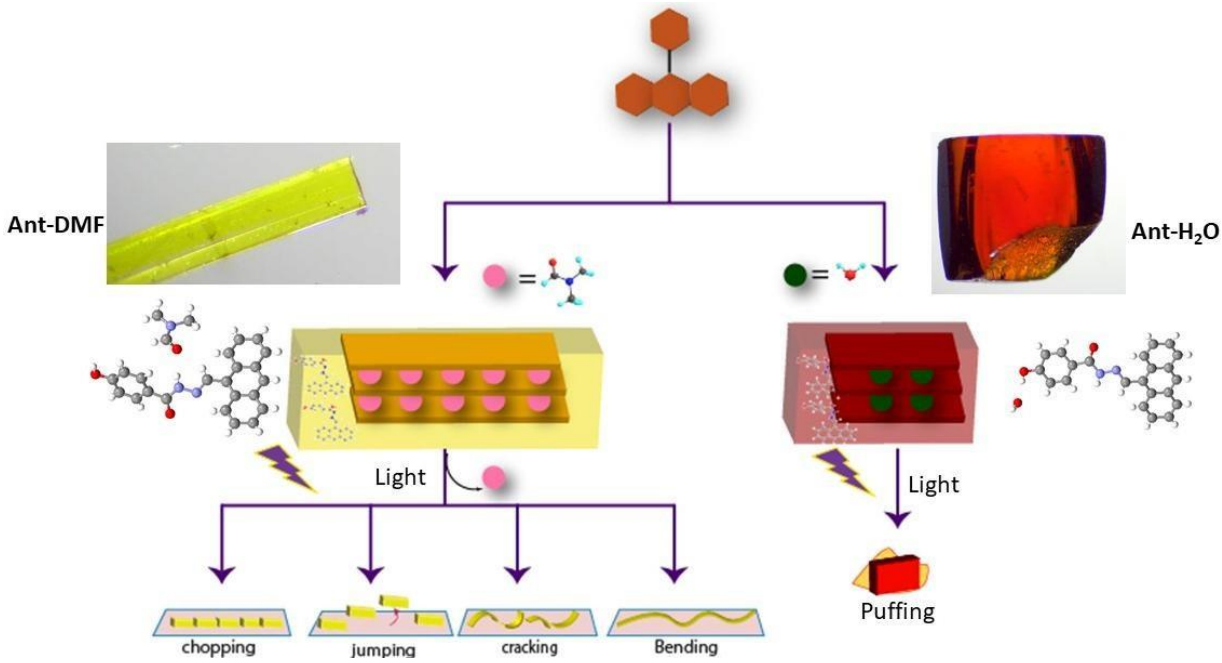

Scheme 2: Schematic representation of photo induced actuation of two different solvatomorphs.

The image above represents the overall theme of this research work. In this study, two distinct solvatomorphs were obtained by crystallizing the same compound using two different solvents. The yellow, plate-like solvatomorph—incorporating *N*,*N*-dimethylformamide (DMF) within its crystal lattice—is referred to as **Ant-DMF**. The red, block-shaped solvatomorph, which includes water (H_2O) in its crystal structure, is designated as **Ant-H_2O**. Both solvatomorphs exhibit unique and remarkable photomechanical actuation when exposed to a laser light source. Specifically, the **Ant-DMF** crystals respond to 405 nm blue laser irradiation by undergoing chopping, jumping, cracking, and bending motions. In contrast, the **Ant-H_2O** crystals display an unusual photomechanical puffing behavior under the same laser conditions.

Notably, this puffing phenomenon observed in **Ant-H_2O** represents a previously unreported mode of photomechanical actuation in molecular crystals, adding novelty and significance to this research.

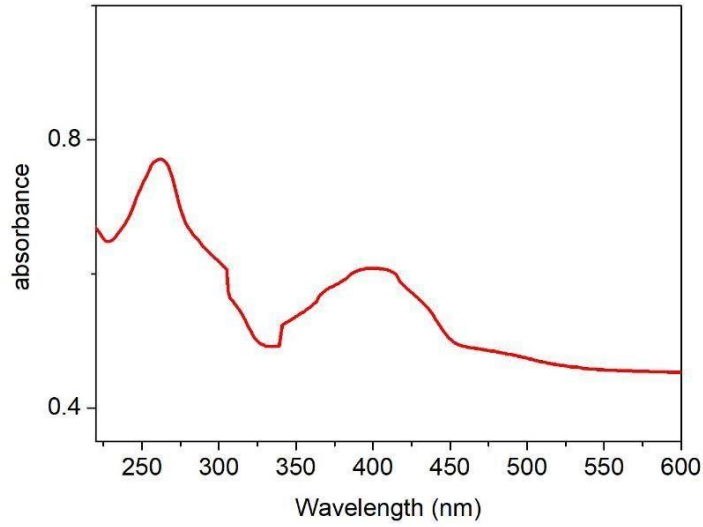

Figure 4. Solid state UV-Vis spectra of pristine **Ant.**

The solid-state absorbance spectrum of pristine **Ant** reveals two distinct absorption bands. The first absorption band, observed at λ_{max} = 261 nm, is attributed to an n→π* electronic transition. The second, broader absorption band appears at λ_{max}= 403 nm, which is associated with intramolecular charge transfer (ICT) within the compound. These spectral features reflect the compound's electronic structure and provide insight into its photophysical behaviour in the solid state.

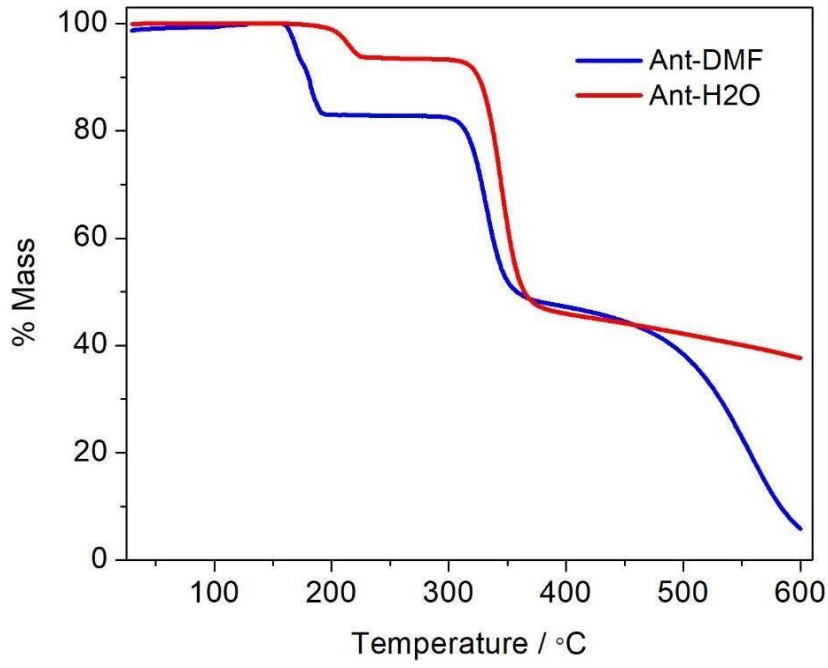

Figure 5. TGA thermogram of **Ant-DMF** and **Ant-H_2O.**

Thermogravimetric analysis (TGA) was carried out to evaluate the thermal stability of the solvatomorphs. The **Ant-DMF** solvatomorph exhibited thermal decomposition starting at

161 °C, whereas **Ant-H_2O** began decomposing at a significantly higher temperature of 196 °C. This indicates that the crystalline water in **Ant-H_2O** is strongly bound, most likely due to extensive intermolecular hydrogen bonding interactions. As a result, **Ant-H_2O** demonstrates superior thermal stability compared to **Ant-DMF**. Overall, these findings suggest that the compound exhibits remarkably high thermal stability in its crystalline forms.

3.3.1 Photo induced puffing property of Ant-H_2O:

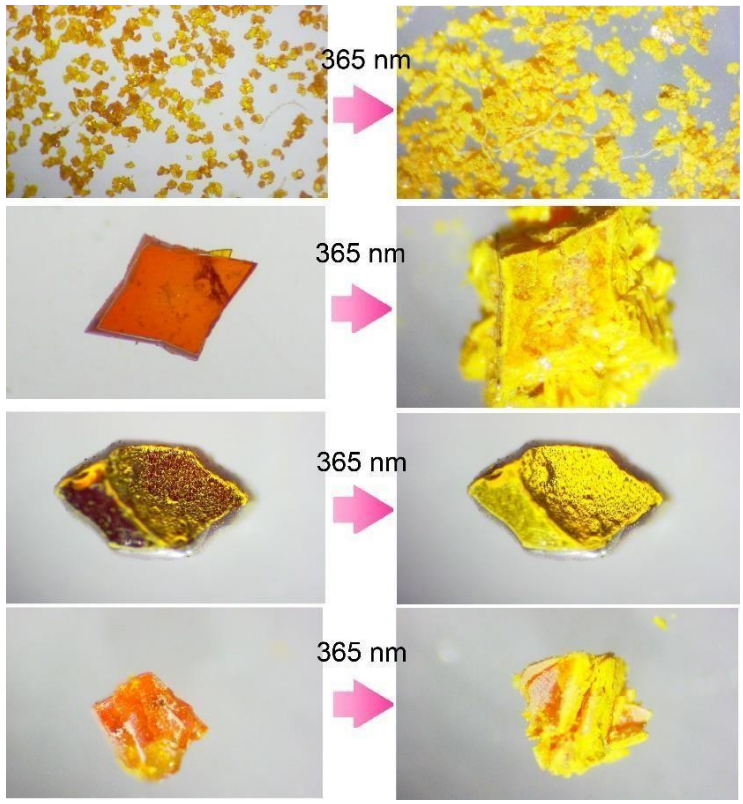

Figure 6. Optical microscope pictures of the **Ant-H_2O** crystals upon UV light illumination

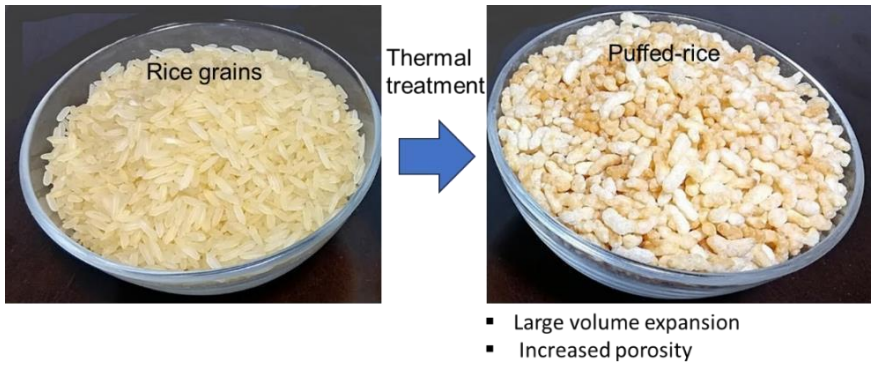

Figure 7. Making of puffed-rice from rice grains by thermal treatment

Interestingly, the photo-induced actuation observed in the **Ant-H_2O** solvatomorph closely resembles the puffing behaviour of rice when heated. Upon exposure to 405 nm laser light, the crystal rapidly expands and undergoes a sudden volumetric change-akin to the puffing of rice grains due to rapid vapour expansion and internal pressure build-up. This analogy provides an intuitive understanding of the rare and dynamic photomechanical puffing behaviour, which to the best of our knowledge, has not been previously reported in molecular crystals.

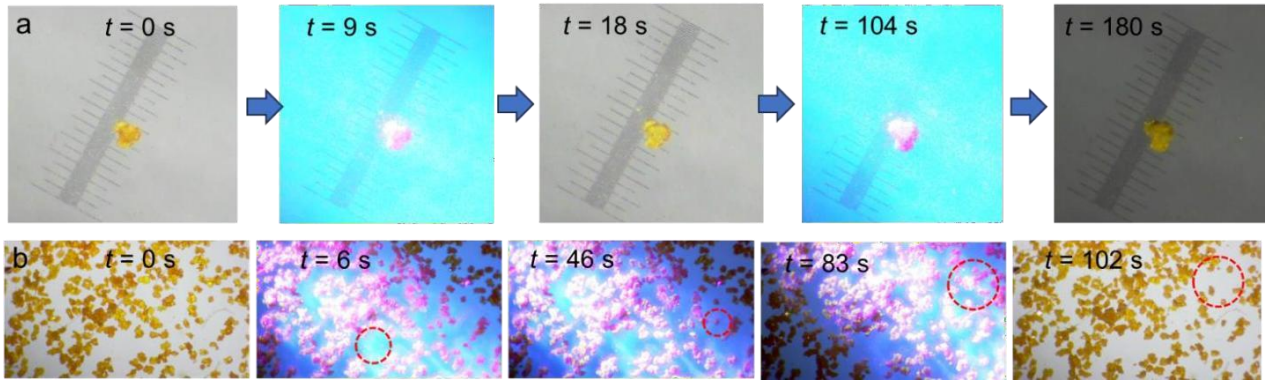

Figure 8. Optical microscope pictures of the **Ant-H_2O** crystals upon UV light illumination. (a) Photoinduced puffing with volume expansion (background scale 1 mm), (b) Gradual snapshots of photosalient effect by few **Ant-H_2O** crystals, displaced crystals are marked by red-dotted circle.

Photo-induced volumetric expansion was observed in **Ant-H_2O** crystals upon irradiation with 395 nm light. Within just 104 seconds of exposure, the crystal volume increased by approximately 50% relative to its initial volume, as clearly illustrated in the accompanying image. This significant expansion highlights the unique photomechanical puffing behaviour of **Ant-H_2O**, distinguishing it from conventional light-responsive materials.

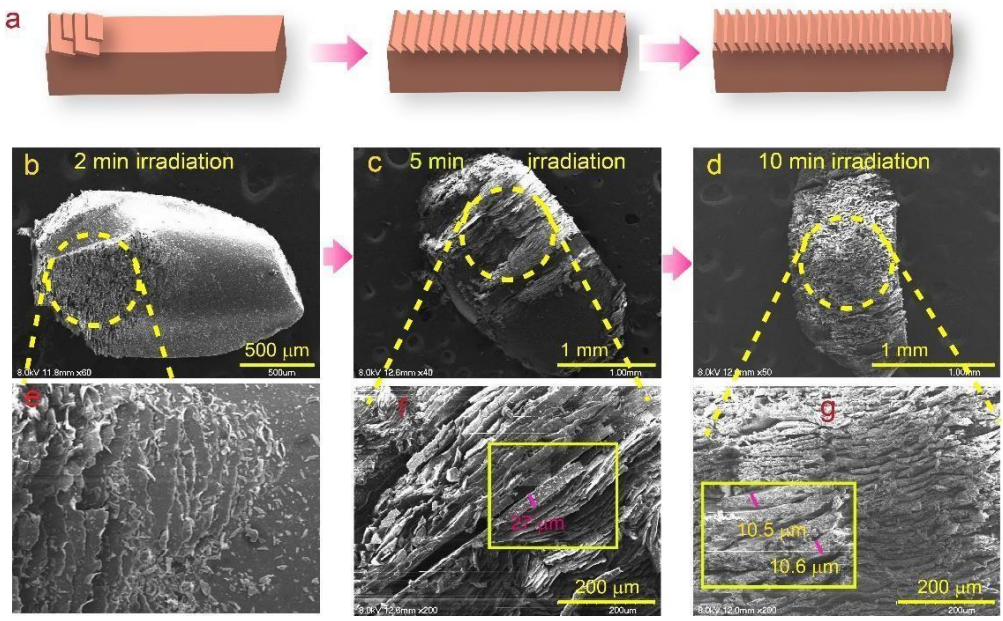

Figure 9. Scanning electron microscope images of the **Ant-H_2O** crystals upon 405 nm light illumination. Images were taken in different time interval. (a) Schematic models of the morphology change upon illumination, (b, e) crystal after 2 minutes irradiation by 405 nm light, (c,f) after 5 minutes irradiation, (d,g) after 10 minutes irradiation

The scanning electron microscope (SEM) images shown above reveal the evolution of surface morphology in **Ant-H_2O** crystals under photo-irradiation. As the irradiation time increases, progressively more layers appear to delaminate or separate from the crystal surface, indicating that photochemical reactions are continuously taking place within the crystal structure. This ongoing reaction results in the formation of multiple new layers, with the interlayer spacing gradually decreasing over time.

Specifically, in Figure f, after 5 minutes of irradiation, the distance between the newly formed layers is measured to be approximately 27 µm. In Figure g, after 10 minutes of irradiation, this spacing reduces significantly to around 10.5 µm. These observations suggest that layer formation becomes more compact as the extent of photo-induced transformation increases, further supporting the dynamic nature of the photomechanical puffing behaviour.

3.3.2 X-ray Structure and Intermolecular Interactions of Ant-H_2O:

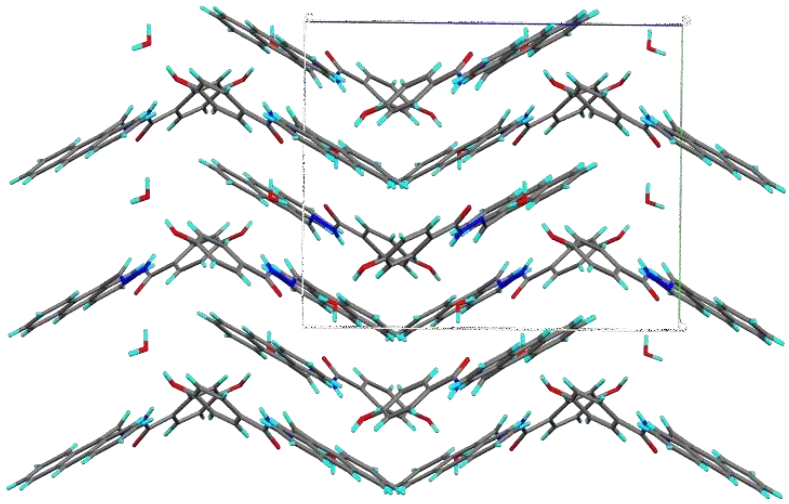

Figure 10. Packing diagram of **Ant-H_2O** crystal, viewed along *a*-axis..

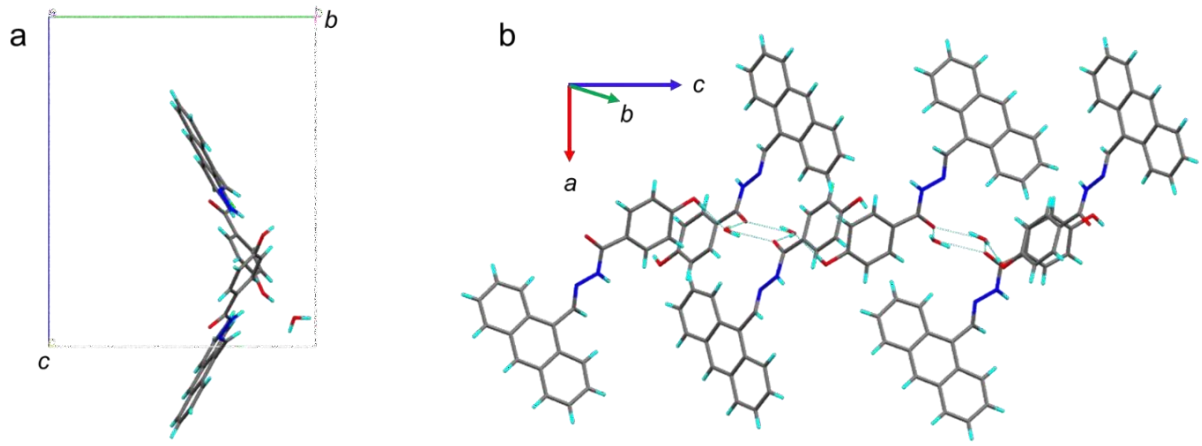

Figure 11. Packing diagram of **Ant-H_2O**, (a) slanting angle between two molecules along c-axis, (b) H bonding interactions involving water solvates

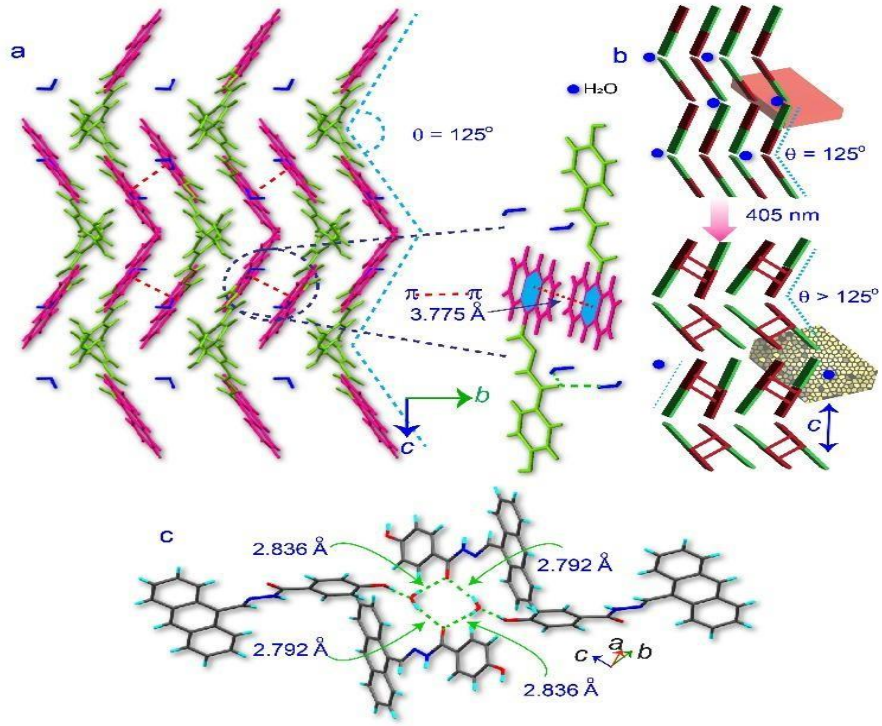

Figure 12. (a) Packing of **Ant-H_2O** molecules in crystal lattice showing $\pi-\pi$ stacking distance in favour of [4+4] cycloaddition, (b) Proposed mechanistic model of packing change upon dimerization and subsequent increase of inclination angle along c-axis that is associated to the expansion of **Ant-H_2O** crystal. (c) Various H-bonding interactions involving lattice water molecule.

Schmidt criteria for solid state photocycloaddition the reacting double bonds should be parallel and within a close distance (typically around 4.2 Å) for the reaction to proceed readily. Closer looks on the crystal faces reveal that the major expansion occurred along the crystallographic *c*-axis. The change in surface morphology was recorded by SEM, which showed that the **Ant-H_2O** crystal changed from smooth surface to loosened slip-stacked layers (interlayer distance ~ 10-15 mm) along *c*-axis of the crystal (Figure 9e-f). This observation suggests that the compact ordered packing of the molecules in the pristine crystal gets disordered due to photoreaction and causes loosening of the layers that results in expansion along *c*-axis (Figure 12b). Apart from puffing behaviour, few **Ant-H_2O** crystals also exhibited photo salient effects, slow jumping displacement during irradiation. **Ant-H_2O** molecule crystallizes from DMSO solution in orthorhombic crystal system with *P*bca space group having one water (H_2O) molecule in the crystal lattice (Figure 10,11). The molecules are arranged in zig-zag fashion along crystallographic *c*-axis having head-to-tail antiparallel orientation of anthracene moiety that are engaged with $\pi-\pi$ stacking interaction having centroid to centroid distance 3.775 Å. This distance satisfies Schmidt's criteria for topochemical reaction (which states that a topochemical cycloaddition reaction in a solid crystal

can occur if the reactive groups are preorganized parallelly within a proximal distance of 4.2 Å) and thus susceptible for photo induced [4+4] cycloaddition reaction.[44] In addition, each of the lattice water molecule form H-bonded supramolecular tetramer with four neighbouring **Ant-H_2O** molecules. Because of the strong H-bonding interactions these lattice water molecules are thermally stable up to 192 ºC (Figure 5). This H-bonding interaction helps to maintain the slanting angle of ~ 126º between two neighbouring molecules that are arranged in zig-zag fashion extended along the crystallographic *c*-axis (Figure 11a). Upon 405 nm light illumination and subsequent [4+4] cycloaddition, the reconfiguration of the **Ant** molecules causes rupturing of the H-bonding interactions and subsequently the water molecules become destabilized and are susceptible to be expelled from the crystal lattice. In fact, TGA thermogram after irradiation shows lower dehydration temperature compared to pristine **Ant-H_2O** crystal (Figure 5). Such reconfiguration due to [4+4] cycloaddition reaction presumably widens the slanting angle between the zig-zag patterned **Ant** molecules which causes destabilization of molecular layers (Figure 12) that results expansion along crystallographic *c*-axis and overall puffing expansion of the **Ant-H_2O** crystal.

3.3.3 NMR, PXRD and IR Analysis: Insights into photo induced actuation:

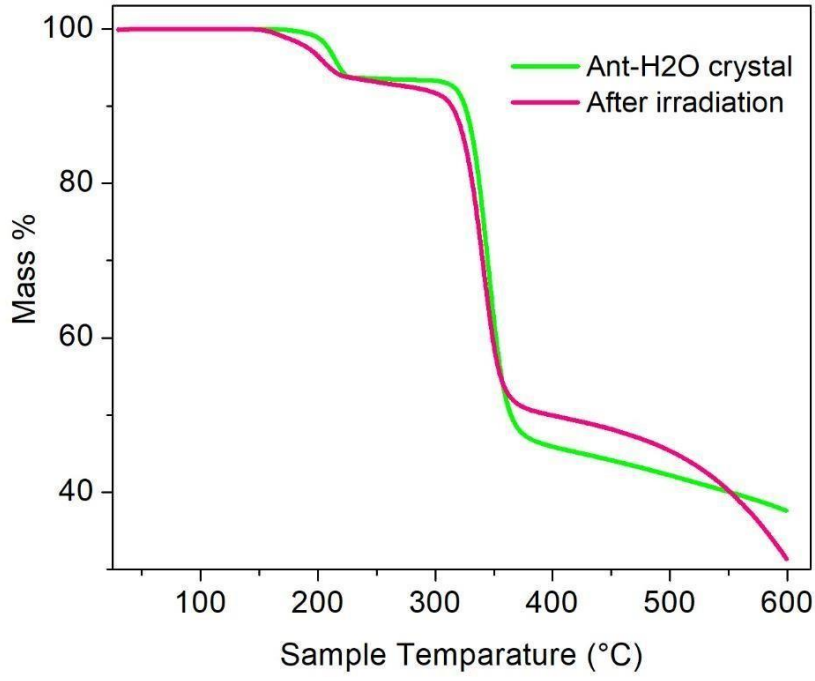

Figure 13. TGA thermogram of **Ant-H_2O** crystal before and after illumination.

Thermogravimetric analysis (TGA) of **Ant-H_2O** crystals after photo-irradiation reveals a noticeable reduction in the dehydration temperature compared to the pristine sample. While the pristine **Ant-H_2O** crystal begins thermal decomposition at approximately 196 °C, the irradiated

crystal shows the onset of decomposition at around 156 °C. This reduction in thermal stability can be attributed to photo-induced molecular reconfiguration, which leads to the disruption of intermolecular hydrogen bonding interactions. As a result, the crystalline water molecules become destabilized and more readily expelled from the lattice upon heating. This behaviour underscores the structural transformation induced by light exposure and its direct influence on the thermal properties of the crystal.

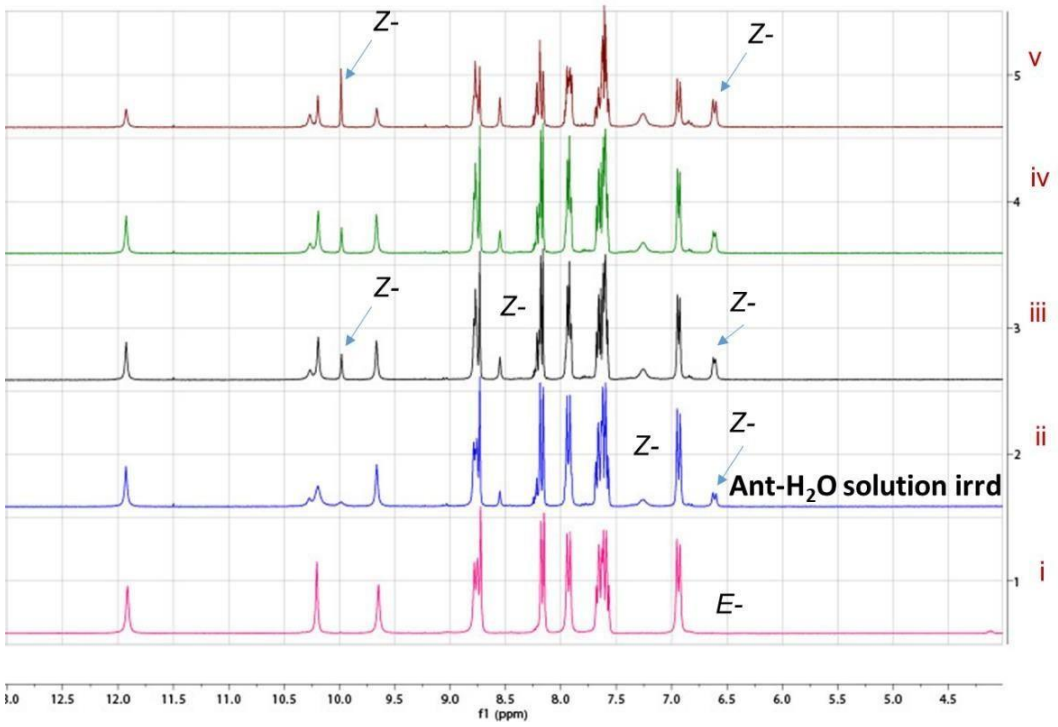

Figure 14. ^{1}H NMR spectra of **Ant-H_2O** crystal in solution state. The solutions (in d_6-DMSO) were irradiated under UV light for different time interval then NMR spectra was recorded. i, ii, iii, iv & v NMR spectra were taken after 0, 15 min, 30 min, 45 min & 1h irradiation respectively which show gradual increase of the ^{1}H NMR peaks of *Z*-isomer. No cycloaddition product was observed in solution phase.

The presented spectrum corresponds to the solution-state ^{1}H NMR spectra of the **Ant-H_2O** crystal. Approximately 5 mg of the crystal sample was dissolved in 0.6 mL of d_6-DMSO solvent for the analysis. A series of five spectra were recorded at 15-minute intervals, and the resulting data were stacked sequentially to monitor temporal changes in the proton environment. Over time, the emergence of a characteristic ^{1}H NMR peak corresponding to the Z-isomer was clearly observed, indicating a photo induced isomerization process occurring in the solution phase upon irradiation. Importantly, no signals corresponding to cycloaddition products were detected, suggesting that the photochemical transformation in solution exclusively leads to Z-isomer formation without undergoing any [4+4] or other cycloaddition reactions.

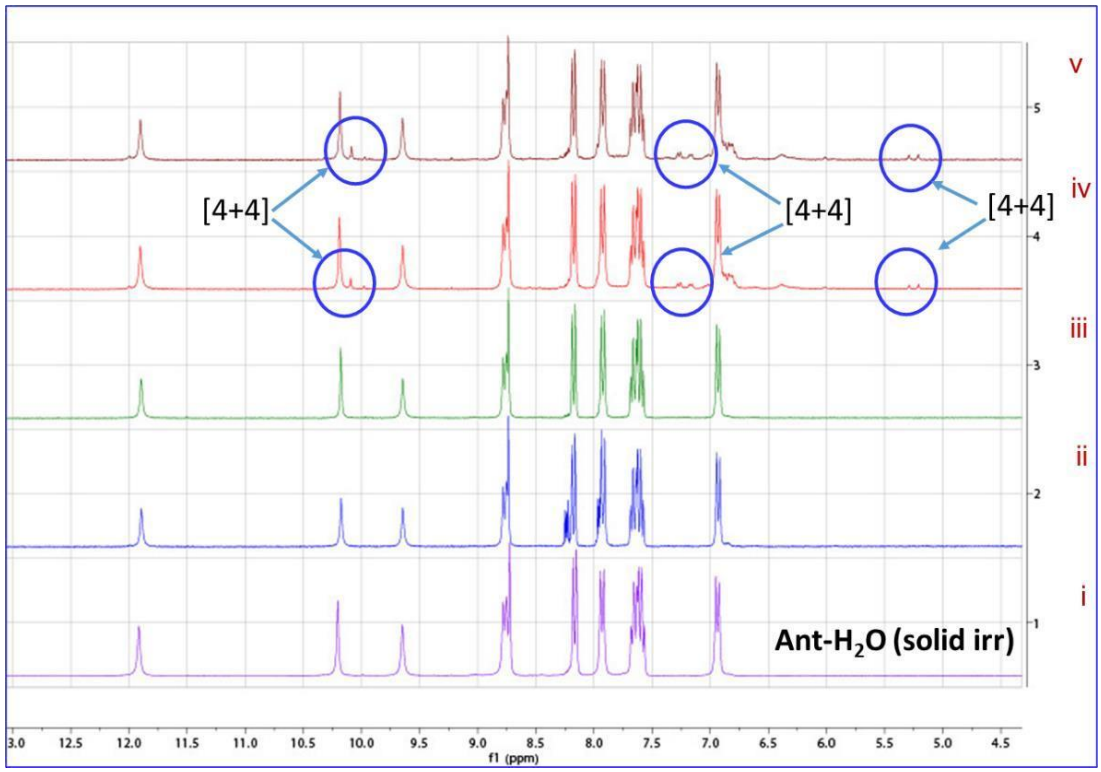

Figure 15. ^{1}H NMR spectra of **Ant-H_2O** crystal in solid state. The crystals were irradiated by 405 nm light for different time interval (0, 30 min, 1h, 2h & 3h) and then d_6-dmso was added & ^{1}H NMR spectra were recorded. The spectra i, ii, iii, iv & v were taken after irradiation of above mentioned time interval. Note that, only cycloaddition product was formed in solid-state illumination, no *E*-to *Z*- isomerization product was formed.

The presented spectra correspond to the solid-state ^{1}H NMR analysis of the **Ant-H_2O** crystal. Approximately 5 mg of the crystalline sample was dissolved in 0.6 mL of d_6-DMSO for spectral acquisition. A total of five spectra were recorded at irradiation time points of 0 min, 30 min, 1 hour, 2 hours, and 3 hours, with the crystal being irradiated in its solid state prior to dissolution. The resulting data were stacked sequentially to monitor the evolution of chemical species over time. With increasing irradiation time, the appearance of distinct ^{1}H NMR peaks corresponding to both the Z-isomer and a dimeric species was observed. This clearly indicates that photoinduced isomerization and dimerization are both operative in the solid state under light exposure. Therefore, the mechanism of the photomechanical puffing behavior exhibited by the **Ant-H_2O** crystal arises from a synergistic effect of photoinduced Z-isomer formation and [4+4] photodimerization processes occurring within the crystal lattice. When the solid **Ant-H_2O** crystals were irradiated with UV light for several hours and then dissolved in dmso-d_6 solvent to record ^{1}H NMR, [4+4] cycloaddition product formed with 9-10 % conversion (Figure 15). **Ant-DMF** crystals showed lower conversion compared to **Ant-H_2O** crystals (Figure 15). This

confirms that higher order and periodic arrangement of molecules in solid crystal facilitate π- π stacking of anthracene to bring them within the Schimdt's critical distance for topochemical [4+4] reaction that is primarily responsible for macroscopic response of the crystals.

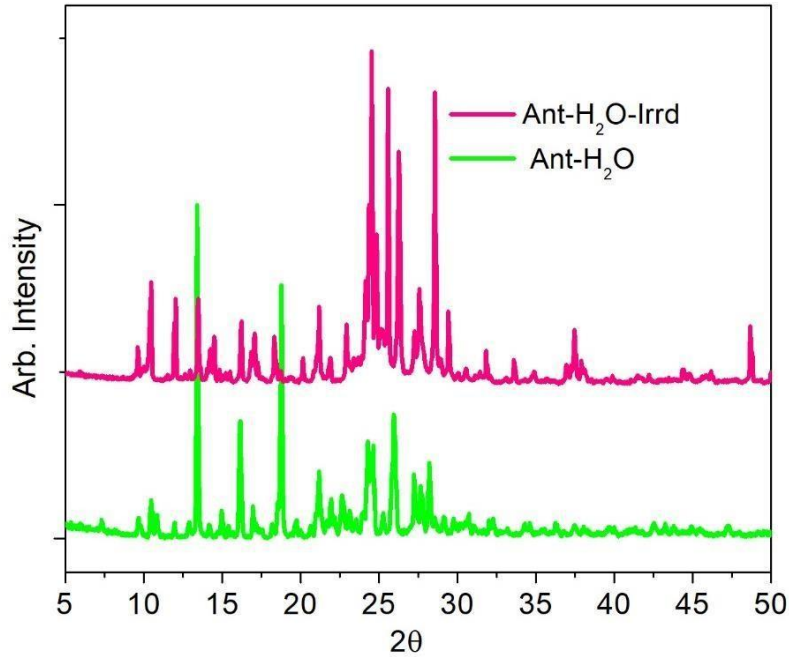

Figure 16. Full PXRD plots of **Ant-H_2O** crystal before and after irradiation by 405 nm light

The powder X-ray diffraction (PXRD) patterns of the **Ant-H_2O** crystal, recorded before and after photo irradiation, display significant changes in both the position and intensity of diffraction peaks (Figure 25). These alterations clearly indicate a modification in the crystal packing, suggesting a rearrangement of the lattice upon light exposure. Such changes are characteristic of a solid-state transformation triggered by a photochemical reaction. In this case, the observed diffraction pattern evolution supports the occurrence of a topochemical [4+4] cycloaddition reaction between adjacent anthracene moieties within the crystal lattice. The preservation of crystallinity, despite the structural reorganization, further validates the topochemical nature of the reaction, wherein the reaction proceeds with minimal atomic displacement, guided by the preorganized molecular arrangement. This structural transition under light stimulation highlights the inherent photoresponsiveness of the **Ant-H_2O** crystal and confirms its potential as a dynamic material for light-driven molecular motion or actuation.

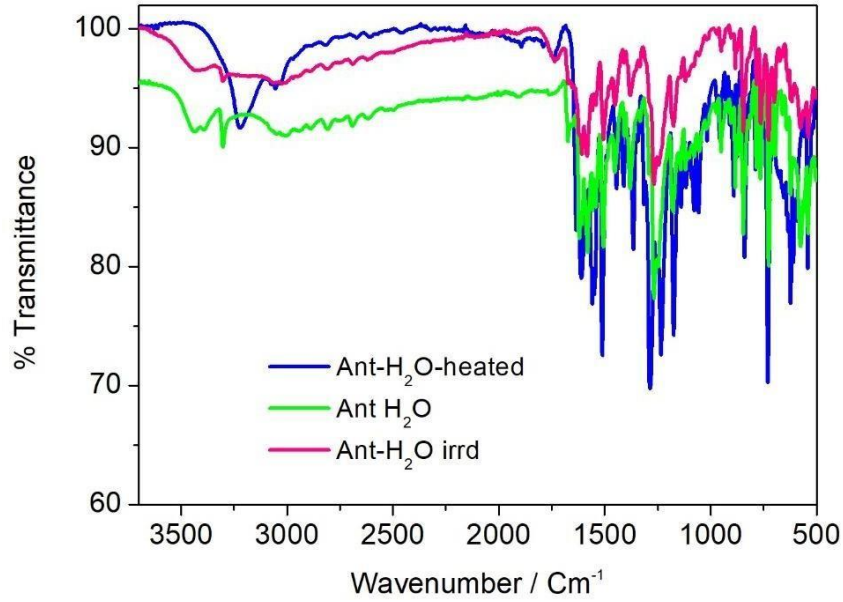

Figure 17. FT-IR spectra of **Ant-H_2O** crystal before, after irradiation and after heating to 210 ^{o}C.

For **Ant-H_2O**, the IR spectrum (Figure 17) shows notable changes after photo irradiation, particularly in the peak shape and intensity at 3441 and 3391 cm^{-1}, which correspond to the vibrational modes of lattice water. The decreased intensity and altered peak profile suggest a possible rearrangement of the lattice water molecules. This is likely a consequence of reconfiguration in the hydrogen-bonding network induced by the photochemical transformation during irradiation.

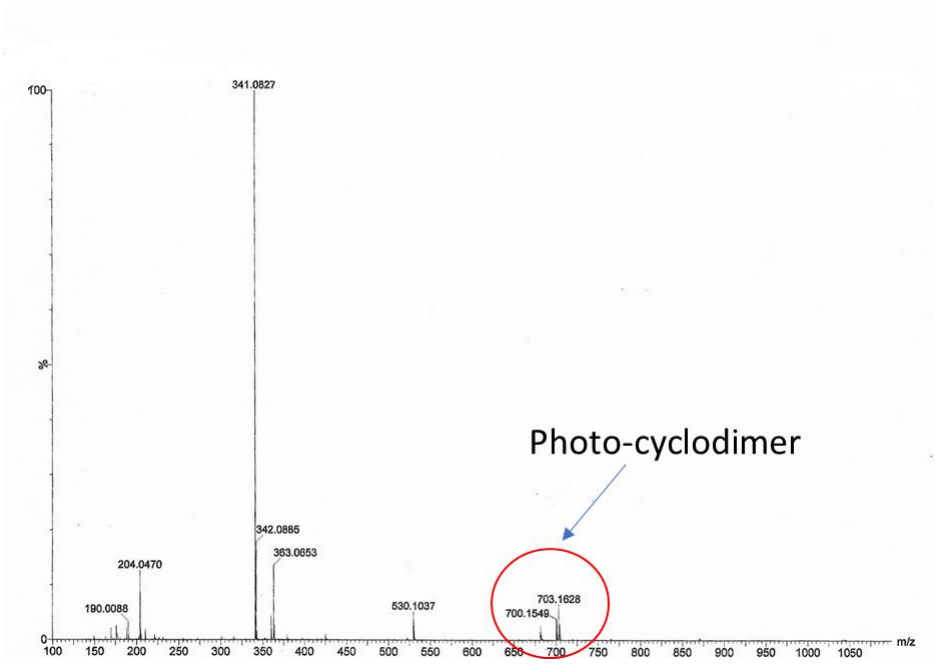

Figure 18. Mass spectrum of **Ant-H_2O** crystal after 405 nm irradiation showing M+23 peak of the dimer at m/z 703.1628 (Calculated for M+23 = 703.24).

The high resolution mass spectrum of the **Ant-H_2O** crystal recorded after 405 nm irradiation reveals a prominent peak at m/z 703.1628, corresponding to $[M + Na]^+$ of the dimeric species. This observed value is in close agreement with the calculated m/z of 703.24, confirming the formation of the photodimer upon light-induced transformation.

3.3.4 Photo induced chopping property of Ant-DMF:

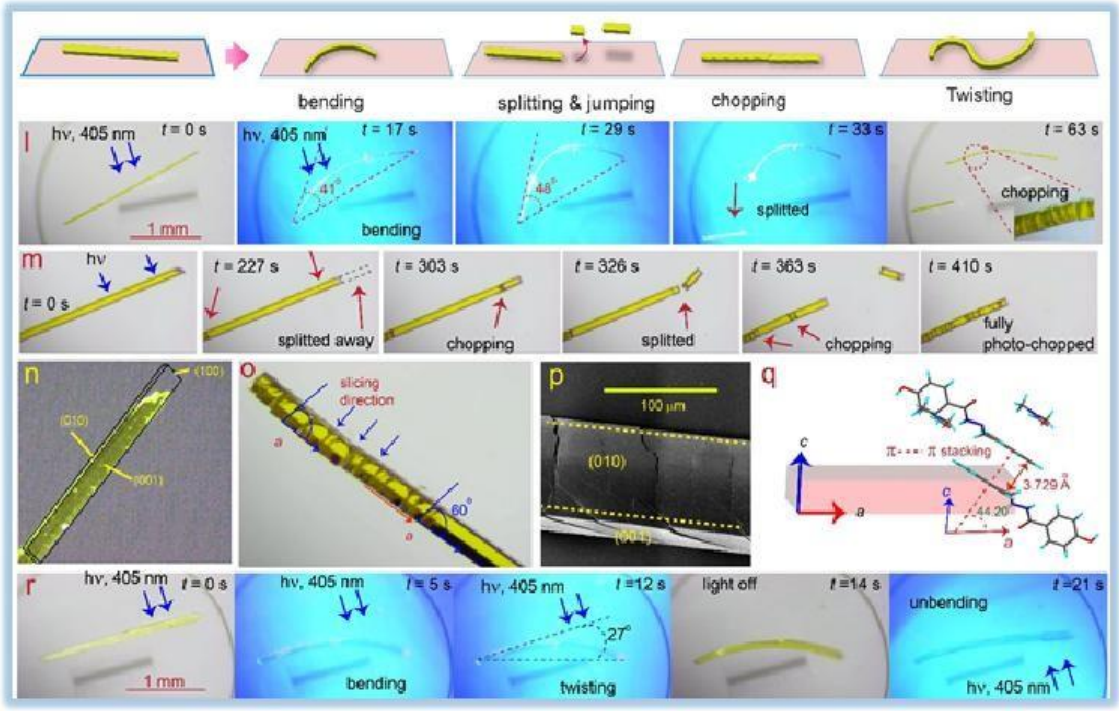

Figure 19. Photo-induced actuation (bending, chopping, twisting & jumping) of **Ant-DMF** crystal in 405 nm light. Chopping of the crystal takes place at 48° angel.

The solvate **Ant-DMF** displays cantilever type bending, twisting, slicing, and splitting upon illumination with 405 nm light (100 mW) because of [4+4] photo-dimer formation (Figure 19k-r). When 405 nm light was shone on (001) face of a thin **Ant-DMF** crystal (dimension: 2.5 mm x 0.18 mm x 0.05 mm), it readily bends away from the light source within 5s and attains maximum bending angle of 48º within 29 s (Figure 19), after which the crystal starts chopping at the different parts which propagate rapidly throughout the length of the crystal and eventually whole crystal is chopped due to strain developed in the crystal interior as a result of photo dimerization reaction. Interesting to note that, for a specific **Ant-DMF** crystal, the chopping/slicing density (i.e the number of chopping lines per unit longitudinal length of the crystal) increases with irradiation time. On the other hand, for a constant illumination time, the chopping density is more for thinner crystals compared to the thicker crystals. Such photo-chopping of organic crystals is visually impressive and rarely observed in literature reports.

Interestingly, the slicing of the crystal was also observed under ambient light (Figure 19m), but the rate of slicing is much slower compared to 405 nm light. However, unlike 405 nm light illumination, the crystals do not bend before slicing under visible or white light. Slicing or bending is not reversible, keeping the chopped crystal in 100 ºC heating for 5-6 hours does not results any unbending or curing of the chopped marks. Interestingly, a closer look on the slicing pattern reveals that the slicing line makes approximately 55º angle with respect to the longitudinal axis of the crystal (parallel to crystallographic *a*-axis, Figure 19n,o). This is possibly due to the alignment of the anthracene moiety which when dimerized to form C–C σ–bond creates strain along the chopping marks, a phenomenon resembling chopping by a knife. Single crystal X-ray diffraction study reveals that the angle between *a*-axis (along the length of the crystal) and direction of new C–C bond formation (for photo dimer) is approximately 44.20º which closely matches with the slicing angle (Figure 19q, more elaborate discussion on X-ray structure and packing is given in Figure 10,11). Apart from bending and chopping, few **Ant-DMF** crystals display twisting motion (Figure 19r).

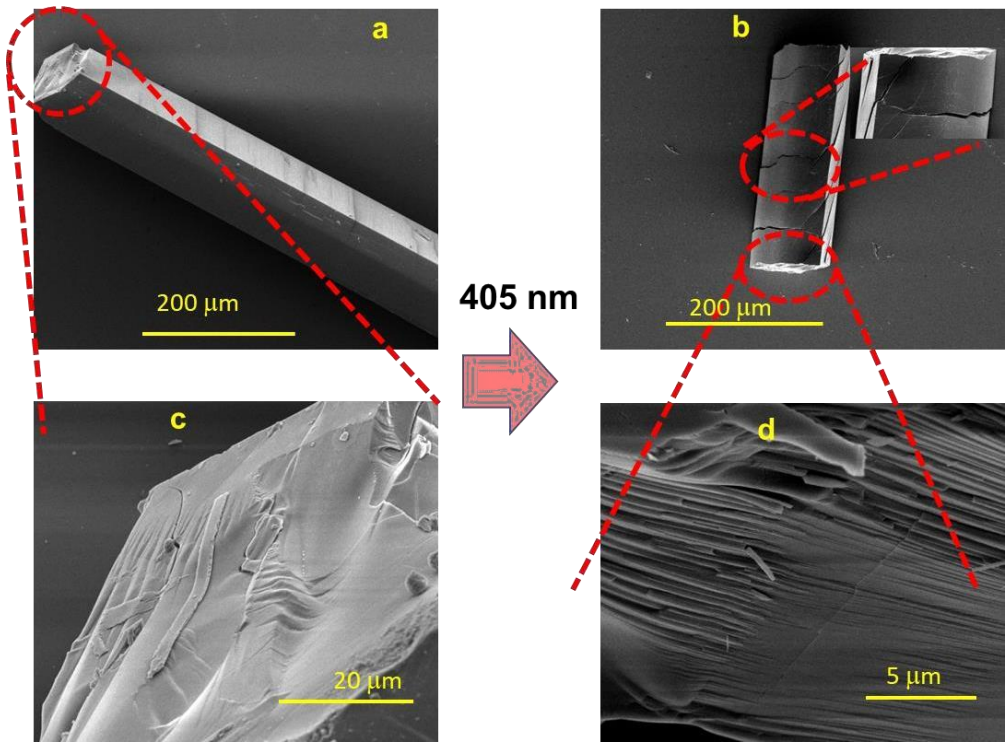

Figure 20. Scanning electron microscope (SEM) images of the **Ant-DMF** crystals upon UV light illumination showing the change in morphology of (100) face (a, c, d) upon 365 nm light illumination.

The scanning electron microscope (SEM) images shown above reveal the evolution of surface morphology in **Ant-DMF** crystals under photo-irradiation. As the irradiation time increases, progressively more layers appear to delaminate or separate from the crystal surface, indicating

that photochemical reactions are continuously taking place within the crystal structure. This ongoing reaction results in the formation of multiple new layers, with the interlayer spacing gradually decreasing over time.

3.3.5 X-ray Structure and Intermolecular Interactions of Ant-DMF:

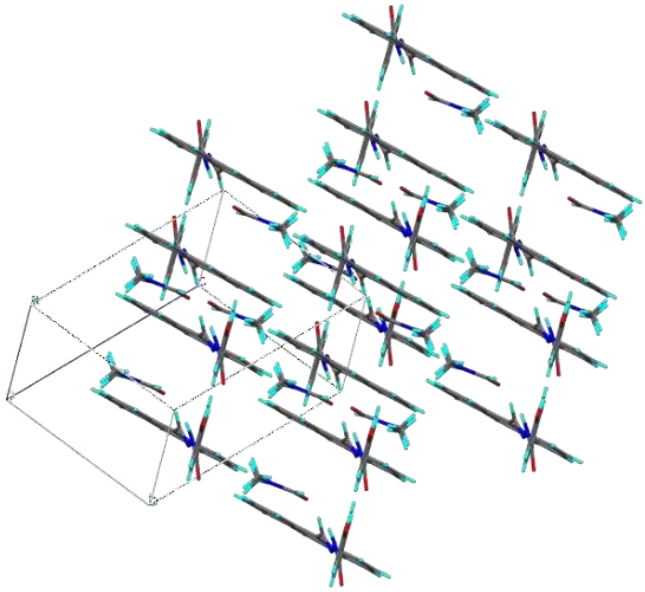

Figure 21. Packing diagram of **Ant-DMF** molecules.

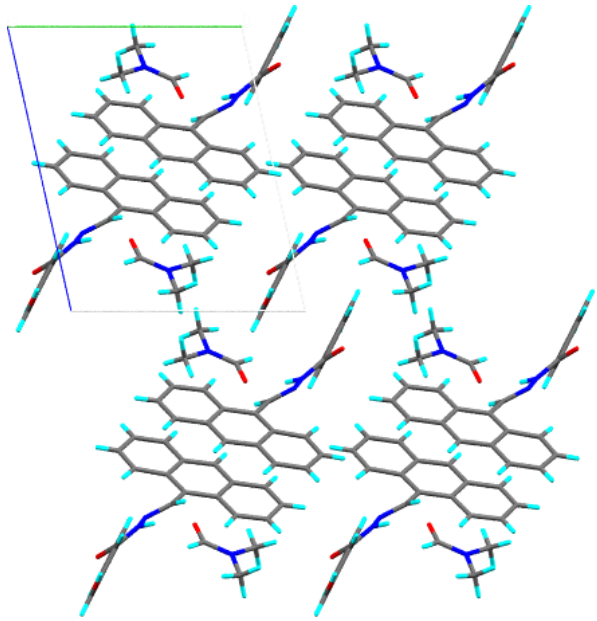

Figure 22. Packing diagram of **Ant-DMF** molecules viewed along *a*-axis.

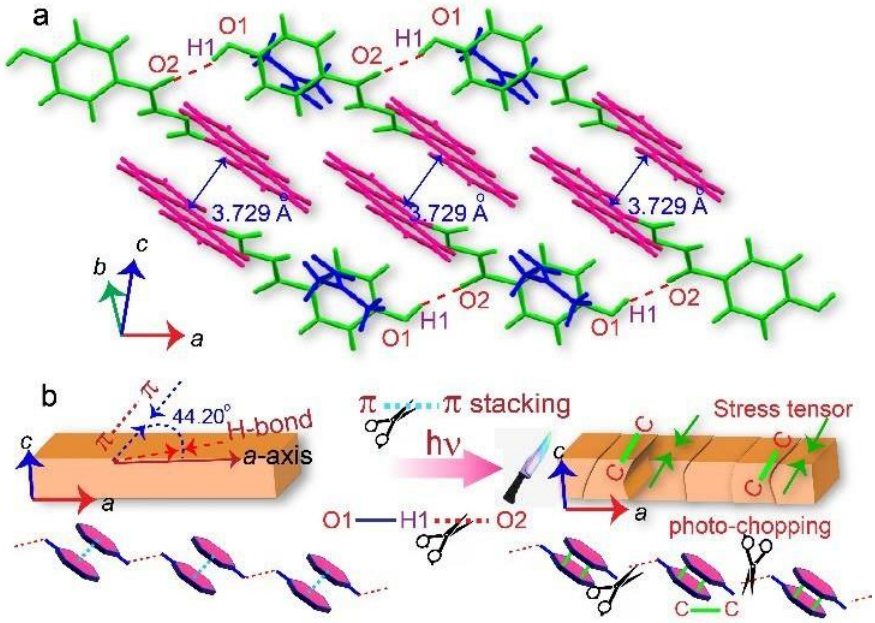

Figure 23. (a) Packing arrangement of **Ant-DMF** molecules in the crystal lattice showing π–π stacking distance and H-bonding interactions, (b) Possible mechanism of photo-chopping of **Ant-DMF** crystal upon light irradiation.

Ant-DMF was crystallized in triclinic form with *P*-1 space group having one DMF molecule in the crystal lattice. The anthracene molecules are also oriented in head-to-tail antiparallel fashion having anthracene π–π stacking distance 3.729 Å which is within the facile distance for Schimdt's topochemical cycloaddition reaction (Figure 23a). This distance is much shorter than that observed in **Ant-H_2O** crystal (3.775 Å). Moreover, the molecules are stitched by strong H-bonding interactions (O1-H1●●●O2 = 2.692 Å, D–A distance) along the length of the crystal (∥ to *a*-axis) that is responsible for maintaining crystal integrity. Crystallographic face indexing of **Ant-DMF** crystal reveals that the (001) is the highest surface area (Figure 19n). On this face, the molecules are arranged in such a manner that π–π stacked anthracenes roughly form an angle of ~ 44º with respect to crystal length parallel to *a*-axis (Figure 23a). When 405 nm light shown on this face, top molecular layers convert to [4+4] photo dimer products and creates an interfacial stress along the direction of the newly formed C–C bond of the cyclodimer (~ 44º with respect to *a*-axis) that could be the possible source of the chopping of the crystal. The reconfiguration of the molecules due to photoreaction disrupts the H-bonding chain along *a*-axis (along the length) and crystal loses its integrity.

3.3.6 NMR, TGA,PXRD and IR Analysis:Insights into photo induced actuation:

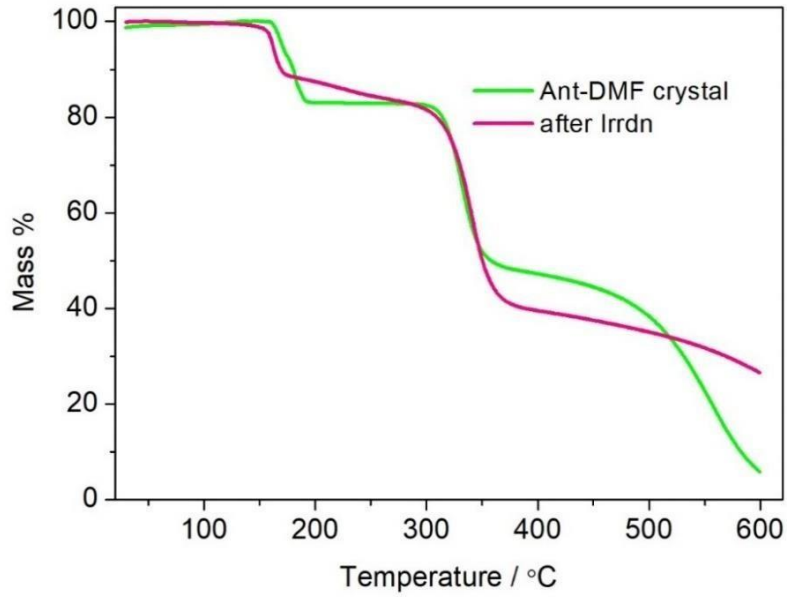

Figure 24. TGA thermogram of **Ant-DMF** crystal before and after illumination.

Thermogravimetric analysis (TGA) of **Ant-DMF** crystals after photo-irradiation reveals a noticeable reduction in the solvation temperature compared to the pristine sample. While the pristine **Ant-DMF** crystal begins thermal decomposition at approximately 163 °C, the irradiated crystal shows the onset of decomposition at around 145 °C. This reduction in thermal stability can be attributed to photo-induced molecular reconfiguration, which leads to the disruption of intermolecular hydrogen bonding interactions. As a result, the crystalline DMF molecules become destabilized and more readily expelled from the lattice upon heating. This behavior underscores the structural transformation induced by light exposure and its direct influence on the thermal properties of the crystal.

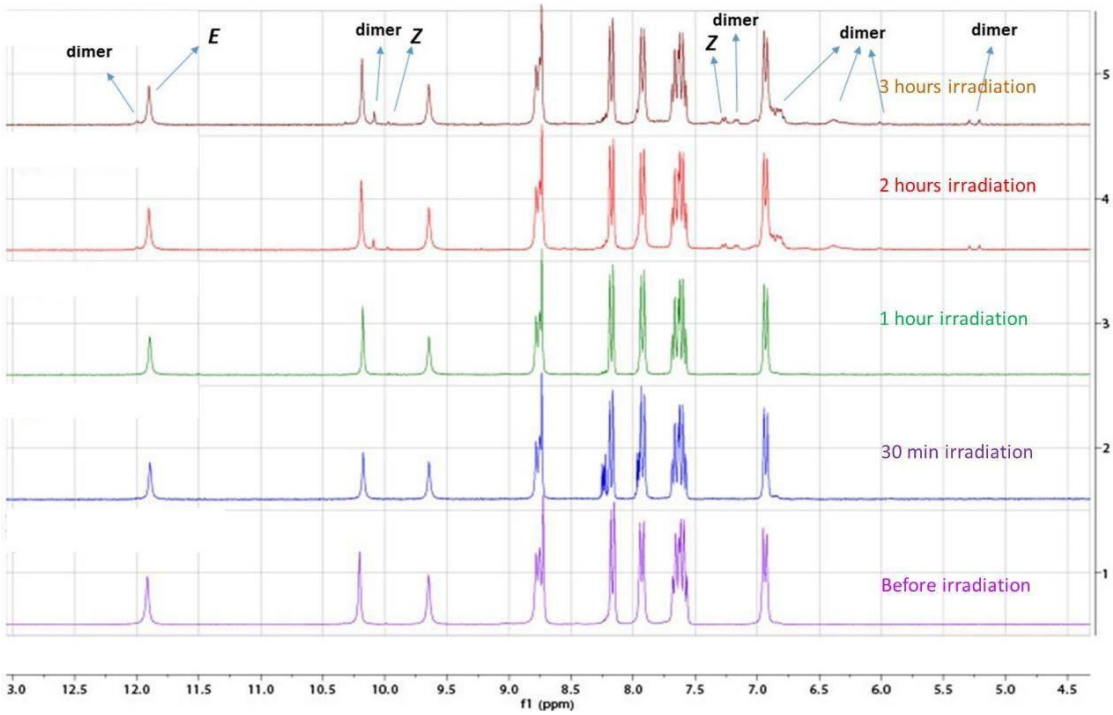

Figure 25. ^{1}H NMR spectra of **Ant-DMF** crystal after irradiation. The crystals were irradiated by 405 nm light for different time interval (30 min, 1h, 2h & 3h) and then dissolved in d_6-dmso & ^{1}H NMR spectra were recorded in solution. The spectra clearly show the *E*- to *Z*- isomerized product as well as cycloaddition product upon light irradiation.

To understand the molecular level mechanism, we have carried out a systematic study by ^{1}H NMR spectroscopy and HRMS study for both the crystals. It is interesting to note that photo-responsive behaviour is very different in solid state compared to the solution state. When the dmso-d_6 solution of **Ant-DMF** was irradiated with UV light, *E*- to *Z*- isomerization occur predominantly without any trace of [4+4] cycloaddition product in solution. However, when the solid **Ant-DMF** crystals were irradiated with UV light for several hours and then dissolved in dmso-d_6 solvent to record ^{1}H NMR, [4+4] cycloaddition product formed with 5-6 % conversion (Figure 25).

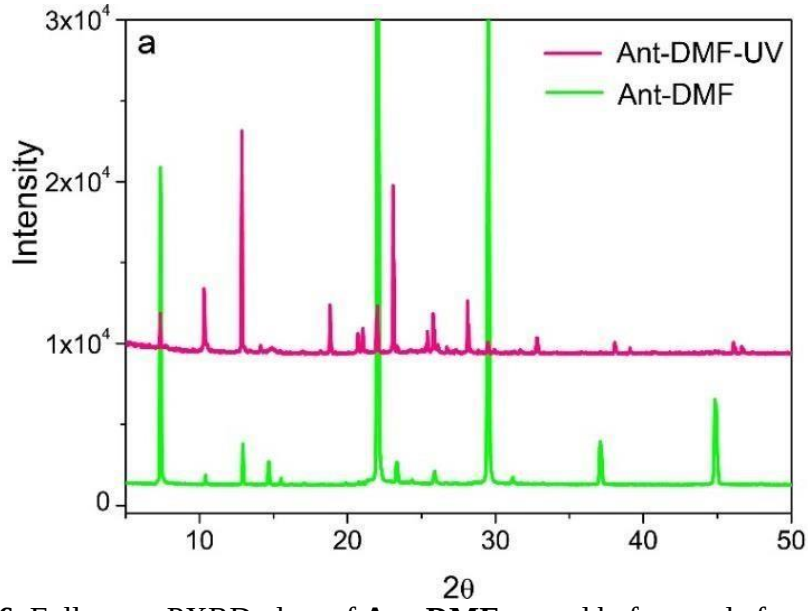

Figure 26. Full range PXRD plots of **Ant-DMF** crystal before and after irradiation.

PXRD profiles of **Ant-DMF** displayed distinct diffraction profiles before and after the illumination (Figure 26) suggesting the lattice rearrangement upon photoreactions. Thus, it is established that both the crystal undergoing topochemical [4+4] cycloaddition reaction upon light illumination.

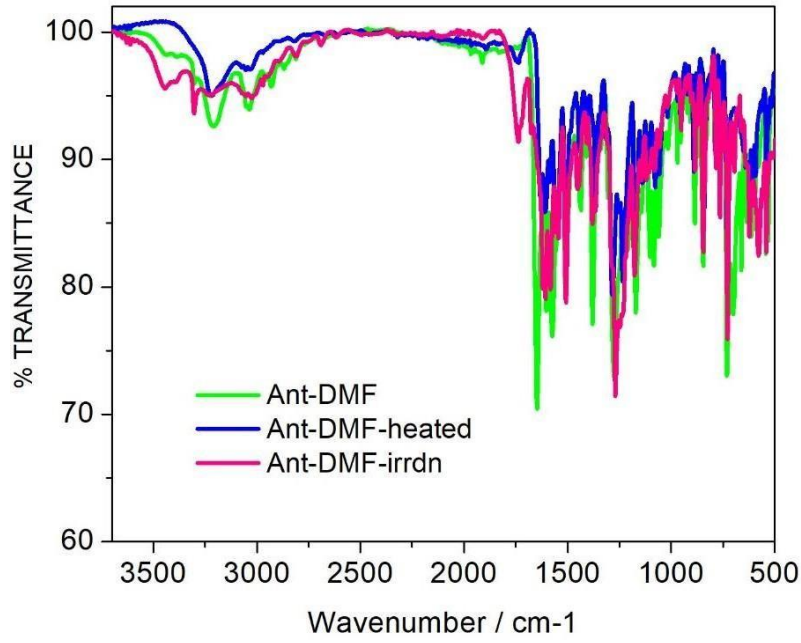

Figure 27. FT-IR spectra of **Ant-DMF** crystal before, after irradiation and after heating to 210 ºC.

For **Ant-DMF**, the IR spectrum (Figure 27) shows notable changes after photo irradiation, particularly in the peak shape and intensity at 3302 and 3209 cm^{-1}, which correspond to the

vibrational modes of hydroxyl group in presence & in absence of hydrogen bonding with DMF molecules respectively. The decreased intensity and altered peak profile suggest a possible rearrangement of the hydroxyl group of **Ant-DMF** molecules. This is likely a consequence of significant molecular rearrangement upon photo irradiation.

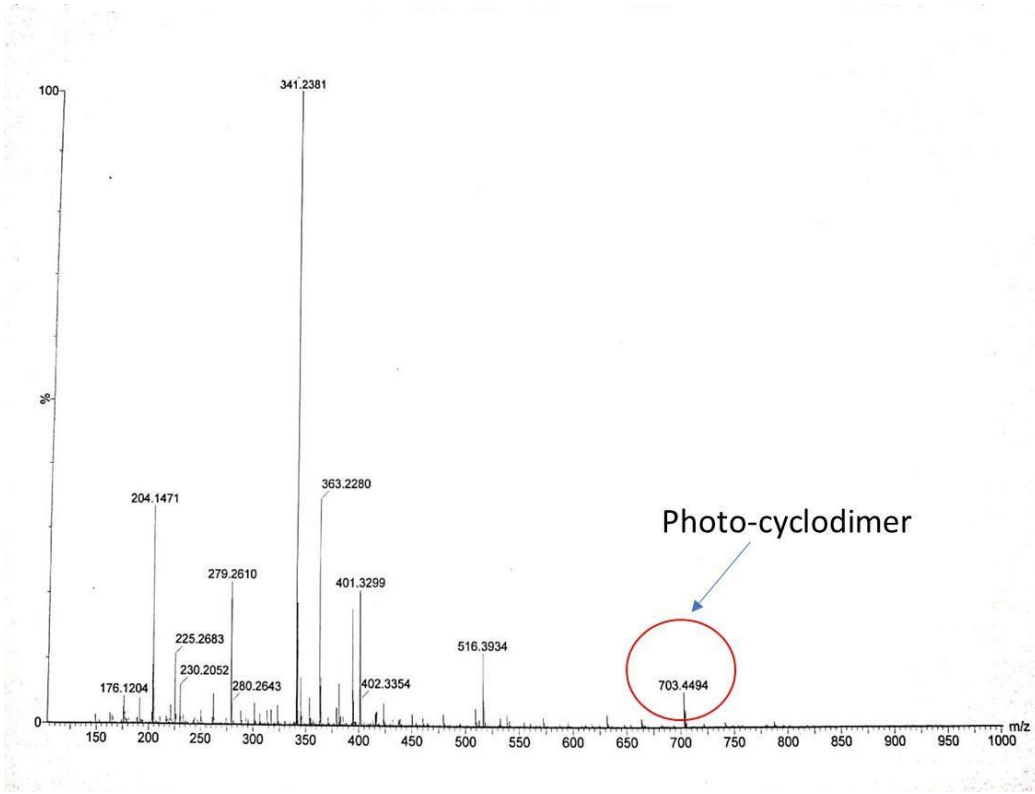

Figure 28. Mass spectrum of **Ant-DMF** crystal after 405 nm irradiation showing M+23 peak of the dimer at m/z 703.4494 (Calculated for M+23 = 703.24)

The high resolution mass spectrum of the **Ant-DMF** crystal recorded after 365 nm irradiation reveals a prominent peak at m/z 703.4494, corresponding to $[M + Na]^+$ of the dimeric species. This observed value is in close agreement with the calculated m/z of 703.24, confirming the formation of the photo dimer upon light-induced transformation.

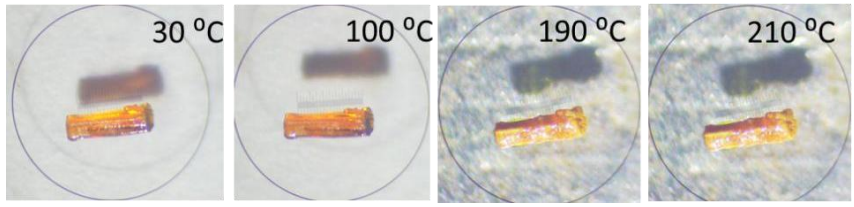

Figure 29. Heating of **Ant-H_2O** crystal to 210 ºC. No puffing on the surface was observed.

3.4 Applications: Procedure volume expansion study for Ant-H_2O crystal:

A cuboidal shaped crystal of **Ant-H_2O** (dimension: 1 mm x 0.68 mm x 0.85 mm) was mounted in a goniometer of X-ray diffractometer. The initial dimension was measured by manually rotating the crystal in the goniometer. The crystal was then exposed to 405 nm light and the crystal dimensions were measured in a specific irradiation time (after 5, 10, 15, 20, minute till we see a no change upon irradiation. The volume of the crystal was calculated using formula, V = length x width x height (mm^3).

Procedure for liquid absorption study of Ant-H_2O crystal:

Liquid drop absorption experiments were carried out using freshly prepared **Ant-H_2O** crystal. Different dye solutions such a Rhodamine-6G, Rhodamine B, Phenolphthalein, fluorescein (5 x 10^{-3} M solution in ethanol) was used. For pre-irradiated crystal experiments, a **Ant-H_2O** crystal (dimension 5.5 mm x 2.6 mm x 0.7 mm) was illuminated under 410 nm light for 9 minutes to obtain a photo converted porous surface. A solution of rhodamine 6G (5 x 10^{-3} in ethanol) was taken in a micro-syringe and added to the crystal surface drop wise with simultaneous light illumination. The time for complete absorption of each drop was recorded and then the next drop was added. Whole process was recorded under microscope to extract the time span of each liquid drop absorption by the crystal. Volume of each drop was calculated and total volume consumed by the crystal surface was also calculated (see below).
1 drop rhodamine 6G = 4 x 10^{-3} mL, *n*-no of drops consumed = n x 4 x 10^{-3} mL liquid (total volume consumed by the crystal).

Calculation of rate of absorption: At a fixed room temperature (33 ºC) we have added the drops in the crystal surface and recorded the time of absorption of the liquid in presence of photoirradiation. Rate of absorption can be calculated as the volume of liquid absorbed by the crystal surface at a specific time range (e,g 5- 10 seconds) assuming that the rate of absorption is constant over the time period of absorption.

Average rate of absorption = volume consumed / consumption time

Control experiment: (blue curve in figure 29d) was carried out in the same way using a freshly prepared pristine crystal. Typically, Rhodamine-6G (5 x 10^{-3} M solution in ethanol) was

dropped on the surface of a freshly prepared **Ant-H_2O** crystal and time of droplet consumption without light irradiation under normal atmosphere was noted. The rate of absorption was calculated using the same procedure described above.

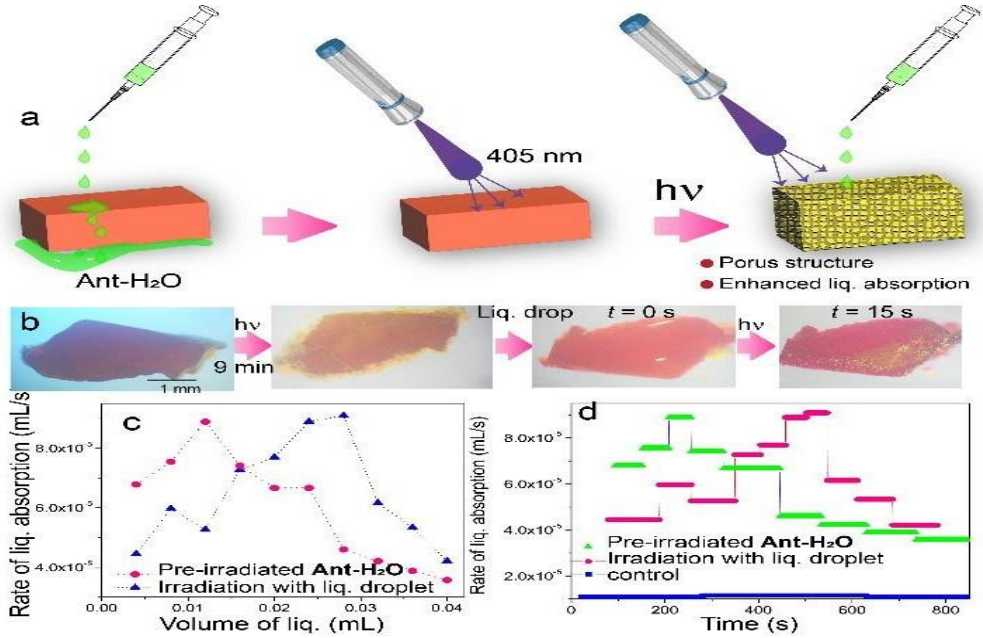

Figure 30. (a) Model representation of sponge like liquid absorption by pre-irradiated Ant-H_2O crystal, (b) Snapshots of pre-irradiation of **Ant-H_2O** crystal (for 9 mins) and subsequent liquid absorption by the irradiated porous crystal, (c) Plot of rate of liquid absorption vs volume of the liquid, (d) Plot of the rate of liquid absorption vs time (s). The blue curve in panel (d) shows the control experiment in which liquid absorption of a pristine non-irradiated crystal was studied.

3.5 Crystallographic data table of Ant-H2O & Ant-DMF crystal:

Table S1. Single crystal X-ray parameters of **Ant-DMF** and **Ant-H_2O** at 273 K.

	Ant-DMF	**Ant-H_2O**
CCDC No.	2297557	2297556
Chemical formula	$C_{25}H_{23}N_3O_3$	$C_{22}H_{18}N_2O_3$
Moiety Formula	$C_{22}H_{16}N_2O_2$, C_3H_7NO	$C_{22}H_{16}N_2O_2$, H_2O
*M*r	413.46	358.38
Crystal system	Triclinic	Orthorhombic
Space group	*P*-1	*Pbca*
a / Å	8.5268(7)	12.5288(13)
b / Å	10.0331(8)	14.8467(13)
c / Å	12.5681(10)	18.3499(17)
α/ °	77.050(2)	90
β/ °	81.762(2)	90

γ / °	86.570(2)	90
V / Å^3	1036.62(14)	3413.3(6)
Z	2	8
ρ_{calc} / (g cm^{-3})	1.325	1.395
μ / mm^{-1}	0.088	0.094
F_{000}	436	1504
θmin / °	2.41	2.744
θmax / °	33.03	29.597
Reflections collected	7648	4746
Independent reflections	5202	3876
GoF	1.090	1.070
Final *R* indices [$I > 2\sigma(I)$]	R_1 = 0.0704, wR_2 = 0.1938	R_1 = 0.0533, wR_2 = 0.1477
R indices (all data)	R_2 = 0.1096, wR_2 = 0.2502	R_2 = 0.0668, wR_2 = 0.1661

Table S2. Noncovalent intermolecular interactions in **Ant-DMF** and **Ant-H_2O** crystals

	D–H●●●A	**D–A distance / Å**	**<DHA angle /º**
Ant-DMF			
	C8–H8●●● O111	3.246(2)	142.6
	C112–H11A●●●O1	3.433(3)	151.4
	N2–H2●●●O111	2.8604(18)	160.8(18)
	O1–H1●●●O2	2.6916(19)	152(3)
Ant-H2O			
	O1–H1●●● O111	2.6863(17)	178.8
	N1–H6●●● O1	3.2111(16)	156.1
	C8–H7●●● O1	3.3984(18)	149.3
	C2–H2 ●●●O111	3.2674(18)	129.6

3.6 Conclusion

In conclusion, we have developed two new crystal solvates (**Ant-H_2O** and **Ant-DMF**) that displayed very different photomechanical behaviour under UV and 405 nm light. **Ant-H_2O** showed novel photo-puffing behaviour with large volume expansion and enhanced surface porosity as a result of [4+4] cycloaddition reaction under UV light that resembles the puffing of rice grains under heat treatment which results in largely expanded puffed rice having higher porosity compared to pristine rice grains. Utilizing the photoconverted porosity of these crystals, we have successfully demonstrated "spongy behaviour" that can absorbs various types of dye solutions. The other solvate **Ant-DMF** behaved very differently under light illumination exhibiting photo-slicing, bending, twisting behaviour because of the stress generation inside the crystal interior due to photoinduced [4+4] cycloaddition reaction. The distinctive photo-responsive behaviours of the two crystal solvates is originated to the relative rearrangement of molecules and lattice solvents that reconfigure differently during photoreaction. Our "crystal solvates" strategy could be extended further for various types of molecules to explore diverse mechanical properties and suitably be integrated for machinery tools, robotics etc.

References

[1] D. Koller, *Plant, Cell and Environment* ,1990, **13**, 615-632.

[2] W. R. Briggs, *Science*, 2016, **353**, 541-542

[3] J. P. Vandenbrink et al., *Plant Biol.* 2014, **224**, 26.

[4] P. Naumov, D. P karathu, E. Ahmed, L. Catalano, P. Commins, J. M. Halabi, M. B. Al-Handawi, L. Li, *J. Am. Chem. Soc.* 2020, **142**, 13256−13272.

[5] S. Kobatake, S, S. Takami, H. Muto, T. Ishikawa, M. Irie, *Nature* 2007, **446**, 778−781.

[6] M. Tamaoki, D. Kitagawa, S. Kobatake, *Cryst. Growth. Des*. 2021, **21**, 3093−3099.

[7] S. Khan, B. Dutta, S. Naaz, B. Choudhury, P. A. Cazade, E. Kiely, S. Guerin, R. Medishetty, M. H. Mir, *Commun Chemistry*, 2023, **6**, 150.

[8] P. Naumov, S. Chizhik, M. K Panda, N. K. Nath, E. Boldyreva, *Chem Rev*, 2015, **115**, 2440−12490.

[9] B. B. Rath, J. J Vittal, *Chem. Mater*. 2021, **33**, 4621-4627.

[10] B. B. Rath, M. Gupta, J. J. Vittal, *Chem. Mater*. 2021, **34**, 178-185.

[11] K. Kato, T. Seki, H. Ito, *Inorg. Chem*, 2021, **60**, 10849−10856.

[12] A. K. Bartholomew, I. B. Stone, M. L. Steigerwald, T. H. Lambert, X. Roy, *J. Am. Chem. Soc*. 2022, **144**, 16773−16777.

[13] Y. S. Chen, C. H. Wang, Y. H. Hu, C. Y. D Lu, J. S. Yang, *J. Am. Chem. Soc*. 2023, **145**, 6024−6028.

[14] F. Tong, D. Kitagawa, I. Bushnak, R. -O. Al-Kaysi, C. J. Bardeen, *Angew. Chem., Int. Ed*. 2021, **60**, 2414−2423.

[15] L. Zhu, R. -O. Al-Kaysi, C. J. Bardeen, *Angew. Chem., Int. Ed.* 2016, **55**, 7073−7076.

[16] E. Ahmed, D. P. Karothu, P. Naumov, *Angew. Chem., Int. Ed*. 2018, **57**, 8837−8846.

[17] F. Terao, M. Morimoto, M. Irie, *Angew. Chem., Int. Ed*. 2012, **51**, 901−904.

[18] Kim, T.; Zhu, L.; Mueller, L. J.; C. J. Bardeen, *J. Am. Chem. Soc*. 2014, **136**, 6617−6625.

[19] S. Ghosh, C. M. Reddy, *Angew. Chem. Int. Ed.* 2012, **51**, 10319 –10323

[20] S. Takamizawa, Y. Miyamoto, *Angew. Chem. Int. Ed*, 2014, **53**, 6970–6973.

[21] A. Worthy, A. Grosjean, M. C Pfrunder, Y. Xu, C. Yan, G. Edwards, J. K Clegg, J. C McMurtrie, *Nat Chemistry*, 2018, **10**, 65-69.

[22] R. Mandal, A. Garai, S. Peli, P. K Dutta, K. Biradha, *Chem, A Eur. J*, 2020, **26**, 396-400.

[23] M. K Panda, T. Runčevski, A. Hussain, P. Naumov*, *J. Am. Chem. Soc*, 2015, **137**, 1895

[24] P. Naumov, S. C. Sahoo, B. A. Zakharov, E. V. Boldyreva, *Angew. Chem. Int. Ed*. 2013, **52**, 9990−9995.

[25] T. Taniguchi, J. Fujisawa, M. Shiro, H. Koshima, T. Asahi, *Chem. - Eur. J.* 2016, **22**, 7950−7958.

[26] L. Zhu, R. O. Al-Kaysi, C. J. Bardeen, *J. Am. Chem. Soc.* 2011, **133**, 12569−12575.

[27] Yue, Y. Shu, K. Ye, J. Sun, C. Liu, S. Dai, L. Jin, C. Ding, R. Lu, *Chem. - Eur. J.* 2023, **29**, e202203178.

[28] T. Taniguchi, H. Sugiyama, H. Uekusa, M. Shiro, T. Asahi, H. Koshima, *Nat. Commun*. 2018, **9**, 538.

[29] J. M. Halabi, E. Ahmed, S. Sofela, P. Naumov, *PNAS*, 2021, **118**, e2020604118.

[30] Yang, Xuesong; Lan, Linfeng; Pan, Xiuhong; Di, Qi; X. Liu, L. Li, P. Naumov, H. Zhang, *Nat. Commun,* 2023, **14**, 2287

[31] J. M. Halabi, I. Segui, L. Salvagnac, T. Leı¨chle´, T. Saya, F. Mathieu, B. Duployer, D. P. Karothu, L. Nicu, P. Naumov, *Cell Reports Physical Science*, 2022, **3**, 101133.

[32] L. Catalano, D. P. Karothu, S. Schramm, E. Ahmed, R. Rezgui, T. J. Barber, A. Famulari, P. Naumov, *Angew Chem Int Ed.* 2018, **57**, 17254–17258.

[33] Y. Shu, J. Sun, Y. Yue, K Ye, R. Lu, *Chemphotochem*, 2022, **6**, e202200006.

[34] H. Koshima, H. Uchimoto, T. Taniguchi, J. Nakamura, T. Asahib and T. Asahiac, *CrystEngComm*, 2016, **18**, 7305-7310.

[35] K. Morimoto, D. Kitagawa, F. Tong, K Chalek, L. J. Mueller, C. J. Bardeen, S. Kobatake, *Angew Chemie Int Ed*. 2022, **61**, e202114089.

[36] K. Yadava, J. J. Vittal, *Cryst. Growth Des*. 2019, **19**, 2542−2547.

[37] Yi-X Shi, W-H Zhang, B. F. Abrahams, P. Braunstein, J-P Lang, *Angew. Chem. Int. Ed*. 2019, **58**, 9453 –9458.

[38] S. Li, B. Lu, X. Fang, D. Yan, *Angew Chem Int Ed.*, 2020, **59**, 22623-22630.

[39] H. Wang, P. Chen, Z. Wu, J. Zhao, J. Sun, R. Lu, *Angew Chem Int Ed.*, 2017, **56**, 9463-9467.

[40] X. Ma, P. Li, J. Wang, M. Yin, Y. Zhang, Cryst. Growth Des. 2022, **22**, 4133−4138.

[41] P. Giri, A. Mazumder, D. Dey, S. Garani, A. Raveendran, M. K Panda, *CrystEngComm.*, 2021, **23**, 5876-5881.

[42] S Bhandary, M. Beliš, L. Bourda, A. M. Kaczmarek, K V Hecke, *Angew Chem Int Ed.*, 2023, **135**, e-202304722.

[43] R. Medishetty, A. Husain, Z. Bai, T. Runcevski, R. E. Dinnebier, P. Naumov, J J. Vittal, *Angew. Chem. Int. Ed.*, 2014, **53**, 5907-5911.

[44] G. M. J. Schmidt, *Pure and Appl. Chemistry*, 1971, **27 (4)**, 647-678.

[45] T. H. Borchers, F. Topić, J.-C. Christopherson, O. S. Bushuyev, J. Vainauskas, H. M. Titi, T. Friščić, C. J. Barret, *Nat Chem*., 2022, **14**, 574-581.

[46] G. Gogoi, R. J. Sharma, *CrystEngComm*, 2023, **25**, 4582-4591.

[47] APEX3, version 2017.3-0, and SAINT, version 8.38A, Bruker AXS Inc., Madison, WI, 2012, URL: https://www.bruker.com

[48] G. M. Sheldrick, SADABS, University of Göttingen, Göttingen, Germany, 1996 (part of Bruker APEX3 software package (version 2017.3-0): Bruker AXS, 2017).

[49] G. M. Sheldrick, *SHELXTL XT – Crystal Structure Solution*, version 2014/4, Bruker AXS, 2010–2014.

[50] G. M. Sheldrick, SHELXL2014. University of Göttingen, Germany, 2014.

[51] G. M. Sheldrick, *Acta Crystallogr*. A 2015, **71**, 3–8.

[52] G. M. Sheldrick, *Acta Crystallogr*. A 2008, **64**, 112.

CHAPTER-4

Distinct Photoresponsive Behaviour by Cyanovinyl Based Geometric Isomer Crystals

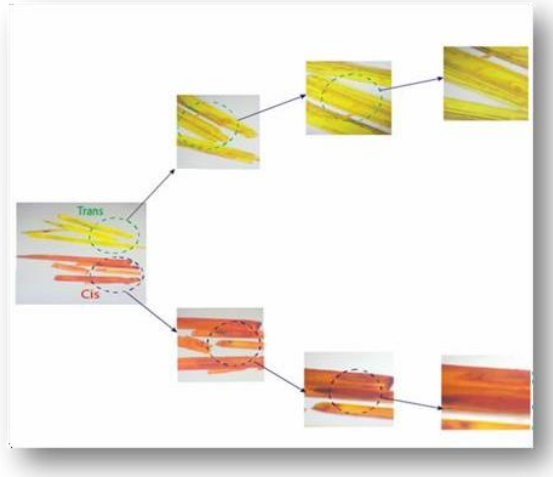

4.1. Introduction

Photomechanical materials can convert light directly into mechanical motion and thereby have immense application in soft robotics and machinery applications[1-3]. While polymer-based systems containing photochromic molecules have been extensively studied,[4-6] molecular crystals armed with photoactive functional group can also exhibit diverse movements when exposed to light.[7-19] To observe shape changes in these crystals, at least one dimension often needs to be on the micron scale or smaller. In larger crystals, the coexistence of reactant and product phases can generate internal strain, potentially leading to fractures and structural failure.[20-22] Previous studies, including those by Naumov and coworkers, have demonstrated that the kinetic energy released during such fracturing events can launch microcrystals across significant distances—a phenomenon known as photosalient effect. However, this process is typically unpredictable and hard to control.[23-25] If crystal fracturing could be induced in a controlled and repeatable manner, it could become a useful feature. Such behavior might be exploited in applications like tunable adhesion, mechanical switches, or self-cleaning surfaces.

The initial step involves identifying a suitable photochemical reaction. To effectively observe the distinct separation between reactant and product regions, the next step is to form crystals with an appropriate morphology. This is crucial because fracture and slippage typically occur along specific crystallographic planes.[26-29] Designing a molecular crystal that undergoes precise fragmentation requires controlling crystal growth to influence its faceting. Studies have shown that modifying variables such as concentration, temperature, and surfactant presence can produce crystals with varying shapes and facet structures in aqueous environments.[30-38]

One of our goals of this project was to design and synthesize molecules that are expected to have light-responsive actuation property. Although many azobenzene based molecules have already been reported in literature, the necessity of developing new molecules having novel physical property seems to be a never-ending effort. Compared to azobenzene-based actuators, cyanovinyl based molecular crystals are comparatively new and thus have a better scope to be explored to a greater extent. Moreover, by changing the photo active group in the molecule, we can attain a diverse range of molecules that could have tunable optical as well as actuation property. In this report, we report a cyanovinyl based molecular crystals (**NMe_2CNF_2**, Scheme 1) that has been isolated in two different isomers, *-cis* (*-Z*) and *-trans* (*-E*) and display very different photo-responsive behaviour in solid state due to distinct structural features. The molecule is armed with $-NMe_2$ donor in one terminal and -CN and -F substituents in the other terminal connected by a conjugated phenyl ring and thus providing a donor-acceptor like

skeleton that facilitate intramolecular charge transfer (ICT). Due to ICT, the molecules are inherently fluorescent in solid state and the colour can be switched by the exposure to various stimuli. Moreover, we envisage that the photoactive functional group C=C-CN may also undergo topochemical cycloaddition reaction if Schmidt's criteria is met in solid state packing, while the auxiliary functional groups (F, CN etc) could provide non-covalent interaction for facile supramolecular reconfiguration during photo isomerization. Bothe the isomers were successfully crystallized and the structures were determined by X-ray crystallography. The crystal with *trans*- configuration is termed as ***E*-NMe$_2$CNF$_2$** while the one with *cis*-configuration is named as ***Z*-NMe$_2$CNF$_2$**. Hereafter. Interestingly, ***E*-NMe$_2$CNF$_2$** display fascinating photo-mechanical actuation & optical wave guiding property when illuminated with 405 nm light. On the other hand, ***Z*-NMe$_2$CNF$_2$** have no mechanical response in presence of 405 nm light but display only wave guiding property. The dual photo-responsive behaviour in a single molecule is rooted to their distinct molecular conformations and packing in the lattices. With the aid of single crystal X-ray diffraction, Powder X-ray diffraction, NMR and other analytical techniques we have investigated the mechanism of functional diversity in these two isomeric crystals.

4.2 Experimental Section

4.2.1. Materials & methods

3,5-difluorobenzylcyanide was purchased from **TCI** and used without further purifications. 4-dimethylaminobenzaldehyde was also purchased from **TCI** and used as commercially received. Potassium *tert*-butoxide was purchased from Merck India. It was used as commercially received. Merck ACS grade (Emplura) solvents were used for synthesis and spectroscopy grade solvents were used for crystallization and spectroscopy studies.

NMR Spectroscopy: Both ^{1}H NMR (300 MHz) and ^{13}C NMR spectra were recorded on a Bruker AVANCE 300 spectrometer using $CDCl_3$ or DMSO-d_6 as the solvent. The chemical shifts (δ) are reported in ppm for precision.

High-Resolution Mass Spectrometry (HRMS): The HRMS of compounds ***E*-NMe$_2$CNF$_2$** & ***Z*-NMe$_2$CNF$_2$** were acquired using a QTOF Micro YA263 mass spectrometer operated in electrospray ionization (ESI) mode.

UV-Vis and Fluorescence Spectroscopy: UV-Vis absorption spectra were recorded with a Shimadzu UV-2401C spectrophotometer in solution and solid-state configurations. For fluorescence studies in the solid state, a HORIBA Jobin Yvon Fluorolomax-4 spectrofluorometer was employed. Additionally, lifetime measurements were performed on a Modular Time-Correlated Single Photon Counting (TCSPC) system equipped with a Delta Flex detector (PPD850).

Infrared Spectroscopy (IR): IR spectra were recorded using a PerkinElmer LX-1 FT-IR spectrometer to examine functional group characteristics and molecular interactions.

Powder X-ray Diffraction (PXRD): PXRD patterns were obtained using a Bruker D8 Advanced Diffractometer with Cu Kα radiation (λ = 1.5418 Å), operating at 40 kV and 40 mA. The Lynxeye detector was utilized for data acquisition with a scanning rate of 0.2 seconds per step over a 2θ range of 0° to 50°.

Single Crystal X-ray Diffraction:

High-quality single-crystal X-ray diffraction data for ***E*-NMe$_2$CNF$_2$** & ***Z*-NMe$_2$CNF$_2$** were collected using a Bruker D8 Venture APEX 3 diffractometer equipped with a CCD area detector and MoKα radiation (λ = 0.71069 Å). The SAINT program (version 8.38A) was used for data reduction, and XPREP (within the APEX 3 suite, version 2017.3–0) ensured structural agreement. Absorption corrections were performed with SADABS, and the structures were solved using SHELXT (version 2018/2) and refined with SHELXL-2014. Non-hydrogen atoms were refined anisotropically, while hydrogen atoms were calculated and refined isotropically.

4.2.2 Synthesis & Characterizations:

A 100 mL round-bottom flask equipped with a magnetic stirrer and reflux condenser was charged with 3,5-difluorobenzylcyanide (0.153 g, 1×10^{-3} mole), 4-dimethylaminobenzaldehyde (0.149 g, 1×10^{-3} mole) in 30 mL (MeOH : THF = 25 :5) solution. Potassium tert-butoxide (0.148g, 1.313×10^{-3} mole) and tetrabutyl ammonium hydroxide (TBAH, 25 % methanol solution, 1.3627 ml, 1.313×10^{-3} mole) was added to it and the resulting mixture was refluxed at 75 °C for 4 hours. Crystals are obtained from mother liquor which were filtered and washed with methanol and air dried (Yield = 0.202 g, 72 %). ^{1}H NMR (300 MHz, D_6-DMSO, 25°C): **NMe$_2$CNF$_2$** δ (ppm), 7.98 (s, 1H, Ar*H*), 7.90 (d, 2H, J=6 Hz , Ar*H*), 7.40 (d, 2H, J= 6.0 Hz, Ar*H*), 7.22 (m, 1H, C_{sp2}-*H*) ,6.83 (m, 2H, Ar*H*), 3.05 (s, 6H, C_{sp3}-*H*),

^{13}C NMR (75 MHz, D_6-DMSO, 25°C) δ (ppm). 164.58 , 161.53, 152.90, 145.79, 139.42, 132.20, 120.35,119.37 ,112.10,108.16, 103.05, 100.10, 31.45 HRMS: calculated for $C_{17}H_{14}N_2F_2$ is 284.3033 , obtained m/z = 285.1865 (M+H).

The molecule **NMe_2CNF_2** was synthesized by one step Knoevenagel Condensation reaction between with 3,5-difluorobenzylcyanide and 4-dimethylaminobenzaldehyde in good yield (Scheme 1). The compound was characterized by ^{1}H NMR, ^{13}C NMR, and HRMS (Figure 1-3).

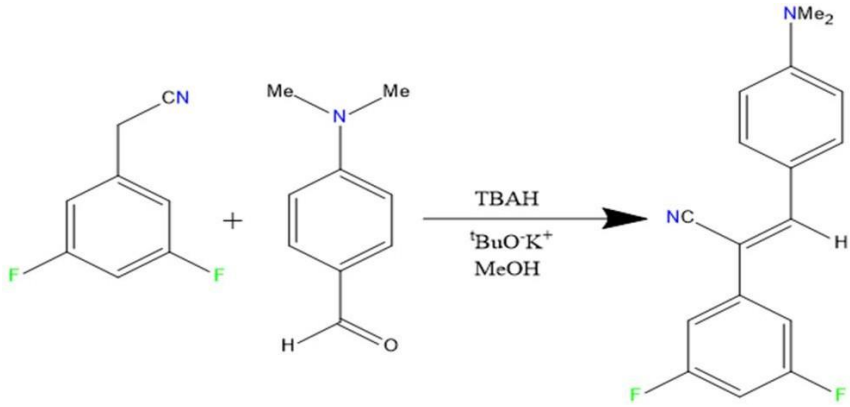

Scheme 1. Synthesis of **NMe_2CNF_2** molecule

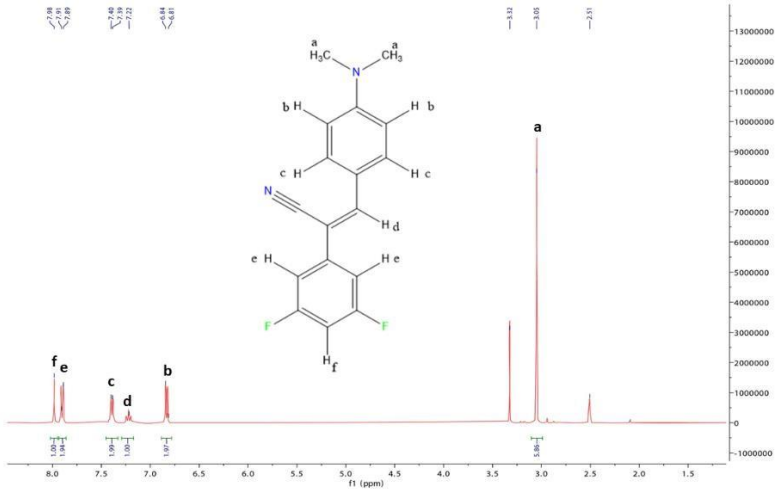

Figure 1. ^{1}H-NMR of as synthesized **NMe_2CNF_2** in $CDCl_3$

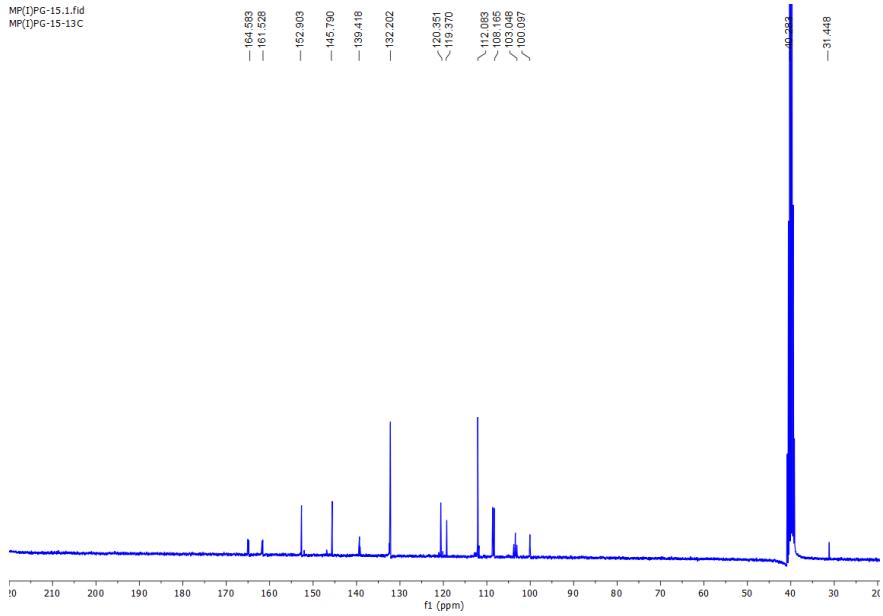

Figure 2. ^{13}C-NMR of as synthesized **NMe$_2$CNF$_2$**

Slow evaporation of the compound from methanol solution provided two different types of crystals, one is long acicular shaped yellow coloured and the other one is acicular shaped red coloured which could possibly be the two isomorphs of the **NMe$_2$CNF$_2$** molecule (Figure 3). In fact, single crystal X-ray diffraction study confirms that the yellow-coloured crystals are *E*-isomer (***E*-NMe$_2$CNF$_2$)** having trans configuration around cyanovinyl double bond C=C(CN), while the red-coloured crystals are *Z*-isomer (***Z*-NMe$_2$CNF$_2$**). Mass spectral analysis of both the crystal confirmed the molecular identity of molecule in both the crystals (Figure 4,5).

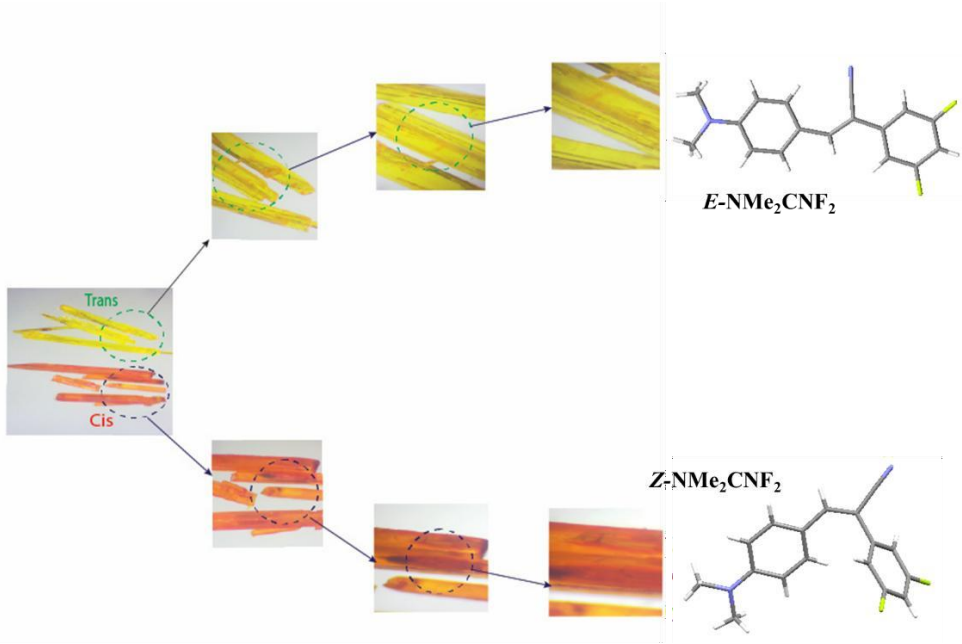

Figure 3. Optical images of the yellow and red coloured crystals of **NMe2CNF2**

4.3. Results and Discussions:

4.3.1 NMR, MASS, PXRD and IR Analysis:

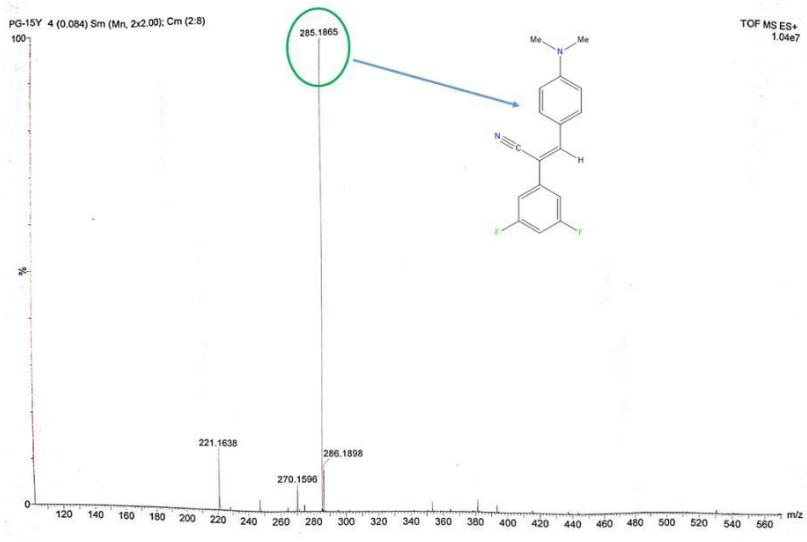

Figure 4. High-resolution mass spectra (HRMS) of compound ***E*-NMe2CNF2** showing [M+H] peak at 285.1865. M= monomer mass (284 g/mol)

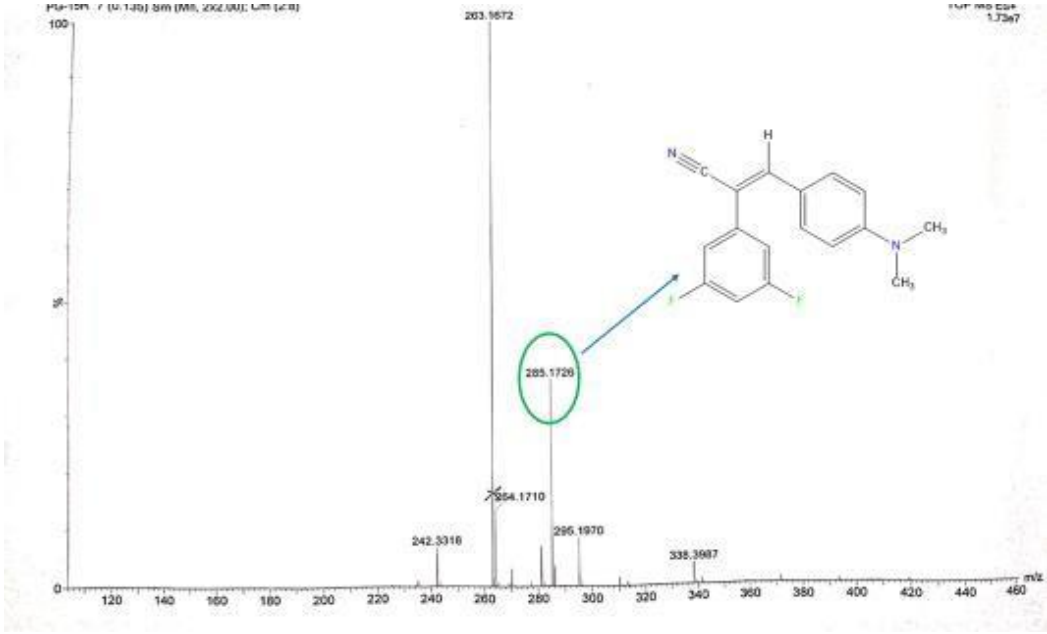

Figure 5. High-resolution mass spectra (HRMS) of compound ***Z*-NMe$_2$CNF$_2$** showing [M+H] peak at 285.1726. M= monomer mass (284 g/mol)

To further verify the effect of geometric configuration on the bond stretching frequency of the isomers, we have carried out IR spectra of the ***E*-NMe$_2$CNF$_2$** and ***Z*-NMe$_2$CNF$_2$**. As can be seen from figure 6, the characteristic $\nu_{C\equiv N}$ bands appear at 2202 cm^{-1} and 2191 cm^{-1} , the $\nu_{C=C}$ bands appear at 1621 cm^{-1} and 1612 cm^{-1} respectively for *E*- and *Z*-isomers, thereby confirming the formation of the geometric isomers.

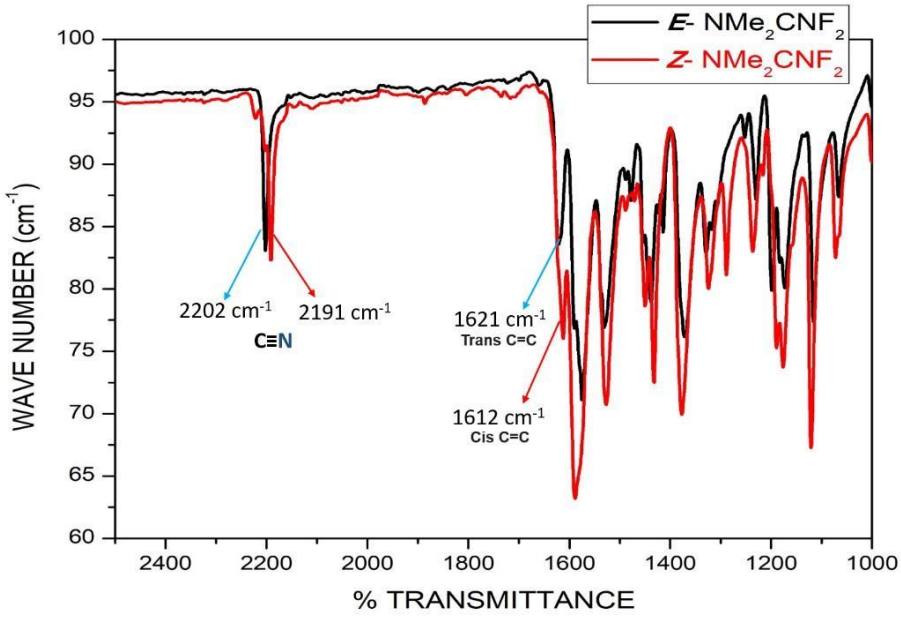

Figure 6. IR spectra of the *E*- (black lines) and *Z*- (red lines) isomers

4.3.2 Photophysical Characterization and Solis State Fluorescence:

UV Vis spectra (in THF, 1 x 10^{-5} M) of the compound in ***E*-NMe$_2$CNF$_2$** display a broad absorption band with a λ_{max} = 411 nm which could be attributed to intramolecular charge transfer transition (Figure 7). On the contrary the ***Z*-NMe$_2$CNF$_2$** display a blue shifted ICT absorption band having λ_{max} = 378 nm. Frontier molecular orbital analysis by our DFT study suggests that for both the isomers, HOMO's are located mainly on donor -NMe_2 fragment while the LUMO's are located on -CN or PhF_2 groups (Figure 8). HOMO-LUMO gap for the ***Z*-NMe$_2$CNF$_2$** is higher (3.5930 e.v) compared to ***E*-NMe$_2$CNF$_2$** (3.440 ev) corroborates well with the experimental UV-Vis spectra of the two isomers.

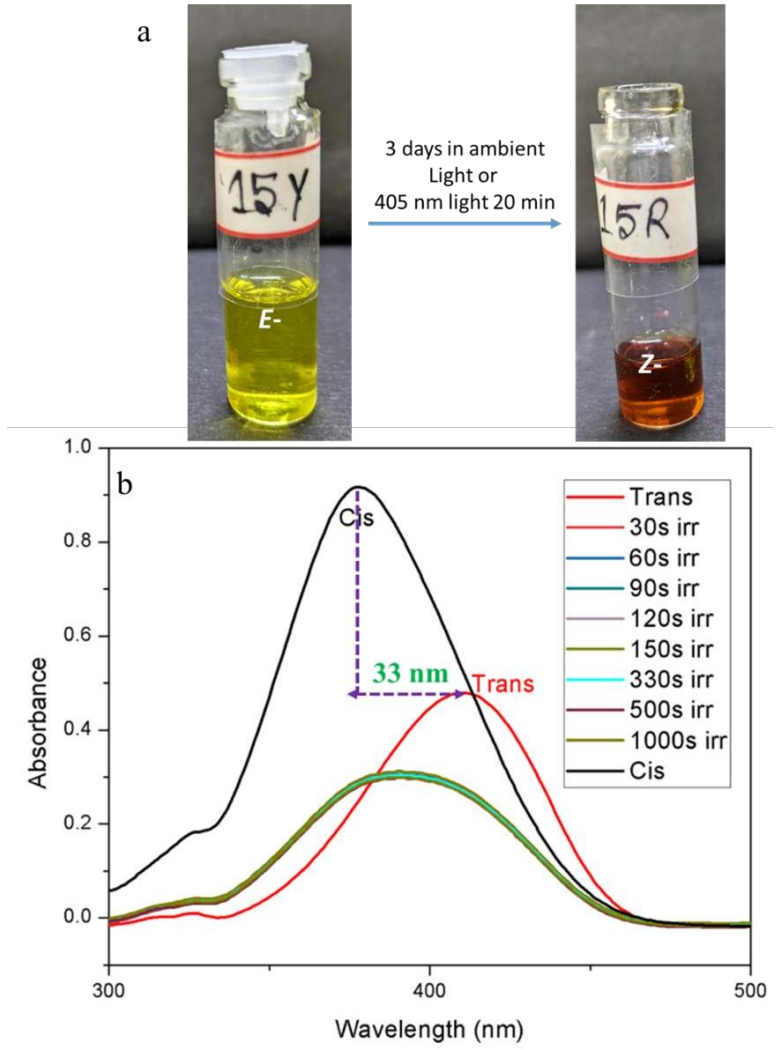

Figure 7. Solution state absorption plot of **NMe$_2$CNF$_2$** in **THF** solvent. Pure ***Z*-** NMe_2CNF_2 shows absorption maxima at 378 nm and pure ***E*- NMe$_2$CNF$_2$** shows absorption maxima at 411 nm in solution state. Illumination of the THF solution of ***E*- NMe$_2$CNF$_2$** led to the blue-shifting of absorption maxima.

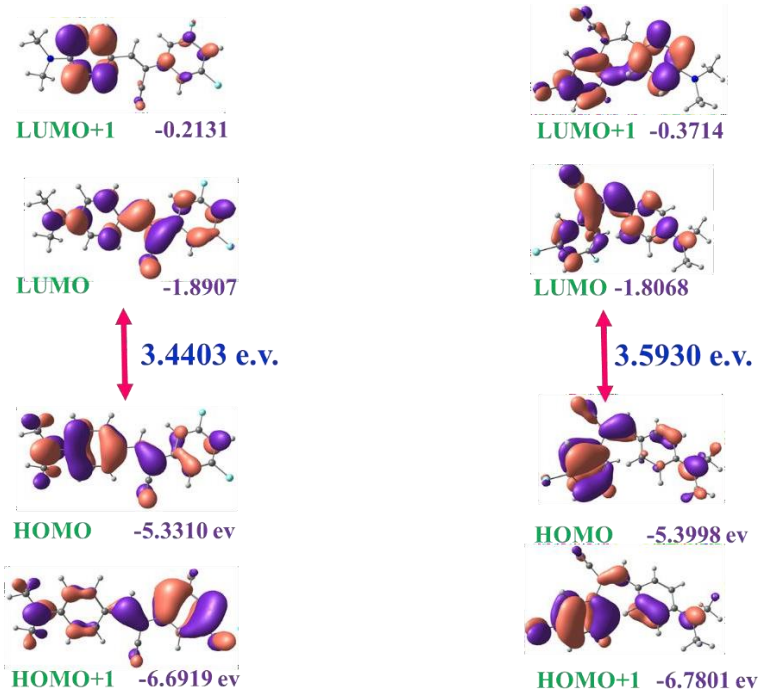

Figure 8. DFT calculated frontier molecular orbitals of ***E*-NMe$_2$CNF$_2$** and ***Z*-NMe$_2$CNF$_2$**.

Interestingly, Both *E*- and *Z*-isomers are non-fluorescent in solution state, however, brightly emissive in solid state. As displayed in Figure 9, the crystals of ***E*-NMe$_2$CNF$_2$** is green fluorescent under UV light while the corresponding *Z*-isomer crystal is orange-red fluorescent. High fluorescence in solid crystalline state while non-fluorescence in solution state can be ascribed to the crystallization induced emission enhancement (CIEE) behaviour of both the isomers.

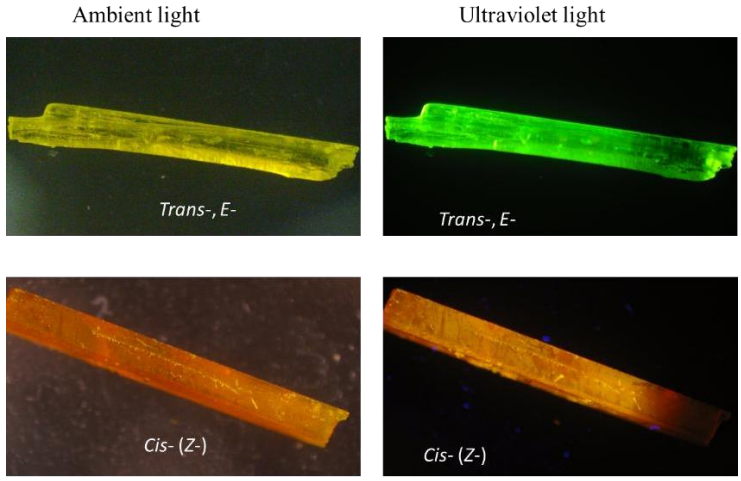

Figure 9. Solid state fluorescence of ***E*-** and ***Z*-**isomers of **NMe$_2$CNF$_2$**

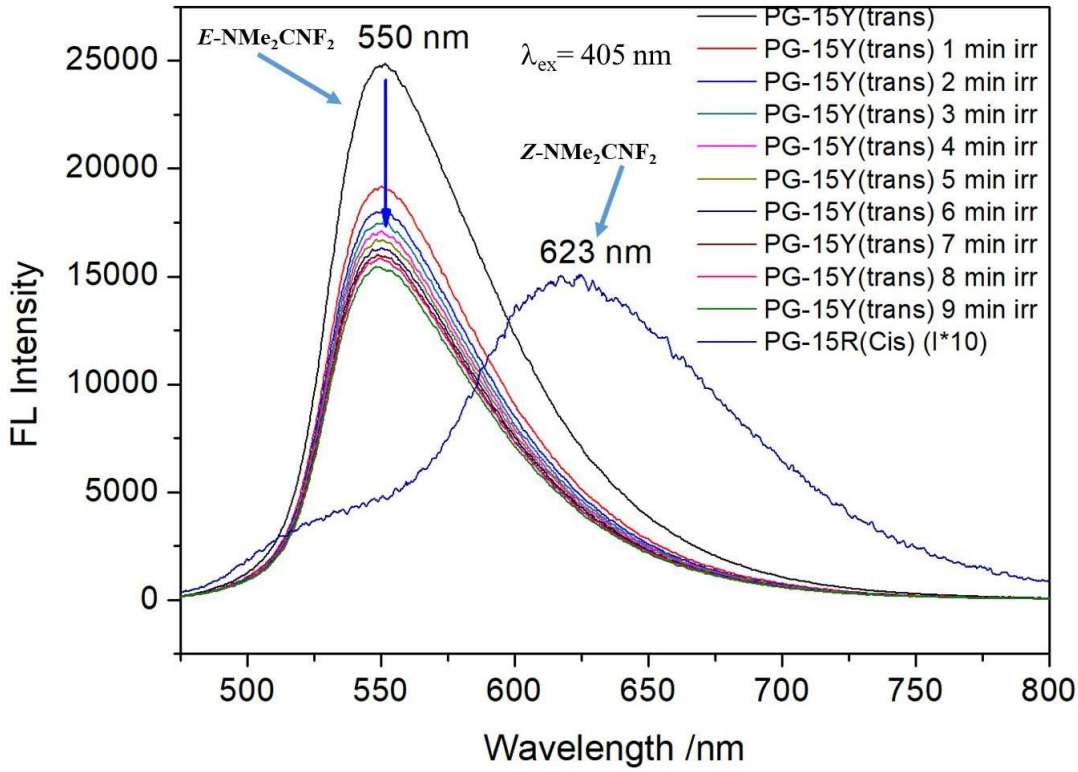

Figure 10. Solid state fluorescence spectra of ***E***- and ***Z***-isomers of **NMe_2CNF_2**

Solid state fluorescence spectra of ***E*-NMe_2CNF_2** isomer exhibit an emission band peaking at λ_{max} = 550 nm correspond to green emission of the crystal while the ***Z*-NMe_2CNF_2** isomer crystal display much red shifted emission band peaking at λ_{max} = 623 nm signifying orange-red emission of the cis isomer. As expected, the fluorescence intensity of the *E*-isomer crystal is much higher compared to the *Z*-isomer crystals. As discussed earlier, when illuminated with 405 nm light, the solution of the ***E*-NMe_2CNF_2** isomer slowly transformed into ***Z*-NMe_2CNF_2** isomer, however same switching is not observed in solid state. As observed from the figure 10, illumination of solid crystals of ***E*-NMe_2CNF_2** isomer do not transform to ***Z*-NMe_2CNF_2** isomer except hypochromic shift of the fluorescence.

4.3.3 Single Crystal X-ray Structure: Slow evaporation of solvent led to the growth of long acicular single crystals of ***E*-NMe_2CNF_2**. The X-ray crystallographic data unveiled that the *E*-isomer have crystallized adopting a planer geometry in conformity with the DFT geometry optimized structure. Scrutinizing the two regioisomers i.e. ***E*- NMe_2CNF_2** and ***Z*-NMe_2CNF_2**, it can be addressed that the *E*-isomer is possessing greater planarity between the benzaldehyde ring and the olefinic bond.

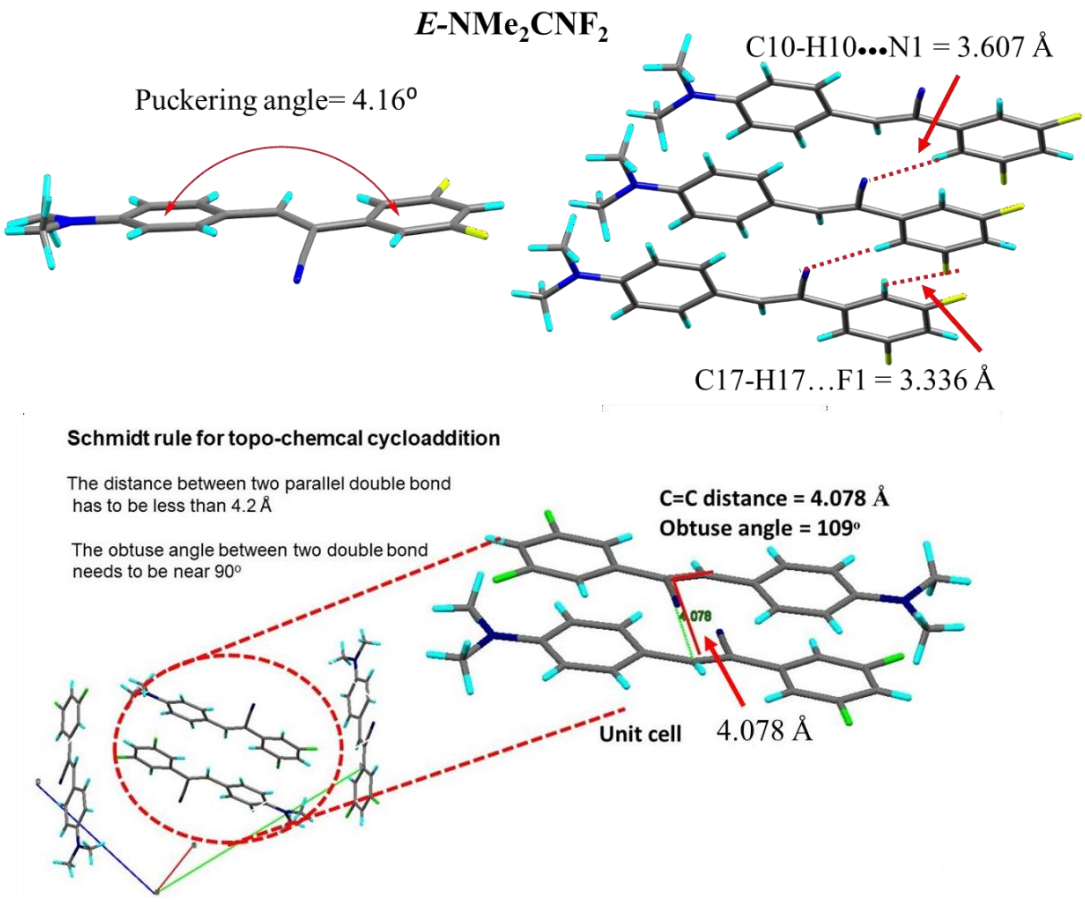

Figure 11. Conformational analysis of ***E*-NMe$_2$CNF$_2$** and ***Z*-NMe$_2$CNF$_2$** in the respective crystal lattice showing puckering of the terminal phenyl rings in two isomers.

Solid-state luminescence properties of the ***E*-NMe$_2$CNF$_2$** and ***Z*-NMe$_2$CNF$_2$** crystals greatly depend on their molecular conformation, packing and non-covalent interactions. To highlight the structural features that could be responsible for difference in the luminescence behavior of the two isomers, we have determined the X-ray structures and analyzed their structural features. ***E*-NMe$_2$CNF$_2$** crystallized from MeOH: DMSO (5:1) mixture in a monoclinic system having $P2_1$ space group (cell parameters: a = 7.0345(2) Å, b = 18.4945(5) Å, c = 11.5223(3) Å, α = γ = 90°, β = 106.9350(10)°, (see Table 1). Conformational analysis reveals that the terminal aromatic rings of the ***E*-NMe$_2$CNF$_2$** molecule are nearly coplanar (4.16°, Figure 11). This planar conformation of the molecule enables better conjugation as well as effective electronic communication within the molecule which is responsible for its bright green fluorescence in solid state. Moreover, The molecules are connected by several intermolecular intermolecular H-bonding interactions (C10-H10•••N1 = 3.607 Å, D•••A distance, <DHA = 173.75º, C17-H17…F1 = 3.336 Å, <DHA = 132.16º). These intermolecular interactions tie the molecules in the crystal lattice and restrict non-radiative decay thereby enhancing the emission in solid state

which is responsible for bright green fluorescence of ***E*-NMe$_2$CNF$_2$** crystal. Another important feature that can be extracted from the crystal structure is the stacking of the cyanovinyl C=C double bonds within Schmidt's distance (d = 4.078 Å) which is indicative of possible photo-reactivity for [2+2] cycloaddition reactions. The packing diagram of ***E*-NMe$_2$CNF$_2$** crystal is shown in figure 12 reveals that the molecules are arranged in herringbone pattern (viewed along *a*-axis) in the lattice.

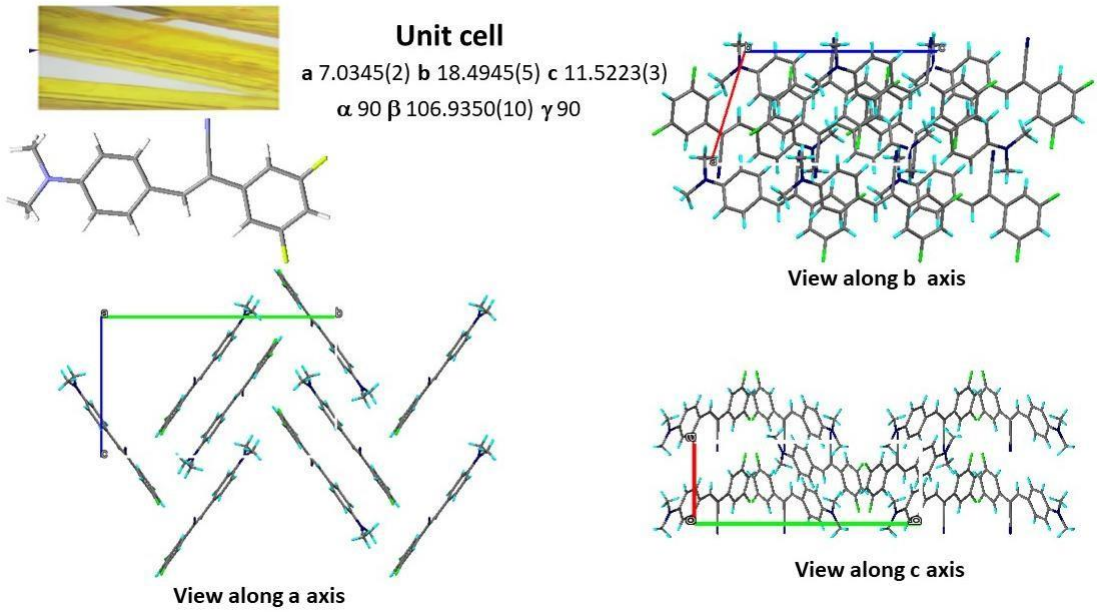

Figure 12. Packing diagram of ***E*- NMe$_2$CNF$_2$** crystal view along all axis.

Table 1. Single crystal X-ray parameters of ***E*- NMe$_2$CNF$_2$** and ***Z*- NMe$_2$CNF$_2$** at 273 K.

	***E*- NMe$_2$CNF$_2$**	***Z*- NMe$_2$CNF$_2$**
CCDC No.	2299147	2299146
Chemical formula	$C_{17}H_{14}F_2N_2$	$C_{17}H_{14}F_2N_2$
M_r	284	284
Crystal system	Monoclinic	Monoclinic
Space group	P $2_1/c$	P $2_1/c$
a / Å	7.0345(2)	11.8580(3)
b / Å	18.4945(5)	13.6014(4)
c / Å	11.5223(3)	9.0074(2)
α/°	90	90
β/°	106.9350(10)	93.9700(10)
γ/°	90	90
V / Å^3	1434.04(7)	1449.28(7)

Z	4	4
ρ_{calc} / (g cm^{-3})	1.284	1.298
μ / mm^{-1}	0.085	0.089
F_{000}	580	592
θ_{min} / °	2.88	2.717
θ_{max} / °	27.12	27.114
Reflections collected	3133	3175
Independent reflections	2677	2612
GoF	1.050	1.033
Final *R* indices [$I > 2\sigma(I)$]	R_1 = 0.0754, wR_2 = 0.2050	R_1 = 0.0567, wR_2 = 0.1646
R indices (all data)	R_2 = 0.0835, wR_2 = 0.1938	R_2 = 0.0665, wR_2 = 0.1516

Single crystals of ***Z*-NMe$_2$CNF$_2$** were obtained from the same solvent mixture from which *E*-isomer was crystallized. The crude product of PG-15 was dissolved in a MeOH : DMSO (5:1) mixture. The resulting solution was exposed to 9-watt white light for 12 hours. During this period, the solution colour gradually changed from yellow to red, indicating photo induced *trans-to-cis* isomerization. Red-coloured needle-shaped crystals of the *cis* isomer formed during this process and were isolated by filtration. ***Z*-NMe$_2$CNF$_2$** crystallizes in monoclinic crystal system with P2$_1$/*c* space group having unit cell parameters cell parameters: *a* = 11.8580(3) Å, *b* = 13.6014(4) Å, c = 9.0074(2) Å, α = γ = 90°, β = 93.9700(10). As can be

In contrary to *E*-isomer, the molecule in the ***Z*-NMe$_2$CNF$_2$** crystal is not planner, rather it has twisted geometry having dihedral angle of 68.85º between terminal phenyl planes. The molecules are connected to each other by C–H•••π interaction between phenyl hydrogen and neighbouring π -cloud of the benzene ring (Figure 13). To get more insight into the intermolecular interactions and the interaction energy we have done detailed study using Crystal explorer software which is discussed below.

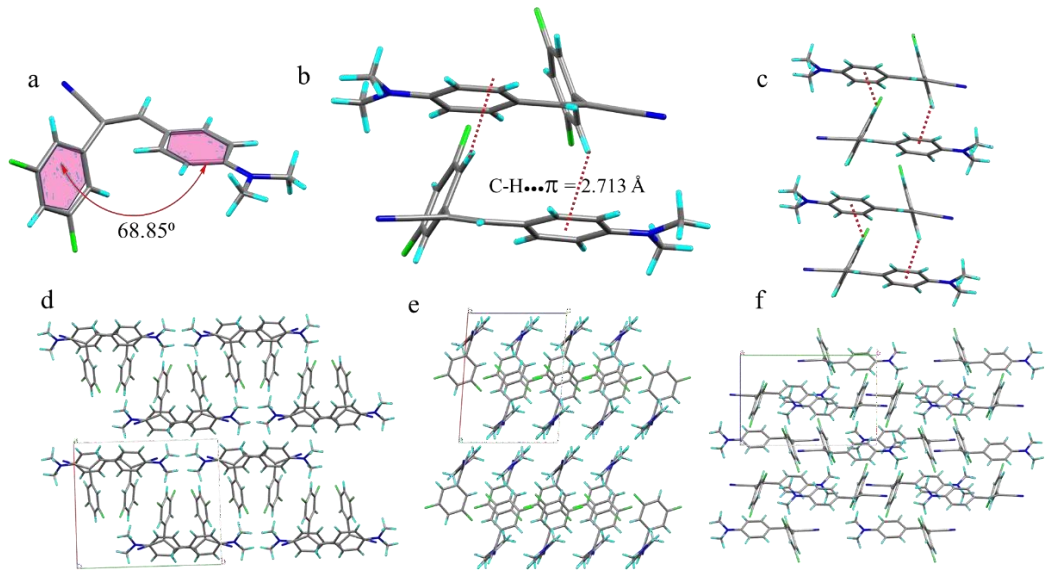

Figure 13. Structural information of ***Z*-NMe$_2$CNF$_2$** crystal. (a) molecular conformation and puckering angle; (b,c) C-H…π interactions and extended network; (d, e, f) packing of the molecules along different crystallographic axis.

4.3.4 Photo-responsive behaviour in solid and solution state:

As anticipated earlier in the discussion of X-ray structure that the molecules in the *E*-isomers stack within Schmidt's distance which is favourable for topochemical [2+2] cycloaddition reaction. We wanted to see the effect of isomeric structure on the photoresponsivity of the *E*- and *Z*- crystals under UV or visible light illumination. Indeed, a *E*- and *Z*-isomer respond to 405 nm light in very different way. While ***E*-NMe$_2$CNF$_2$** crystals display fascinating photo-mechanical actuating behaviour when illuminated with 405 nm light, ***Z*-NMe$_2$CNF$_2$** crystals are surprisingly silent even though the molecular identity and photoactive functionality is same in both the cases. This phenomenon conclude that solid state photo reactivity is highly dependent on the packing structure of the material. As can be seen from figure 14, long acicular shaped crystals of ***E*-NMe$_2$CNF$_2$** bend, jump, splits, roll when illuminated by 405 nm light, but no significant shape change or actuation is observed in the Z-isomer crystal.

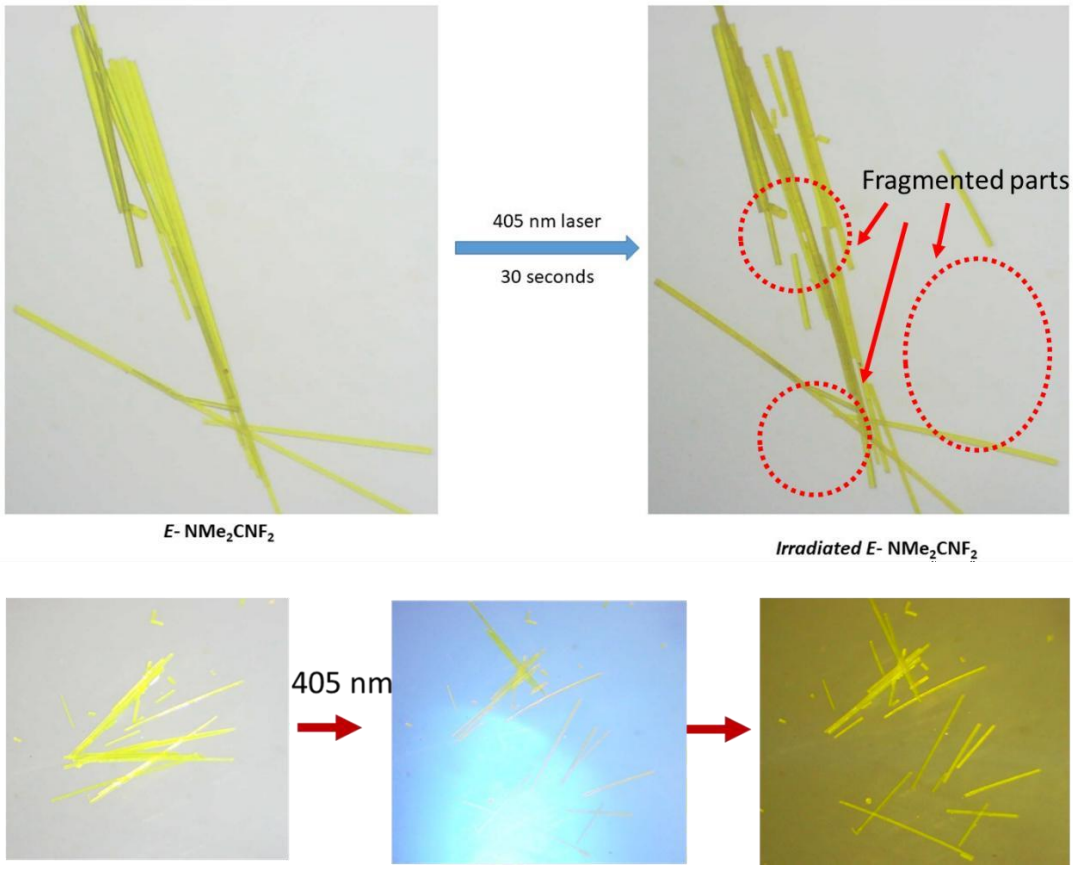

Figure 14. Photomechanical actuation, splitting of ***E*-NMe$_2$CNF$_2$** crystals under 405 nm light illumination.

Interestingly, the photo reactivity of the *E*-isomer in solution state and solid state are drastically different. Do verify the solution state reactivity we have irradiated the $CDCl_3$ solution of ***E*-NMe$_2$CNF$_2$** and recorded the ^{1}H NMR spectra in different time interval of the photoirradiation. The result is shown in Figure 15 below. In case of solid state photoreactiveity, we have irradiated the crystals with 405 nm light for different time intervals and then dissolven in $CDCl_3$ to record the ^{1}H NMR spectra at the respective time. As can be seen from time dependent ^{1}H NMR spectra (Figure 15-16), ***E*-NMe$_2$CNF$_2$** undergo only isomerization in the solution while in the solid state both the isomerization and [2+2] cycloaddition product is forming. The actuation in solid state is rooted to both isomerization and cycloaddition reaction that generates a bimorphic stress in solid state that are released in the form of actuation. In solution state, molecules are diluted and thus do not meet the Schmidt's criteria for cycloaddition reaction and as a result only *E*- to *Z*- isomerization occurs. To understand the details of conversion and mechanism we have carried out several NMR study. Photoconversion of the *E*-isomer to the *Z*- one was carried out irradiating the *E*-regioisomer with ambient light for straight 70 hours in

solution state (Figure 15). The photoconversion was responsible to 405 nm light irradiation as well. Crystallization of the photoconverted solution led us to the synthesis of the *Z*-isomer.

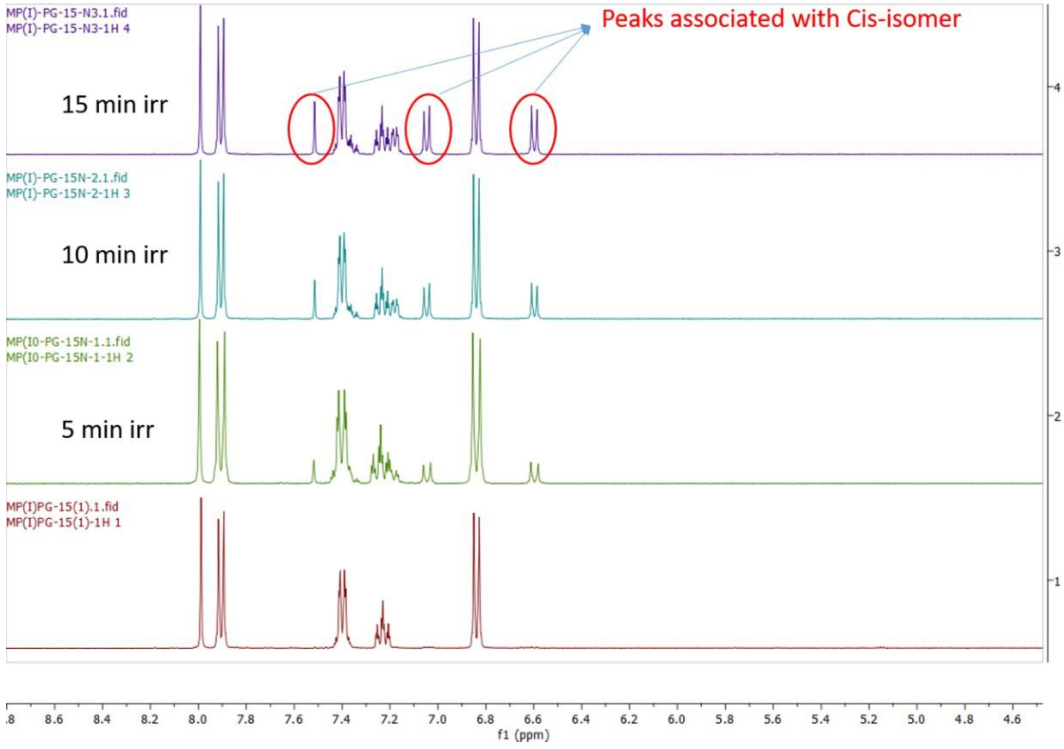

Figure 15. Time dependent Solution state NMR spectroscopy of ***E*- NMe_2CNF_2** in D_6-DMSO solvent. In this time dependent solution state NMR study, we observed ***E*- NMe_2CNF_2** to ***Z*- NMe_2CNF_2** geometrical isomerization takes place in solution state. For this nmr study 405 nm light is used.

In solid state, irradiation of the *E*- isomer crystals under 405 nm visible light for about 3 hours led to the formation of mixture of photo-converted products comprising of a certain portion of *Z*-isomeric molecules and a certain portion of molecules underwent dimerization as can be deduced from Figure16 unveiling the peaks of cis-isomer as well as peaks associated to dimerization. Schmidt's criteria of photo dimerization asserts that for any molecules to undergo [2+2] cycloaddition, the intermolecular distance between the double bonds of the two molecules should be oriented parallel to each other with a centroid distance of 3.5Å-4.2Å. And for the E-isomer, crystal packing structure provides the evidence of possessing a centroid distance of 4.082Å between the two parallel molecules which clarifies the obvious reason for the molecules to undergo dimerization upon irradiation. The formation of [2+2] cycloaddition product was further confirmed by mass spectral analysis (Figure 17). Time dependent PXRD analysis (Figure 18) of the photo conversion of the *E*-isomer confirms the formation of new

products. Several new peaks associated with lattice structure rearrangement and shifted peak position upon irradiation with 405 nm light is supporting the observation from NMR and lass spectra.

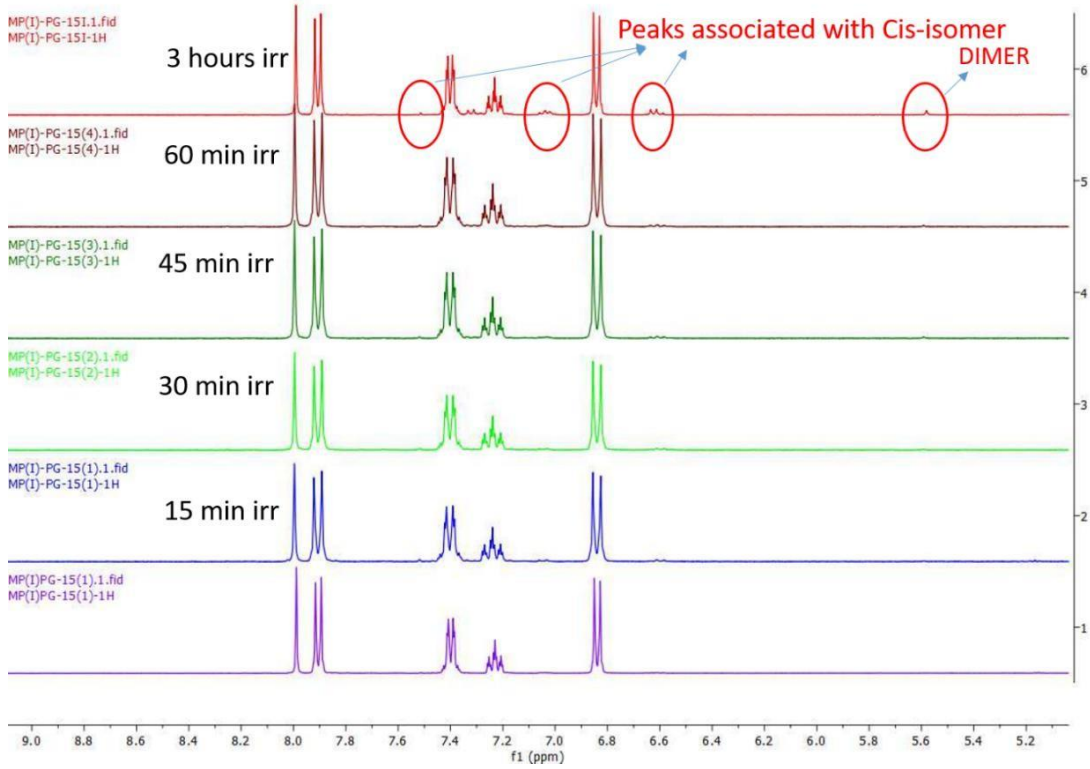

Figure 16. Time dependent solid state irradiated NMR spectroscopy of ***E*- NMe_2CNF_2** in D_6-DMSO solvent. In this time dependent solid state irradiated NMR study, we observed ***E*- NMe_2CNF_2** to ***Z*- NMe_2CNF_2** geometrical isomerization and dimerization both takes place simultaneously. 405 nm light was used for illumination.

The phenomena of photoconversion of *trans* to *cis* isomer is irreversible, allowing only the conformational change from *E*- to *Z*- isomer. As discussed earlier in the crystal structure analysis that this process is highly reliant on the packing form of the crystal lattice structure. Photo-induced isomerization takes place within that lattice structure where the consisting molecules lacks effective packing of their backbones which corresponds to the fact that sufficient amount of void space is required for undergoing efficient isomerization in solid state. The crystal packing structure of *E*-isomer elucidates that the molecules within the crystal lattice are aligned orthogonal to each other which is symbolic to less effective packing of the molecules in crystalline backbones thereby demonstrating a plausible reason behind the photo isomerization of the *trans* to cis isomer. Consequently, the densely packed lattice structure of

the *Z*-isomer completely blocks the photo conversion for possessing minimum amount of void space and effective overlap within the crystal lattice structure.

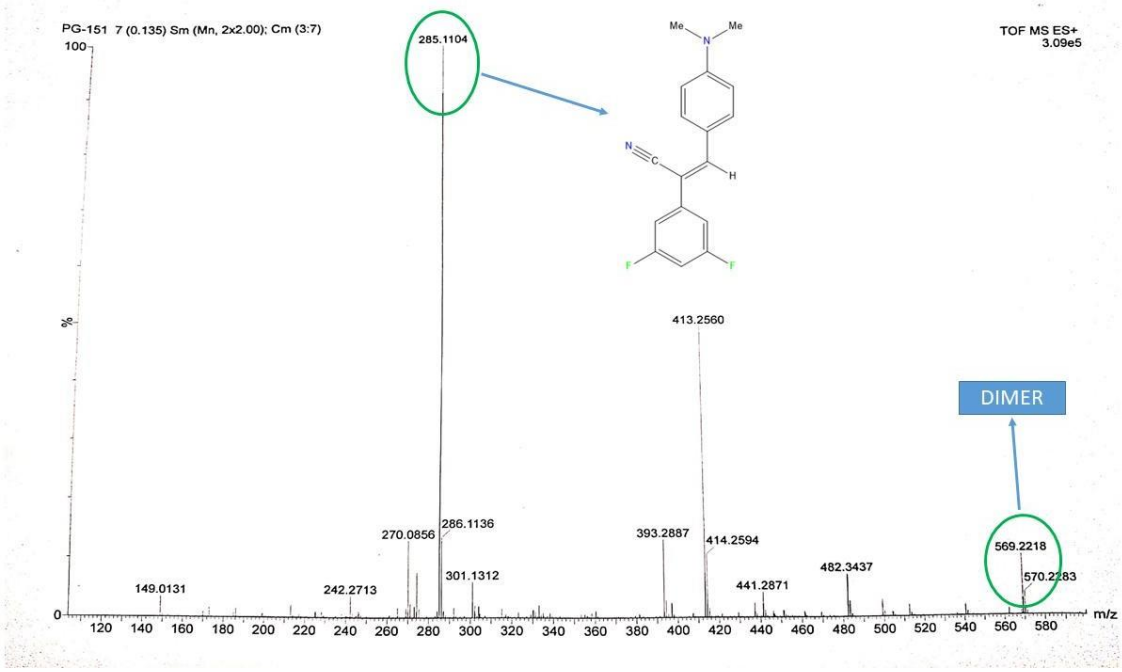

Figure 17. High-resolution mass spectra (HRMS) of **NMe_2CNF_2** after irradiation by 405 nm laser. [2M+H] peak is observed at 569.2218 which confirms the formation of [2+2] dimer product upon photoirradiation.

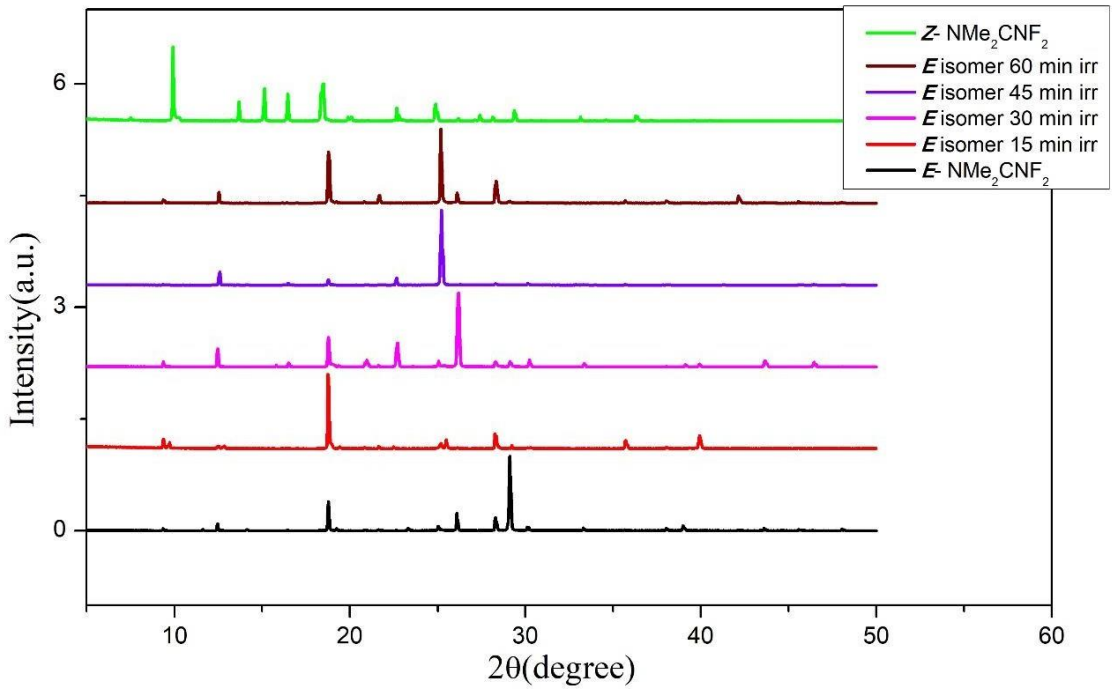

Figure 18. Stack PXRD of ***Z*-NMe2CNF2** and irradiated ***E*-NMe2CNF2** in different time scale.

4.4 Hirshfield surface Analysis:

The Hirshfield surface Analysis which pen picturises the molecular surface analysis was carried out in order to comprehend the intermolecular interactions those are accountable for the molecular packing within in the geometric isomers. The surface analysis was generated with the help of Crystal Explorer17 software''. The Hirshfield surface was mapped with respect to the d_{norm} and the resulting plots are provided below. d_{norm} is the measure of normalised contact distance and can be expressed in the following form of equation:

$$d_{norm} = \left[\frac{d_i - r_i^{vdw}}{r_i^{vdw}}\right] + \left[\frac{(d_e - r_e^{vdw})}{r_e^{vdw}}\right]$$

where d_i and d_e symbolises the distance from each point of the surface of the respective conformationally different molecules to the nearest nuclei external and internal to the surface respectively. Depending on the note that whether the intermolecular contacts are longer or shorter than the van der Waals radii, the value of the d_{norm} may vary from negative to positive. Red surface indicates the region where atoms are making intermolecular contacts shorter that

sum of their van der Waals radii that generating a negative d_{norm} value. In the similar way the blue and white surface indicates the region that's forming interaction greater and almost neutral than the van der Waals radii thereby with a positive and zero d_{norm} values respectively.

The 2D fingerprint plots of the ***E*-NMe$_2$CNF$_2$** & ***Z*-NMe$_2$CNF$_2$** crystals (Figure 19 & 20) were derived in the d_{norm} ranging from 0.6 to 2.8 Å. These plots provide information regarding the prevailing intermolecular interactions along with the relative area of surface corresponding to each kind of existing interactions from Fragment Patch diagrams (Figure 19b, 20b). The percentage wise various kinds of interactions present like **H…H, C…H, C..,F…H, N…H** for the conformationally different three isomers is provided below in schematic form. It's evident from the figure and calculated data that a remarkable amount of H bonding interaction is present in the ***E*-NMe$_2$CNF$_2$** crystal which plays a crucial role in the stabilization of lattice and packing reconfiguration resulting in attaining planarity of the molecular crystals. The shape index figures (Fig. 19b) give a rough sketch of the quantitative measure of shape of the respective crystals where hollow regions (concave) marked by yellow region represent the region having shape index < 1 and the bumps (convex) with blue regions symbolises the surface with shape index > 1.

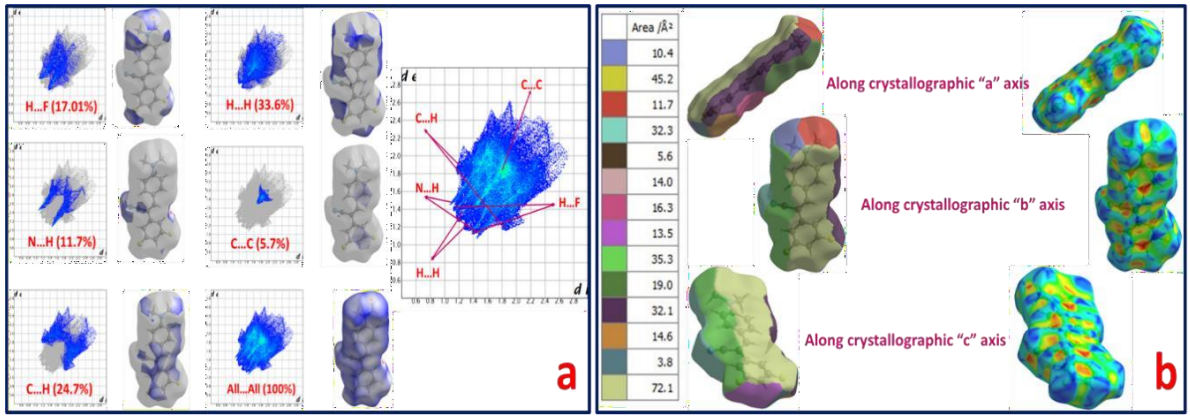

Figure 19. (a) Fingerprint plots and Hirshfield surface area **(d_{norm})** of each of the major interactions in ***E*- NMe$_2$CNF$_2$** Molecule**. (b)**Fragment Patch area and Shape Index of Trans crystal in all the three axial directions

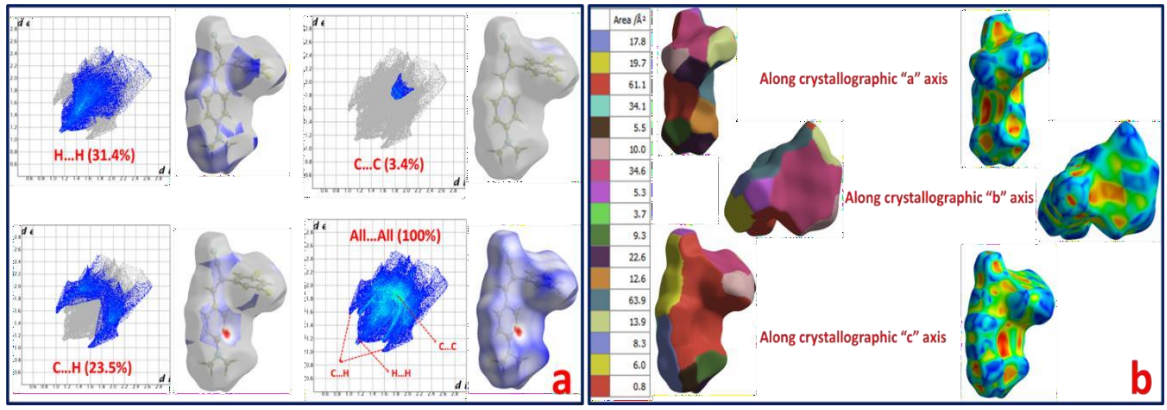

Figure 20. (a) Fingerprint plots and Hirshfield surface area **(d_{norm})** of each of the major interactions in ***Z*- NMe_2CNF_2** Molecule**. (b)**Fragment Patch area and Shape Index of Cis crystal in all the three axial directions

4.5 Energy Framework calculations:

In order to understand the various intermolecular interaction energies, present in the two positional Isomers crystal lattice, we took the help of Crystal Explorer17 software to undergo the energy framework calculations. The molecular wave function B3LYP/6-31G (d,p) was utilized in order to run the DFT calculations. The total intermolecular energy (E_{tot}) that's derived from the energy framework calculation was calculated to be -11.74 kJ/mol, -47.11 kJ/mol & -60.78 kJ/mol for ***E*- NMe_2CNF_2** crystal & -55.84 kJ/mol, -31.66 kJ/mol and -32.11 kJ/mol for the ***Z*- NMe_2CNF_2**.(Figure 20 & 21, Table 2-5). Whereas the dispersive energy ($E_{dispersive}$) was calculated to be -12.37 kJ/mol, -40.65 kJ/mol & -72.90 kJ/mol for the *E*-isomer and the same measuring -51.72 kJ/mol, -35.98 kJ/mol and -32.33 kJ/mol for the *Z*-isomer. The total amount of energy generating due to charge separation i.e. coulomb energy ($E_{coulombic}$) in the molecule was found to be -13.35 kJ/mol, -4.94 kJ/mol & -16.35 kJ/mol for *E*-isomer and -12.01 kJ/mol, -22.79 kJ/mol and -8.11 kJ/mol for the *Z*-isomer respectively. Which is significantly lower than the dispersive energy. The pair wise interaction energies of the molecules in lattice are also provided below as calculated. The interaction energy calculations indicates that the interaction energy within the crystal lattice structure of *Z*-conformation is more viable than that of the *E*-form which could be a plausible reason behind the irreversibility of photo isomerization.

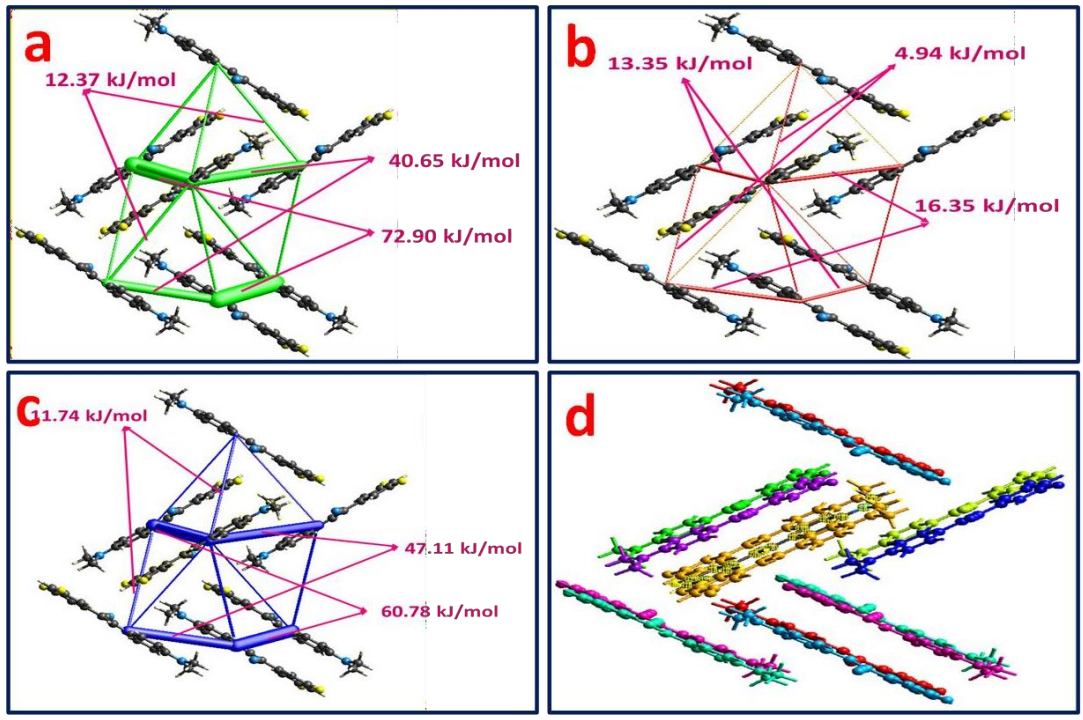

Figure 21. Energy Framework calculations, **(a)** $E_{coulombic}$ **(b)** $E_{dispersive}$ **(c)** E_{total} **(d)** Interaction Energy; for PG-15Y Crystal

E- NMe_2CNF_2 -Pair-wise Interaction Energy:

Table 2. Interaction Energies (kJ/mol) R is the distance between molecular centroids (mean atomic position) in Å.*, **

N	Symop	R	Electron Density	E_ele	E_pol	E_dis	E_rep	E_tot
2	-x, y+1/2, -z+1/2	10.45	B3LYP/6-31G(d,p)	-4.5	-0.8	-10.1	3.8	-11.7
2	x, y, z	7.03	B3LYP/6-31G(d,p)	-11.0	-5.4	-22.1	18.9	-23.2
1	-x, -y, -z	9.71	B3LYP/6-31G(d,p)	-15.5	-3.8	-46.7	20.6	-47.1
1	-x, -y, -z	5.87	B3LYP/6-31G(d,p)	-5.3	-2.5	-29.9	10.7	-26.9
2	x, -y+1/2, z+1/2	10.06	B3LYP/6-31G(d,p)	-1.7	-1.0	-5.1	1.8	-5.9
2	-x, y+1/2, -z+1/2	10.67	B3LYP/6-31G(d,p)	-4.7	-0.7	-11.2	6.3	-11.3
1	-x, -y, -z	11.08	B3LYP/6-31G(d,p)	-0.8	-1.3	-16.9	10.9	-9.8
1	-x, -y, -z	3.96	B3LYP/6-31G(d,p)	-12.6	-2.0	-83.7	43.7	-60.8
2	x, -y+1/2, z+1/2	8.68	B3LYP/6-31G(d,p)	2.7	-0.7	-14.2	4.3	-7.4

*Scale factors for benchmarked energy models

**See Mackenzie et al. IUCrJ (2017)

Table 3. Total energies, only reported for two benchmarked energy models, are the sum of the four energy components, scaled appropriately

Energy Model	k_ele	k_pol	k_disp	k_rep
CE-HF ... HF/3-21G electron densities	1.019	0.651	0.901	0.811
CE-B3LYP ... B3LYP/6-31G(d,p) electron densities	1.057	0.740	0.871	0.618

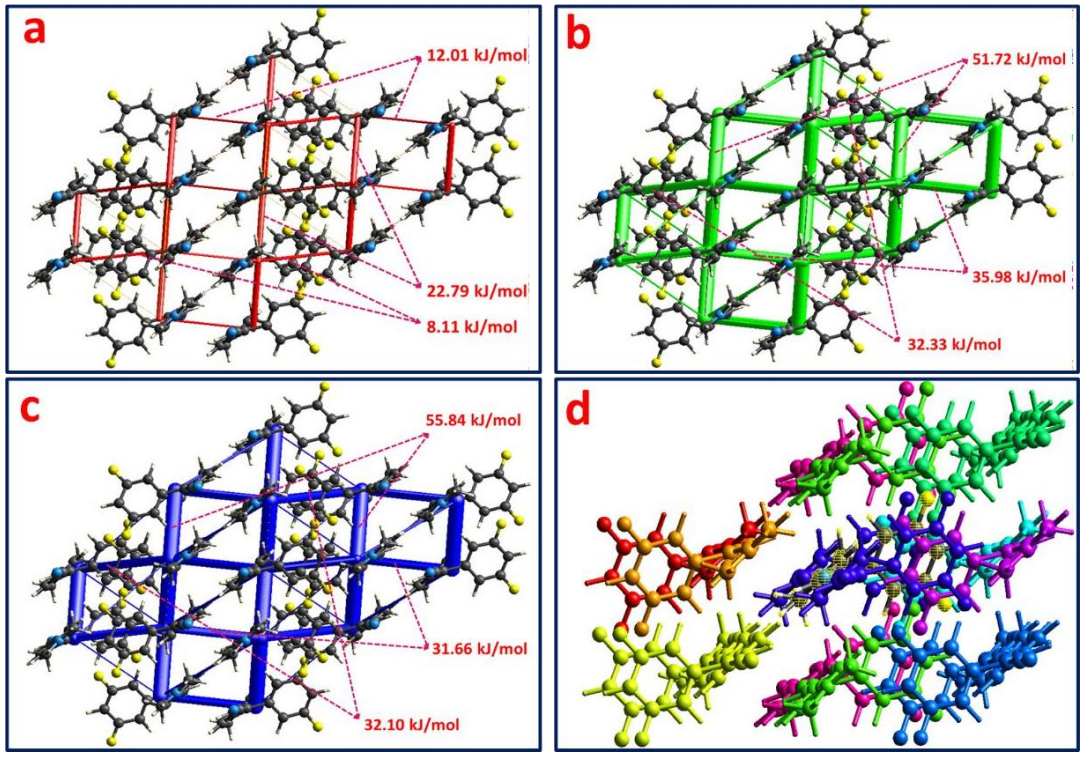

Figure 22. Energy Framework calculations: **(a)** $E_{coulombic}$ **(b)** $E_{dispersive}$ **(c)** E_{total} **(d)** Interaction Energy for ***Z*- NMe_2CNF_2** Crystal

***Z*- NMe_2CNF_2 -Pair-wise Interaction Energy:**

Table 4. Interaction Energies (kJ/mol),R is the distance between molecular centroids (mean atomic position) in Å.*, **

	N	Symop	R	Electron Density	E_ele	E_pol	E_dis	E_rep	E_tot
	1	-x, -y, -z	9.41	B3LYP/6-31G(d,p)	-7.7	-2.0	-41.3	22.5	-31.7
	1	-x, -y, -z	9.88	B3LYP/6-31G(d,p)	-6.4	-3.6	-8.5	3.7	-14.5
	2	-x, y+1/2, -z+1/2	10.64	B3LYP/6-31G(d,p)	-0.9	-2.6	-14.7	8.8	-10.3
	2	x, -y+1/2, z+1/2	4.52	B3LYP/6-31G(d,p)	-21.6	-3.8	-59.4	34.8	-55.8

	2	-x, y+1/2, -z+1/2	9.98	B3LYP/6-31G(d,p)	0.3	-0.5	-6.6	1.6	-4.9
	1	-x, -y, -z	8.22	B3LYP/6-31G(d,p)	-2.0	-1.4	-18.6	8.7	-14.0
	2	-x, y+1/2, -z+1/2	9.21	B3LYP/6-31G(d,p)	1.1	-0.5	-7.1	0.8	-4.9
	2	x, y, z	13.60	B3LYP/6-31G(d,p)	-12.1	-2.6	-4.1	3.6	-16.0
	1	-x, -y, -z	8.75	B3LYP/6-31G(d,p)	-11.4	-1.9	-37.1	22.1	-32.1
	2	x, -y+1/2, z+1/2	14.01	B3LYP/6-31G(d,p)	3.6	-0.6	-4.1	0.9	0.3

Table 5. Total energies, only reported for two benchmarked energy models, are the sum of the four energy components, scaled appropriately

Energy Model	k_ele	k_pol	k_disp	k_rep
CE-HF ... HF/3-21G electron densities	1.019	0.651	0.901	0.811
CE-B3LYP ... B3LYP/6-31G(d,p) electron densities	1.057	0.740	0.871	0.618

To understand the effect of steric crowding in the *Z*-isomer, we have carried out Non-Covalent Interaction (NCI) Plots. The analysis reveals that in *Z*-isomer minimal number of steric clashes between the protons of the two benzene rings around the olefinic bond. Furthermore, in case of the z-isomer, the de-planarity and its deviation from the ideal bond angle is attributed to the greater number of steric clashes in its crystal lattice structure as also confirmed from the Non-Covalent Interaction (NCI) Plots (Figure.23).

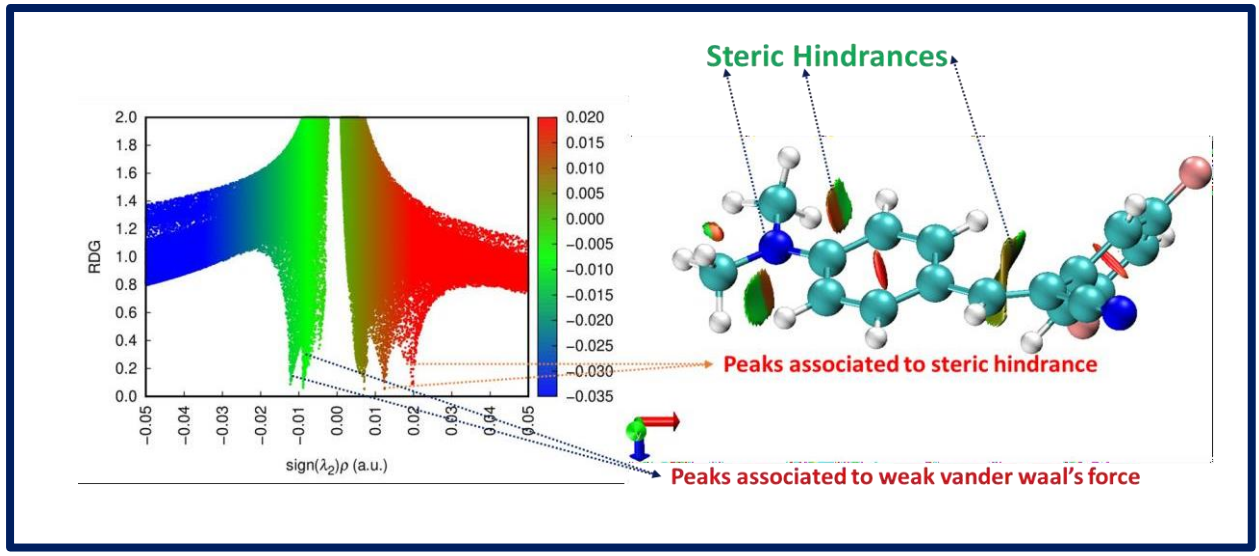

Figure 23. NCI Plots and structure demonstrating the number of steric clashes present in ***Z*-NMe_2CNF_2 .**

From this point of view, it can be put forward that divergent behavior can be observed upon ortho substituting the above mentioned two regioisomers. The single-crystal X-ray structure was collected for both the regioisomers. Photoconversion of the *E*-isomer to the *Z*- one was carried out irradiating the *E*-regioisomer with ambient light for straight 70 hours in solution state. The photoconversion was responsible to 405 nm light irradiation as well. Crystallization of the photoconverted solution led us to the synthesis of the z-isomer i.e. ***Z*- NMe_2CNF_2**. This photo conversion from *E*- to *Z*- stereoisomer is highly reliant on the packing form of the crystal lattice structure. From the single crystal data (Figure 11, 13), it can be surmised that the C5-C6 bond has been buckled out of planarity in comparison to the planes of phenyl rings in case of Z-isomer on the other hand those maintaining the planarity in case of the Trans Regio isomer (C6 & C7).

4.6 Conclusion

In conclusion, we have developed two geometric isomers (*E*- and *Z*-) of a cyanovinyl based molecule (**NMe_2CNF_2**) that displays very distinct photo-responsive behaviour in 405 nm visible light. The synthesis and purification was simple and straightforward. The ***E*-NMe_2CNF_2** crystals display fascinating photo-mechanical actuating behaviour & optical wave guiding property when illuminated with 405 nm light. The other crystal ***Z*-NMe_2CNF_2** responds to 405 nm light by optical wave guiding property only. ***E*-NMe_2CNF_2** molecular crystal undergoes chopping & bending in presence of light stimuli. ***E*-NMe_2CNF_2** molecular crystal undergoes very differently under light illumination exhibiting photo-chopping, bending, twisting behaviour because of the stress generation inside the crystal interior due to photo induced [2+2] cycloaddition & *E* to *Z* geometrical isomerization reaction. Both ***E*-NMe_2CNF_2 & *Z*-NMe_2CNF_2** crystals are showing optical wave guiding behaviour which is under investigation. Our strategy of manipulating photo-reactivity by geometric isomerism could be extended further for various types of molecules to explore diverse mechanical properties and suitably be integrated for machinery tools, robotics, optical fibre etc.

References:

[1]. T. Kim, L. Zhu, R. O. Al-Kaysi and C. J. Bardeen, *ChemPhysChem*, 2014, **15**, 400-414.

[2]. J. M. Abendroth, O. S. Bushuyev, P. S. Weiss and C. J. Barrett, *ACS Nano*, 2015, **9**, 7746-7768.

[3]. T. J. White, ed., *Photomechanical Materials, Composites, and Systems*, 1 edn., Wiley, Hoboken, New Jersey, 2017.

[4]. T. Ikeda, J. Mamiya and Y. Yu, *Angew. Chem. Int. Ed.*, 2007, **46**, 506-528.

[5]. T. J. White, N. V. Tabiryan, S. V. Serak, U. A. Hrozhyk, V. P. Tondiglia, H. Koerner, R. A. Vaia and T. J. Bunning, *Soft Matter*, 2008, **4**, 1796-1798.

[6]. L. Liu, M.-H. Liu, L.-L. Deng, B.-P. Lin and H. Yang, *J. Am. Chem. Soc.*, 2017, **139**, 11333−11336.

[7]. R. O. Al-Kaysi and C. J. Bardeen, *Adv. Mater.*, 2007, **19**, 1276-1280.

[8]. L. Zhu, R. O. Al-Kaysi and C. J. Bardeen, *J. Am. Chem. Soc.*, 2011, **133**, 12569-12575.

[9]. L. Zhu, R. O. Al-Kaysi and C. J. Bardeen, *Angew. Chem. Int.Ed.*, 2016, **55**, 7073-7076.

[10]. S. Kobatake, S. Takami, H. Muto, T. Ishikawa and M. Irie, *Nature*, 2007, **446**, 778-781.

[11]. M. Morimoto and M. Irie, *J. Am. Chem. Soc.*, 2010, **132**, 14172-14178.

[12]. D. Kitagawa, H. Nishi and S. Kobatake, *Angew. Chem. Int. Ed.*, 2013, **52**, 9320-9322.

[13]. D. Kitagawa, R. Tanaka and S. Kobatake, *Phys. Chem. Chem. Phys.*, 2015, **17**, 27300--27305.

[14]. H. Koshima, N. Ojima and H. Uchimoto, *J. Am. Chem. Soc.*, 2009, **131**, 6890-6891.

[15]. H. Koshima, K. Takechi, H. Uchimoto, M. Shiro and D. Hashizume, *Chem. Commun.*, 2011, **47**, 11423-11425.

[16]. P. Naumov, J. Kowalik, K. M. Solntsev, A. Baldridge, J.-S. Moon, C. Kranz and L. M. Tolbert, *J. Am. Chem. Soc.*, 2010, **132**, 5845-5857.

[17]. N. K. Nath, L. Pejov, S. M. Nichols, C. Hu, N. Saleh, B. Kahr and P. Naumov, *J. Am. Chem. Soc.*, 2014, **136**, 2757-2766.

[18]. O. S. Bushuyev, A. Tomberg, T. Friscic and C. J. Barrett, *J. Am. Chem. Soc.*, 2013, **135**, 12556-12559.

[19]. H. Wang, P. Chen, Z. Wu, J. Zhao, J. Sun and R. Lu, *Angew. Chem. Int. Ed.*, 2017, **56**, 9463 –9467.

[20]. R. O. Al-Kaysi, A. M. Muller and C. J. Bardeen, *J. Am. Chem. Soc.*, 2006, **128**, 15938-15939.

[21]. D. K. Bucar and L. R. MacGillivray, *J. Am. Chem. Soc.*, 2007, **129**, 32-33.

[22]. A. E. Keating and M. A. Garcia-Garibay, in *Organic and Inorganic Photochemistry*, eds. V. Ramamurthy and K. S. Schanze, Dekker, New York, 1 edn., 1998, vol. 2, pp. 195-248.

[23]. R. Medishetty, A. Husain, Z. Bai, T. Runčevski, R. E. Dinnebier, P. Naumov and J. J. Vittal, *Angew. Chem. Int. Ed.*, 2014, **126**, 6017-6021.

[24]. R. Medishetty, S. C. Sahoo, C. E. Mulijanto, P. e. Naumov and J. J. Vittal, *Chem. Mater.*, 2015, **27**, 1821-1829.

[25]. E. Hatano, M. Morimoto, T. Imai, K. Hyodo, A. Fujimoto, R. Nishimura, A. Sekine, N. Yasuda, S. Yokojima and S. Nakamura, *Angew. Chem. Int. Ed.*, 2017, **56**, 12576-12580.

[26]. T. Kim, M. K. Al-Muhanna, S. D. Al-Suwaidan, R. O. Al- Kaysi and C. J. Bardeen, *Angew. Chem. Int. Ed.*, 2013, **52**, 6889- 6893.

[27]. C. T. Sun and Z. H. Jin, *Fracture Mechanics*, Academic Press, Waltham, MA, 2012.

[28]. S. Saha, M. K. Mishra, C. M. Reddy and G. R. Desiraju, *Acc. Chem. Res.*, 2018, **51**, 2957-2967.

[29]. E. Ahmed, D. P. Karothu and P. Naumov, *Angew. Chem. Int. Ed.*, 2018, **57**, 837–8846.

[30]. H. Fu, D. Xiao, J. Yao and G. Yang, *Angew. Chem. Int. Ed.*, 2003, **42**, 2883-2886.

[31]. Y. Lei, Q. Liao, H. Fu and J. Yao, *J. Phys. Chem. C*, 2009, **113**, 10038-10043.

[32]. X. Zhang, X. Zhang, W. Shi, X. Meng, C. Lee and S. Lee, *J. Phys. Chem. B*, 2005, **109**, 18777-18780.

[33]. X. Zhang, C. Dong, J. A. Zapien, S. Ismathullakhan, Z. Kang, J. Jie, X. Zhang, J. C. Chang, C. S. Lee and S. T. Lee, *Angew. Chem. Int. Ed.*, 2009, **48**, 9121-9123.

[34]. Z.-Q. Lin, P.-J. Sun, Y.-Y. Tay, J. Liang, Y. Liu, N.-E. Shi, L.- H. Xie, M.-D. Yi, Y. Qian, Q.-L. Fan, H. Zhang, H. H. Hng, J. Ma, Q. Zhang and W. Huang, *ACS Nano*, 2012, **6**, 5309–5319.

[35]. S.-H. Yang, Z.-Q. Lin, N.-E. Shi, L.-Z. Jin, M.-N. Yu, L.-H. Xie, M.-D. Yia and W. Huang, *CrystEngComm*, 2015, **17**, 1448– 1452.

[36]. L. Peng, Y.-N. Chen, Y. Q. Dong, C. He and H. Wang, *J. Mater. Chem. C*, 2017, **5**, 557-565.

[37]. R. O. Al-Kaysi, F. Tong, M. Al-Haidar, L. Zhu and C. J. Bardeen, *Chem. Commun.*, 2017, **53**, 2622-2625

[38]. F. Tong, W. Xu, M. Al-Haidar, D. Kitagawa, R. O. Al-Kaysi and C. J. Bardeen, *Angewandte Chemie*, 2018, **130**, 7198-7202.

[39]. M. B. Epstein and J. Ross, *J. Phys. Chem.*, 1957, **61**, 1578- 1578.

[40]. M. S. Bakshi, *Cryst. Growth & Des.*, 2015, **16**, 1104-1133.

[41]. F. Tong, M. Liu, R. O. Al-Kaysi and C. J. Bardeen, *Langmuir*, 2018, **34**, 1627-1634.

[42]. Peter R. Spackman, Michael J. Turner, Joshua J. McKinnon, Stephen K. Wolff, Daniel J. Grimwood, Dylan Jayatilaka and Mark A. Spackman, *Journal of Applied Crystallography*, 2021, **54(3)**. https://doi.org/10.1107/S1600576721002910